Ultrafast Relaxation Dynamics and Optical Properties of GaAs and GaAs-based Heterostructures

By

Stephanie N. Gilbert Corder

Dissertation

Submitted to the Faculty of the

Graduate School of Vanderbilt University

in partial fulfillment of the requirements

for the degree of

DOCTOR OF PHILOSOPHY

in

Interdisciplinary Materials Science

December, 2014

Nashville, Tennessee

Approved:

Jimmy Davidson, PhD

Richard Haglund, PhD

Timothy Hanusa, PhD

Norman Tolk, PhD

Kalman Varga, PhD

INTERDISCIPLINARY MATERIALS SCIENCE

Ultrafast Relaxation Dynamics and Optical Properties of GaAs and GaAs-based Heterostructures

Stephanie N. Gilbert Corder

Dissertation under the direction of Professor Norman H. Tolk

Three previously unreported photo-carrier relaxation pathways are presented and discussed in GaAs-based systems. In bulk GaAs, a transient bleach of the spin-split exciton transition 1s $\rightarrow 2p_{\pm}$ is reported following photo-excitation at low temperatures and is likely caused by final state blocking of the $2p_{\pm 1}$ exciton level. The bleach of the 1s $\rightarrow 2p_{-1}$ transition is delayed with respect to that of the free carriers and 1s $\rightarrow 2p_{+1}$, suggesting electronic relaxation occurs through two simultaneous mechanisms: elastic scattering between quantized conduction band states and spin-dependent relaxation through the $2p_{\pm 1}$ exciton states. For ErAs:GaAs composites, the response at short time delays is completely dependent on the occupation of the interface trap state between the ErAs nanoparticles and the GaAs matrix. Occupation of the interface state depends on the photo-carrier energy, carrier density, and trap density. Carrier scattering from the interface state plays a large role in the response as it prevents full relaxation of the system on ultrashort timescales. The composite ErAs:GaAs systems also exhibit an oscillatory response highly suggestive of surface plasmon polaritons at the interface between the semi-metallic ErAs and semiconducting GaAs, which couple to the GaAs phonon modes. The oscillation frequencies are observed to follow the same trend with volume fraction as the static absorption resonance peaks, suggesting different nanoparticle size distributions exist with different ErAs incorporation.

To my mom

and grandpa

for their unending support.

ACKNOWLEDGMENTS

I would like to thank several people without whom this project would not have been completed. First and foremost, my advisor Norman Tolk for his vision and support, the Tolk research group members past and present who made this process enjoyable, G. Larry Carr for his mentorship and willingness to work with me, my family and friends for mental support during this process, and finally my husband Chris, whose unceasing questions led me to think deeper about my research than anyone else, even when it was unwillingly so.

I would like to gratefully acknowledge the VINSE core laboratories for access to equipment, the NSF IGERT program, the Department of Energy and Army Research Offices for funding.

TABLE OF CONTENTS

Page

DEDICATION . . . . **ii**

ACKNOWLEDGMENTS . . . . **iii**

LIST OF FIGURES . . . . **ix**

LIST OF TABLES . . . . **x**

Chapter

1. INTRODUCTION. **1**

Interest in Bulk GaAs. 2
Interest in ErAs:GaAs Composite Systems 2
Organization 3

2. OPTICAL PROPERTIES OF GALLIUM ARSENIDE **5**

Introduction to Optics 5
Macroscopic Form of Maxwell's Equations.................................... 5
Properties of the Medium.. 6
Complex Index of Refraction and Dielectric Constants 7
Drude-Lorentz Model of Optical Properties.................................... 12
Band Structure of Solids 14
Metallic vs. Insulating Materials 16
Effective Mass.. 19
Landau Levels 20
Semiconductor Dynamics 22
Optical Excitation of a Crystal Lattice 22
Quasiparticles and Quanta in an Excited Crystal Lattice..................... 23
Carrier Relaxation 28
Measuring Dynamic Properties with Pump and Probe Spectroscopy . . . 30
Summary 31

3. **MAGNETO-SPECTROSCOPY OF GAAS** 32

Introduction 32
Exciton Excitation and Relaxation Dynamics 34
Experimental Setup 38
Static Absorption Spectroscopy of GaAs 39
Photo-Induced Spectroscopy of GaAs 41
Time-Resolved Pump and Probe Spectroscopy 46
Differential Transmission of GaAs 47
Summary 53

4. **RELAXATION PATHWAYS IN ERAS:GAAS SYSTEMS** 54

Introduction 54
State of Research 56
Growth Process 56
The Bulk ErAs:GaAs Interface Structure 57
Electrical Characterization of the Embedded Nanoparticle ErAs:GaAs Interface 59
Previous Optical Studies of Superlattice Structures and Related Systems . 59
Single Layer ErAs:GaAs Dynamics 66
Sample Structure and Growth 66
Experimental Details 67
Results and Discussion 69
Conclusions 78

5. **SURFACE PLASMON POLARITONS IN ERAS:GAAS** 80

Motivation 80
State of Research 81
ErAs Absorption Across a Confinement-Induced Bandgap 81
ErAs Absorption as a Surface Plasmon Resonance 82
Experimental Description 84
Samples Under Investigation 85
Static Infrared Absorption 87
Time-Resolved Optical Measurements 89
Summary 93

6. **CONCLUDING REMARKS** 95

7. **APPENDIX** 98

Excitonic Calculations 98
Carriers per Island Calculation 98

Simulation Code for the ErAs:GaAs Potential Barrier Dynamics 99
Phonon Frequencies 108

BIBLIOGRAPHY 109

LIST OF FIGURES

Figure 2.1 The Electromagnetic Wave 6

Figure 2.2 Reflection and Transmission at an Interface 10

Figure 2.3 Schematic Diagram of the Atomic States of a Covalent Crystal Forming Energy Bands 15

Figure 2.4 Electron Occupancy of States at Room Temperature 17

Figure 2.5 The GaAs Crystal Structure 18

Figure 2.6 The GaAs Band Structure 19

Figure 2.7 Landau Level Structure at the Band Gap 21

Figure 2.8 Direct Band Gap and Exciton Structure. 25

Figure 2.9 Bandfilling Effects 27

Figure 2.10 Basic Recombination Processes in Semiconductors 30

Figure 3.1 Heavy Hole Exciton Absorption Peak in a Quantum Well Structure . . . 35

Figure 3.2 Non-Resonant Exciton Formation 36

Figure 3.3 Theoretical Contributions to Differential Absorption Spectra. 37

Figure 3.4 NSLS Experimental Design 39

Figure 3.5 Temperature Dependence of the Exciton Population. 40

Figure 3.6 Field Dependence of the GaAs Absorption Edge at 20 K. 41

Figure 3.7 Photo-induced Absorption Spectra of GaAs at 50 K as a Function of Field 42

Figure 3.8 Photo-induced Absorption Spectra of GaAs at 5 K as a Function of Field 43

Figure 3.9 Static Absorption Spectra and Model of Transitions 44

Figure 3.10 Photo-induced Spin-dependent Exciton Transitions 45

Figure 3.11 Photo-induced Absorption Spectra of GaAs at 5 T and 5 K as a Function of Excitation Wavelength 47

Figure 3.12 Photo-induced Absorption of GaAs Oscillator Strength and Mode Width at 5 K as a Function of Photo-excitation Energy 48

Figure 3.13 Formation of the Differential Transmission Response at 5 T, 5 K and 795 nm 49

Figure 3.14 Decay of the Differential Transmission Response at 5 T, 5 K and 795 nm 50

Figure 3.15 Effective Mass Comparison for Different Applied Magnetic Fields at 784 nm and 5 K 51

Figure 3.16 Effective Mass Comparison for Different Excitation Wavelengths at 5 K 52

Figure 3.17 Oscillator Transition Strengths at 5 T, 5 K, and 784 nm 53

Figure 4.1 ErAs:GaAs Deposition Dependence and Current Density 57

Figure 4.2 Structural Model of the ErAs:GaAs (001) Interface 58

Figure 4.3 High-angle Annular Dark-field Images TEM of the ErAs/GaAs Interfaces 60

Figure 4.4 Average Differential Conductance for ErAs Nanoparticles and GaAs Matrix. 61

Figure 4.5 Optical-pump THz-probe of GaAs Reference 62

Figure 4.6 ErAs:GaAs Superlattice Optical Pump-THz Probe Response. 62

Figure 4.7 ErAs:GaAs Superlattice Transient Decay as a Function of Superlattice Period L 63

Figure 4.8 ErSb:GaSb Superlattice Transient Decay as a Function of Superlattice Growth Parameters. 65

Figure 4.9 ErSb:GaSb Superlattice Growth Parameters 66

Figure 4.10 Absorption and Sample Structure of the $ErAs_x$:$GaAs_{1-x}$ Composite System.. 68

Figure 4.11 Spectral Response of $ErAs_x$:$GaAs_{1-x}$ at 1.38 eV. 71

Figure 4.12 Spectral Response of $ErAs_x$:$GaAs_{1-x}$ at 1.46 eV. 73

Figure 4.13 Spectral Response of $ErAs_x$:$GaAs_{1-x}$ at 1.55 eV. 76

Figure 5.1 Absorption Spectra for 0.5-4.5% ErAs 82

Figure 5.2 Transmission and Absorption for ErAs/GaAs Superlattices 83

Figure 5.3 Normalized Transmission for Three ErAs:GaAs Samples at Room Temperature 84

Figure 5.4 $ErAs_x$:$GaAs_{1-x}$ Composite Absorption Data 86

Figure 5.5 $ErAs_x$:$GaAs_{1-x}$ Composite Absorption Change 87

Figure 5.6 $ErAs_x$:$GaAs_{1-x}$ Composite Absorption in the Mid-Infrared 88

Figure 5.7 Oscillatory Response of $ErAs_x$:$GaAs_{1-x}$ Composites at 1.55 eV 89

Figure 5.8 Oscillation Frequencies of $ErAs_x$:$GaAs_{1-x}$ Composites at 1.55 eV 90

Figure 5.9 Oscillatory Response of 10% $ErAs_x$:$GaAs_{1-x}$ at 1.38 eV 92

Figure 5.10 Frequency of 10% $ErAs_x$:$GaAs_{1-x}$ at 1.38 eV 93

Figure 5.11 Polarization Dependence of the Oscillatory Response Below the Bandgap 94

Figure 7.1 GaAs Characteristic Timescales for Excitation at 1.46 and 1.55 eV 107

LIST OF TABLES

Table 2.1 Quanta of Crystal Lattice Excitations 23

Table 2.2 Photo-excited Semiconductor Relaxation Regimes 29

Table 3.1 Energy in Different Units for Comparison. 39

Table 5.1 Average Observed Oscillation Frequencies Compared to Phonon Frequency at 1.55 eV 91

Table 7.1 Experimental Values of the Index of Refraction and Expected Phonon Frequencies at 1.55 eV 108

CHAPTER 1

INTRODUCTION

There are two possible outcomes:
if the result confirms the hypothesis, then you've made a measurement.
If the result is contrary to the hypothesis, then you've made a discovery.
Enrico Fermi

Photo-excitation in condensed matter systems results in the creation of complex many-body states arising from the interaction of quasiparticles and quanta of the excited system. The evolution of these many-body states is of fundamental interest as knowledge of such behaviors could motivate the creation of devices. The work presented in this dissertation is based on understanding the relaxation dynamics of gallium arsenide (GaAs), the archetypal III-V compound semiconductor, following photo-excitation. Gallium arsenide has long been a material of great interest in semiconductor research as a result of its direct band gap and optical accessibility with femtosecond (fs) Ti:Sapphire laser systems. Due to its relative popularity, many have assumed there is no work remaining in the study of GaAs and have moved on to less familiar semiconductors and composite systems. As will be seen in the subsequent chapters, many questions remain about the general GaAs relaxation process and its time-evolution.

The techniques used in this work are static and time-resolved optical spectroscopy. These optical methods provide fundamental information about nonlinear properties, non-equilibrium dynamics, many-body effects, state occupation and transport properties of semiconductors.

Photo-excitation generates carrier populations with non-equilibrium temperature distributions, and optical spectroscopy provides the best means of characterizing population distributions as well as determining their relaxation dynamics [1].

Relaxation dynamics in semiconductors occur in different temporal regimes. As a result, different optical techniques are required to characterize the full relaxation process. For GaAs optically excited at 300 K, carriers undergo rapid energy and momentum redistribution within the first few picoseconds (ps). The system thermalizes in nanoseconds (ns), with full equilibrium occurring in tens of ns. These time scales are significantly slower when the system is held at cryogenic temperatures.

Interest in Bulk GaAs

The characterization of the relaxation dynamics of intrinsic GaAs provides a way to investigate many-body effects in a compound semiconductor. Effects such as band-gap renormalization, carrier interactions, alteration of exciton binding energies, energy level broadening, bleaching, phase space filling, alteration of matrix elements, and non-equilibrium occupation of states all depend on the photo-excited carrier density and the system being investigated.

Interest in ErAs:GaAs Composite Systems

Manipulation of the GaAs relaxation process can be achieved through the incorporation of nanoparticulates co-deposited with GaAs during the molecular beam expitaxy (MBE) growth process. Metal-semiconductor composites have hybrid electronic, dielectric and optical properties that may be controlled by manipulating the amount of metal in the semiconductor [2], enabling the engineering of materials for specific uses. The incorporation of erbium (Er) in the GaAs growth process yields composite ErAs:GaAs systems. These

composite systems offer improved detection efficiency and performance as compared to other common detection materials like low temperature (LT) grown GaAs [3] while nearly doubling the efficiency of GaAs-based multi-junction solar cells [4]. The system is also a major contender for the development of compact terahertz (THz) generators and detectors capable of being excited with commercially available lasers at 800 nm [5]. Composites of ErAs:GaAs may be grown at temperatures above 450° C, resulting in higher crystal quality and improved transport characteristics like carrier mobility in comparison to LT GaAs which is grown around 250° C [6, 7]. The ErAs nanoparticles have intrinsic carrier trapping times below 190 fs which can be tuned over two orders of magnitude by changing the growth parameters [8].

In addition to the trapping behavior, the inclusion of metallic particles in semiconductors results in infrared resonances [2]. The incident light field displaces the metallic electrons in the nanoparticles, causing accumulation or depletion of charge at the edges and resulting in a net restoring force on the electrons. The electron oscillations can have large amplitudes under resonant excitation, resulting in localized surface plasmons [9].

Organization

The subsequent chapters are organized as follows: Chapter 2 contains an overview of the physical concepts used in this work, including a general description of GaAs optical and structural properties. Relevant semiconductor concepts relating to the absorption of photons by a direct bandgap semiconductor and relaxation pathways are introduced. The behavior of an optically excited semiconductor in an applied magnetic field and excitation quanta in a condensed matter system will also be discussed.

Chapter 3 details the characterization of the static and transient absorption of GaAs subjected to low temperatures and high magnetic fields in the far-infrared (FIR) spectral region.

The data provide evidence for a previously unreported relaxation pathway in GaAs through Auger-like scattering of Landau-quantized electrons into exciton states.

Chapters 4 and 5 will detail studies of ErAs:GaAs composite systems. The composites are characterized using static and time-resolved optical techniques in the near infrared (NIR). Chapter 4 shows the interface between the embedded semi-metallic ErAs and the GaAs host behaves as a Schottky barrier. Carrier trapping and scattering are observed to depend highly on the occupation of the interface states. Chapter 5 explores the response of the ErAs:GaAs system at longer time delays following photo-excitation. The results suggest surface plasmon polaritons generated when the ErAs nanoparticles are photo-excited couple strongly to GaAs lattice excitations, creating a long-lived oscillating response and enhancing absorption below the GaAs conduction band edge.

Chapter 6 summarizes the results of this work, including detailing the three previously unreported dynamic pathways observed in GaAs-based systems and their potential impact on device engineering.

The appendix contains example calculations referenced in the text, as well as the simulation code used in Chapter 4 to show the composite ErAs:GaAs system dynamics can be represented by a simple 3 level system.

CHAPTER 2

OPTICAL PROPERTIES OF GALLIUM ARSENIDE

Never memorize something that you can look up.

Albert Einstein

Properties of material systems must be understood in order for technical applications to be realized. The optical response of solid materials can provide valuable information about the nature of the system, like the electronic structure, transport properties, bond strength, defect structure, many-body effects, and relaxation dynamics all. The following introduces the interaction light with semiconductors, with a specific focus on GaAs.

Introduction to Optics

The interaction of light and matter can be described at the most fundamental level using Maxwell's equations. Optical wavelengths are thousands of times larger than the size of an atom. Therefore, within a unit wavelength the atoms present in a solid can be treated as continuous when averaged over the microscopic spatial fluctuations [11, 12]. As a result, the semi-classical macroscopic form of Maxwell's equations can be used to determine the response of a condensed matter system to an optical field.

Macroscopic Form of Maxwell's Equations

Maxwell's equations relate the most basic quantities to uniquely determine the field vectors from a distribution of currents and charges. The electric field vector **E**, magnetic induction

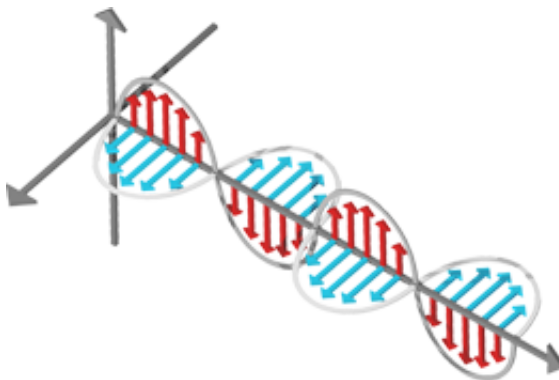

Figure 2.1 An electromagnetic wave propagating in the z direction where the electric field is represented in blue and the magnetic field in red, from [10].

B, magnetic field vector **H**, electric displacement **D**, and electric current density **J** may be written in macroscopic form as:

$$\nabla \cdot \mathbf{D} = \mathbf{4}\pi\rho \tag{2.1}$$

$$\nabla \times \mathbf{E} = -\frac{\mathbf{1}}{\mathbf{c}}\frac{\partial \mathbf{B}}{\partial \mathbf{t}} \tag{2.2}$$

$$\nabla \cdot \mathbf{B} = \mathbf{0} \tag{2.3}$$

$$\nabla \times \mathbf{H} = \frac{\mathbf{1}}{\mathbf{c}}\frac{\partial \mathbf{D}}{\partial \mathbf{t}} + \frac{\mathbf{4}\pi}{\mathbf{c}}\mathbf{J} \tag{2.4}$$

where c is the speed of light in a vacuum and ρ is the electric charge density.

Properties of the Medium

Maxwell's relations are supplemented by materials equations which describe the response of a system to the electromagnetic field. For a harmonic electromagnetic field and a material system at rest, the linear materials equations are

$$\mathbf{j} = \sigma\mathbf{E} \tag{2.5}$$

$$\mathbf{D} = \varepsilon \mathbf{E} = \varepsilon_\mathbf{0} \mathbf{E} + \mathbf{P} \tag{2.6}$$

$$\mathbf{B} = \mu \mathbf{H} = \mu_\mathbf{0} \mathbf{H} + \mathbf{M} \tag{2.7}$$

where σ is the specific conductivity, ε is the dielectric constant, **P** is the polarization, μ is the magnetic permeability, and **M** is the magnetization of the medium [13].

The polarization of the medium **P** induced by the electromagnetic field can be expressed in terms of the electric field components as a tensor relation

$$\mathbf{P} = \varepsilon_\mathbf{0} \chi_\mathbf{E} \mathbf{E} \tag{2.8}$$

where χ_E is the electric susceptibility tensor. Likewise, the magnetic susceptibly tensor χ_M may be described by

$$\mathbf{M} = \mu_\mathbf{0} \chi_\mathbf{M} \mathbf{H} \tag{2.9}$$

Conductors are materials in which σ is non-zero. Insulators or dielectrics have negligibly small σ values, and their electric and magnetic properties may be completely determined by ε_r and μ_r. For nonmagnetic materials (μ_r=1), the dielectric function connects the displacement field of the medium with the electric field of the light and is the basis for characterizing the optical response of semiconductors.

Complex Index of Refraction and Dielectric Constants

The most general phenomena describing the interaction of solid materials with light can be classified into three groups: transmission, reflection, and propagation. During propagation, the light may be refracted (waves travel slower than in free space, bending the light rays as described by Snell's law), absorbed (the beam is attenuated), and scattered (light interacts with the medium, causing it to change direction and possibly frequency, also attenuating the beam) [14].

Dynamic properties may be investigated using the reflection and refraction of light at a planar interface between dielectrics through changes in intensity, phase, and polarization of the electromagnetic radiation [12]. Reflection at the surface of the material is determined by the coefficient of reflectivity, R, and is defined as the ratio of the reflected power to the power incident on the surface. Similarly, the transmission is determined by the coefficient of transmissivity, T, which is the ratio of the transmitted power to the incident power. In the absence of scattering,

$$R + T + A = 1 \tag{2.10}$$

where the absorption, A, will be defined below.

The absorption coefficient α is used to quantify the absorption of light in a medium by defining the fraction of power absorbed per unit length of the material according to Beer's Law:

$$I(z) = I_0 e^{-\alpha z} \tag{2.11}$$

where I_0 is the optical intensity at $z = 0$ for a beam propagating in the z direction.

In a transparent medium, the propagation of an incident beam is described by the refractive index n, where n is defined as the ratio of the velocity of light in free space, c, to the velocity of light in the medium v:

$$n = \frac{1}{\sqrt{\mu\varepsilon}} = \frac{c}{v} \tag{2.12}$$

where n is dependent on the frequency of the incident light beam, producing an effect called dispersion.

The absorption and refractive index are incorporated into a quantity called the complex

index of refraction given by

$$\tilde{n} = n + i\kappa \tag{2.13}$$

where κ is the imaginary term called the extinction coefficient and is related to the absorption by

$$\alpha = \frac{4\pi\kappa}{\lambda} \tag{2.14}$$

where λ is the wavelength of light in free space.

The relative dielectric function ε_r (or relative permittivity) is related to the vacuum dielectric constant through

$$\varepsilon_r(\omega) = \frac{\varepsilon(\omega)}{\varepsilon_0} = \varepsilon_1 + i\varepsilon_2 \tag{2.15}$$

where $\varepsilon(\omega)$ is the frequency dependent absolute dielectric function of the material.

ε_r is related to the complex index of refraction $\tilde{n}$ and the two quantities are commonly used to describe optical properties of dielectric materials. For nonmagnetic matter, the two quantities are related to one another by the following equations [14]

$$\varepsilon_1 = n^2 - \kappa^2 \tag{2.16}$$

$$\varepsilon_2 = 2n\kappa \tag{2.17}$$

$$n = \sqrt{\frac{\sqrt{\varepsilon_1^2 + \varepsilon_2^2} + \varepsilon_1}{2}} \tag{2.18}$$

$$\kappa = \sqrt{\frac{\sqrt{\varepsilon_1^2 + \varepsilon_2^2} - \varepsilon_1}{2}} \tag{2.19}$$

Both sets of optical constants are equally valid but have different utility in understanding matter: n and κ are related to the phase velocity and attenuation of plane waves in materials

while ε_1 and ε_2 are useful when considering sub-wavelength optical effects.

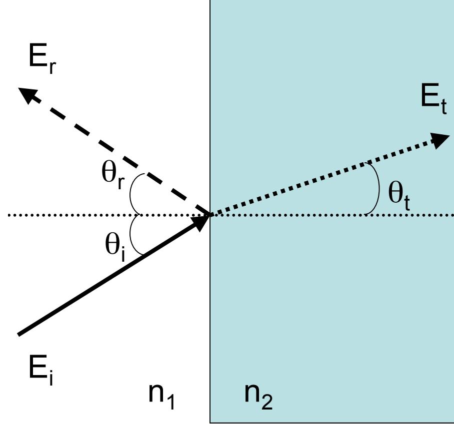

Figure 2.2 Reflection and transmission at an interface.

The reflectivity of a dielectric depends on the complex index of refraction. Reflection and transmission of light at an interface are a function of the angle of the light incident on the material surface and also the light polarization [15]. The incident and reflected angles $\theta_{i,r}$ are defined relative to the material surface normal. The reflection and transmission can be resolved into perpendicular components: $R = r_p^2 + r_s^2$ and $T = t_p^2 + t_s^2$. For polarization in the plane of incidence (p polarization), the reflection at an interface is given by

$$r_p = \frac{E_r}{E_i} = \frac{n_2^2 cos\theta_i - n_1\sqrt{n_2^2 - n_1^2 sin^2\theta_i}}{n_2^2 cos\theta_i + n_1\sqrt{n_2^2 - n_1^2 sin^2\theta_i}} \tag{2.20}$$

where E_r (E_i) is the reflected (incident) electric field and θ_r has been eliminated using Snell's law. n_1 is the index of refraction of the medium in which the light is propagating (usually air or vacuum) while n_2 is the index of refraction of the material under investigation (see Figure 2.2).

The transmission is given by

$$t_p = \frac{E_t}{E_i} = \frac{2n_1 n_2 cos\theta_i}{n_2^2 cos\theta_i + n_1\sqrt{n_2^2 - n_1^2 sin^2\theta_i}} \tag{2.21}$$

where E_t is the transmitted electric field.

For polarization perpendicular to the plane of incidence (s polarization), the reflection and transmission are, respectively;

$$r_s = \frac{E_r}{E_i} = \frac{n_1 cos\theta_i - \sqrt{n_2^2 - n_1^2 sin^2\theta_i}}{n_1 cos\theta_i + \sqrt{n_2^2 - n_1^2 sin^2\theta_i}} \tag{2.22}$$

$$t_s = \frac{E_t}{E_i} = \frac{2n_1 cos\theta_i}{n_1 cos\theta_i + \sqrt{n_2^2 - n_1^2 sin^2\theta_i}} \tag{2.23}$$

For normal incidence, (θ_i=0), the reflection and transmission of both polarizations reduce to

$$r_{p,s} = \frac{E_r}{E_i} = \frac{n_2 - n_1}{n_2 + n_1} \tag{2.24}$$

$$t_{p,s} = \frac{E_t}{E_i} = \frac{2n_1}{n_1 + n_2} \tag{2.25}$$

The $r_{p,s}$ and $t_{p,s}$ constitute the Fresnel coefficients of reflection and transmission where in the absence of absorption $r_p + t_p = 1$ and $r_s + t_s = 1$. It can clearly be seen that the observed reflection or transmission from a surface is highly dependent on the incident angle and polarization of the light, as well as the material properties described by the index of refraction. To further investigate the response of a system to an applied electromagnetic field, the material response will be modeled as a microscopic harmonic oscillator.

Drude-Lorentz Model of Optical Properties

The classical Lorentz theory of optical properties makes the assumption that electrons and ions in a material can be modeled as simple harmonic oscillators subjected to a driving force by means of an applied electromagnetic field. The equation of motion for an electric charge -e of mass m is given by

$$m[\ddot{\mathbf{x}} + \gamma\dot{\mathbf{x}} + \omega_0^2\mathbf{x}] = -e\mathbf{E}(\mathbf{x},t) \quad (2.26)$$

where γ is the damping coefficient and ω_0 is the resonance frequency [12]. For a field varying harmonically ($e^{-i\omega t}$) in time with frequency ω, the dipole moment p of one electron is

$$\mathbf{p} = -e\mathbf{x} = \frac{e^2}{m}\frac{\mathbf{E}}{(\omega_0^2 - \omega^2 - i\omega\gamma)} \quad (2.27)$$

The material response is the sum of individual dipoles, so for N molecules per unit volume with f_j electrons per molecule, binding frequencies ω_j, and damping constants γ_j;

$$\sum_j \mathbf{p}_j = -Ne\mathbf{x} = \frac{Ne^2\mathbf{E}}{m}\sum_j \frac{f_j}{(\omega_j^2 - \omega^2 - i\omega\gamma_j)} \quad (2.28)$$

Given equation 2.27 and the dielectric function $\varepsilon_r(\omega)$= 1+χ, equation 2.28 can be written as

$$\varepsilon_r(\omega) = 1 + \frac{Ne^2}{\varepsilon_0 m}\sum_j \frac{f_j}{(\omega_j^2 - \omega^2 - i\omega\gamma_j)} \quad (2.29)$$

where the f_j are referred to as oscillator strengths [12].

Low Frequency Response of the Dielectric Function: Optical Conductivity

If some fraction of the electrons per molecule are unbound ($\omega_0 = 0$), as ω approaches zero the dielectric function can be written

$$\varepsilon(\omega) = \varepsilon_{bg}(\omega) + i\frac{Ne^2 f_0}{m\omega(\gamma_0 - i\omega)} \tag{2.30}$$

where ε_{bg} is the background dipole contribution from the free electrons [12]. The conductivity σ may be written as

$$\sigma = \frac{f_0 Ne^2}{m(\gamma_0 - i\omega)} \tag{2.31}$$

when the properties of the medium arise from only the dielectric function [12]. Equation 2.31 is the Drude conductivity for the medium if the number free electrons per unit volume in the medium is $f_0 N$.

High Frequency Response of the Dielectric Function: Plasma Frequency

For high frequencies where $\omega \gg \gamma_0$, the dielectric function in equation 2.30 can be approximated as

$$\varepsilon(\omega) = \varepsilon_{bg}(\omega) - \varepsilon_0 \frac{\omega_p^2}{\omega^2} \tag{2.32}$$

where ω_p is defined as the the plasma frequency of the conduction electrons $\omega_p^2 = Ne^2/m^*\varepsilon_0$ and includes binding effects through the effective mass term m^* (see below) [12].

In small metal nanoparticles, the optical properties are dominated by surface plasmon resonance effects [16]. The polarizability of a sphere is given by

$$P = \frac{\chi_e \varepsilon_0 E}{1 + \chi_e/3} \tag{2.33}$$

Assuming the carriers in the nanoparticle behave as a free electron gas, the susceptibility

may be written as:

$$\chi_e(\omega) = -\frac{Ne^2}{m^* \varepsilon_0 \omega^2}. \tag{2.34}$$

Combining the previous two equations, one sees

$$P(\omega) = \frac{\varepsilon_0 E}{1 - Ne^2/3m^* \varepsilon_0 \omega^2} = \frac{\varepsilon_0 E}{1 - \omega_p^2/3\omega^2} \tag{2.35}$$

where ω_p is the plasma frequency of the bulk metal. The polarization equation diverges for frequency values of $\omega_{sp} = \omega_p/\sqrt{3}$ where ω_{sp} is the surface plasmon frequency of the metal sphere [16].

Band Structure of Solids

The close proximity of atoms in a solid results in the interatomic separation distance being approximately the same size as the atom, producing overlap of the orbitals and strong inter-atomic interactions. This creates a broadening of the discrete atomic levels into bands which form a continuum of states [14].

Electrons in a crystal are arranged in energy bands separated by forbidden regions, or band gaps, in which no electron orbitals exist. The bands form as a result of the interaction between the lattice ions and electron wavefunctions [16]. Bragg reflection of electron waves in the crystal give rise to energy gaps, as traveling wave solutions to the Schrödinger equation do not exist at points satisfying the Bragg condition [16].

Band theory arises from the single electron approximation, wherein an electron is assumed to be subject to the effective (average) potential field of fixed lattice ions, inner shell electrons, and other valence electrons [11, 17]. For perfect crystals, the potential energy of the crystal $V(\mathbf{r})$ has the periodicity of the lattice. Solutions of the Schrödinger equation

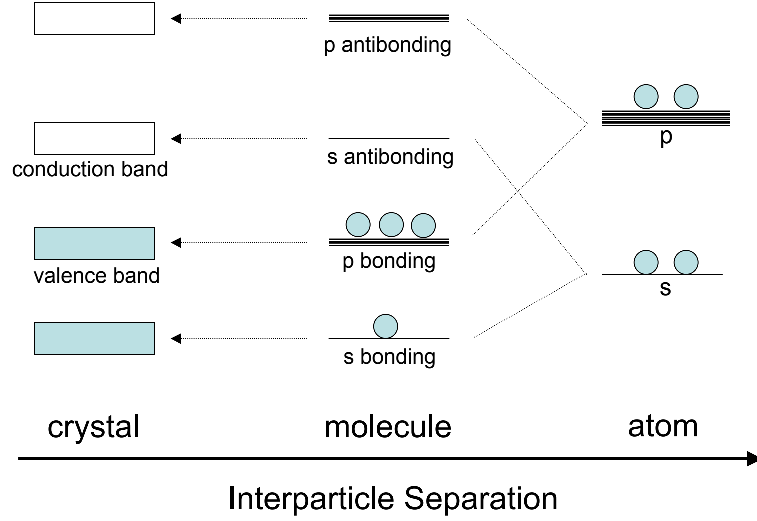

Figure 2.3 Schematic diagram of the atomic states of GaAs. As the interparticle separation decreases, the *s* and *p* states of the atoms hybridize, forming occupied bonding and unoccupied antibonding molecular states. The bonding and antibonding states evolve into the valence and conduction bands as the interparticle spacing decreases further.

$$\frac{\hbar^2}{2m}\nabla^2\psi + [E - V(\mathbf{r})]\psi = \mathbf{0} \tag{2.36}$$

are Bloch functions of the form

$$\psi(\mathbf{k},\mathbf{r}) = \mathbf{u_k}(\mathbf{r})\exp(\mathbf{ik}\cdot\mathbf{r}) \tag{2.37}$$

where $u_k(\mathbf{r})$ has the periodicity of the lattice, $\mathbf{k}$ is the crystal momentum, and $\mathbf{r}$ is the radial direction [11]. This indicates there are eigen-energies E where $\mathbf{k}$ is real and electron wave functions exist; conversely, there are energy ranges where $\mathbf{k}$ is imaginary and no energy states exist [17]. The eigenstates where $\mathbf{k}$ is real are referred to as the energy bands of the solid and the imaginary states are the forbidden states or energy gaps. In this way, the band structure of the solid is a direct result of the periodicity of the lattice.

For free electrons, eigen-energies can be written as

$$E = \frac{p^2}{2m} = \frac{\hbar^2 \mathbf{k^2}}{2m} \tag{2.38}$$

and the energy bands of a material are then plotted in terms of energy vs. **k**-space direction. For real crystals, spin-orbit coupling, crystal field lattice splitting, and other effects lift the degeneracies of some points in the **k**-space plot.

Taking into account the two spin orientations of electrons, there are *2N* independent orbitals in each energy band, where N is the number of atoms in the primitive cell. Materials with fully occupied bands are insulators provided the filled bands are separated by an energy gap from the next higher band as in Figure 2.4. For crystals with even numbers of valence electrons per primitive cell, but with no energy gap between levels, two partially filled bands may exist and therefore the crystal is a metal.

Metallic vs. Insulating Materials

As previously stated, the occupancy of the highest band containing electrons determines whether a material is metallic or insulating. If the band is partially full, electrons may take part in conduction. For metals, the structure and number of valence electrons per atom produces occupied and unoccupied bands with no energy gap between them [15]. If the highest occupied band is completely full, no electrons are available for conduction and the material is an insulator. The band gap is the energy difference between the lowest point of the conduction band (conduction band edge) and the highest point of the valence band (valence band edge).

The highest occupied energy level is called the Fermi level and is defined in metals such that all the states below are occupied and states above are unoccupied. The dielectric response of a metal is due to intraband transitions: where an electron is excited from an occupied

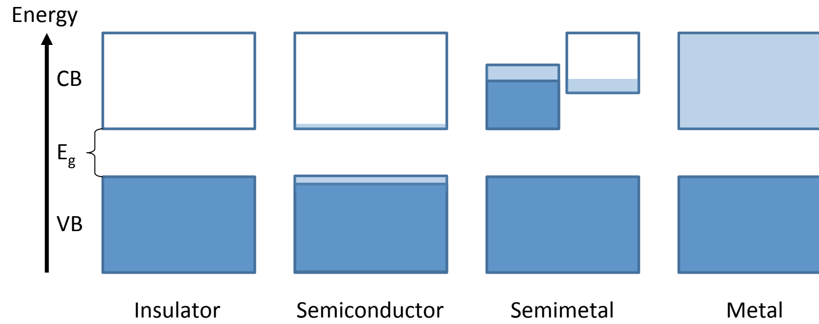

Figure 2.4 Electron occupancy of states at room temperature. Dark blue shading represents fully occupied bands and light blue shading indicates partially filled bands. The conduction band (CB) is separated in energy from the valence band (VB) by the energy gap (E_g). The availability of states and electron number determine whether a material is insulating, semiconducting, semimetallic or metallic.

to unoccupied state within the same band, changing crystal momentum **k** and requiring a quantized lattice vibration or impurity to conserve momentum [15].

An intrinsic (undoped) semiconductor is characterized by a bandgap separating an occupied valence band and empty conduction band at low temperatures [1]. The conductivity of intrinsic semiconductors increases with temperature: an electron in the highest occupied (valence) band is thermally excited to the lowest empty (conduction) band [17]. The energy difference required to excite the electron from the valence to conduction band is called the intrinsic band gap. The vacancy left in the valence band by the excited electron is called a hole, and behaves like a positively charged electron. As the temperature of the intrinsic semiconductor increases, the energy gap between the highest occupied valence band and lowest unoccupied conduction band decreases.

If no momentum change ($\Delta\mathbf{k} = 0$) is required to photo-excite a carrier from the valence band maximum to the conduction band minimum, the semiconductor has a direct band gap. If a momentum change is required, photo-excitation must involve quantized lattice

vibrations or impurity states. In this case, the material has an indirect band gap.

Band Structure of GaAs

The GaAs lattice consists of two interpenetrating face-centered cubic lattices as can be seen in Figure 2.5. The Zinc Sulfide structure consists of four valence electrons per atom and eight atoms per unit cell [15]. Each electron can be in either a bonding or antibonding state, resulting in 16 states per value of **k** space, or eight bands. In the ground state, GaAs has four completely full valence or bonding bands and the top four conduction/antibonding states are empty. The gap between the bonding and antibonding states makes GaAs a semiconductor [15].

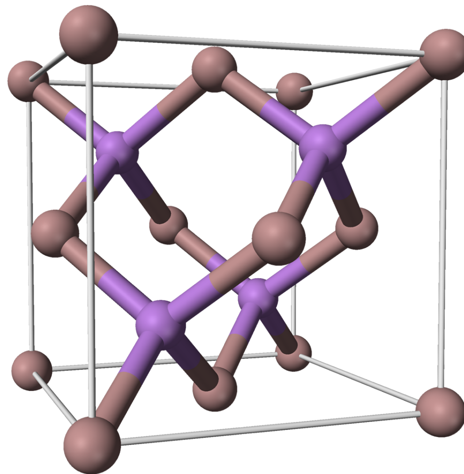

Figure 2.5 Crystal Structure of GaAs: Zinc Blende or two interpenetrating FCC sublattices. The Ga ions are indicated by red balls while the As ions are represented as purple balls. The tetrahedral bonding structure is evident. From [18].

Bulk GaAs has cubic symmetry; therefore, the conduction band at the zone center has s orbital character with two-fold spin degeneracy. The valence band has p orbital character and

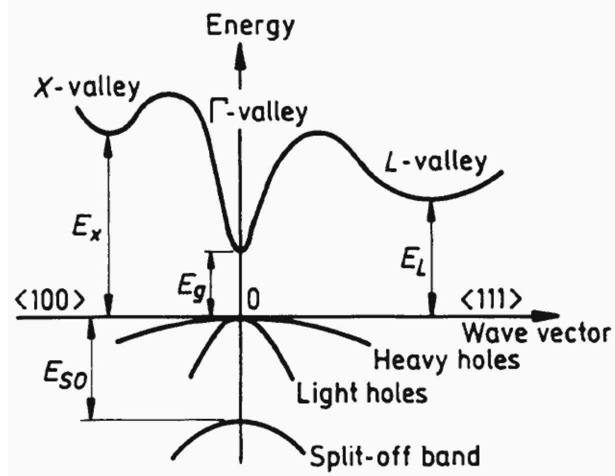

Figure 2.6 The GaAs band structure at 300K. The direct bandgap E_g is at 1.42 eV. The E_L transition is at 1.71 eV and the E_X is at 1.90 eV. The split off hole band E_{SO} is 0.34 eV below the top of the valence band. Adapted from [19].

the top of the valence band is four fold degenerate $J = 3/2$ due to the spin-orbit interaction. This results in heavy hole (HH) and light hole (LH) bands, each two-fold degenerate due to uniaxial stress [1]. The room temperature band structure of GaAs can be seen in Figure 2.6.

Motion of the electrons and holes within an energy band is determined by the energy-momentum dispersion in the material. In a crystal, the electrons are not really free, and equation 2.38 is modified by the lattice ion potential [14].

Effective Mass

The energy bands in a semiconductor or insulator are parabolic for small values of **k** and have dispersions given by

$$E^c = E_g + \frac{\hbar^2 k^2}{2m_e^*} \tag{2.39}$$

$$E^v = -\frac{\hbar^2 k^2}{2m_h^*} \tag{2.40}$$

where $E^{c,v}$ is the energy of the conduction or valence band, and $m^*_{e,h}$ is the electron or hole effective mass, respectively. The effective mass m^* defines the band curvature

$$\frac{1}{m^*} = \frac{1}{\hbar^2}\frac{\partial^2 E}{\partial k^2} \tag{2.41}$$

The effective mass is thus a measure of the curvature of the energy band in **k**-space. m^* will be close to m_0 near the bottom of the parabolic conduction band. If the energy band has little **k** dependence, m^* is very large [16].

Landau Levels

When a strong magnetic field is applied to a semiconductor, it causes the conduction electrons to move in circular orbits around the field at a frequency $\omega_c = \frac{e\mathbf{B}}{m_0}$ known as the cyclotron frequency. The energy and radius of the electron orbits have discrete values. The quantized energies, known as Landau levels, follow $E_n = (n+1)\hbar\omega_c$ where $n = 0, 1, 2, ...$ [14]. Electrons in a magnetic field move in **k**-space on a surface of constant energy, normal to **B** [16].

For a direct gap semiconductor with the magnetic field **B** applied in the $\hat{z}$ direction and the sample plane in $\hat{x}$-$\hat{y}$, the motion of the electrons in the conduction band will be quantized in the $\hat{x}$-$\hat{y}$ plane with free motion in the $\hat{z}$. For this reason, it can be considered a two-dimensional system. Carriers within the Landau levels have energies given by

$$E^n(k_z) = (n+\frac{1}{2})\frac{e\hbar\mathbf{B}}{m^*} + \frac{\hbar^2 k_z^2}{2m^*} \tag{2.42}$$

where m^* is the effective mass of the appropriate carrier and n is the index of the Landau level as can be seen in Figure 2.7. The first term describes the quantized motion in the $\hat{x}$-$\hat{y}$ plane while the second is the motion in the $\hat{z}$ direction.

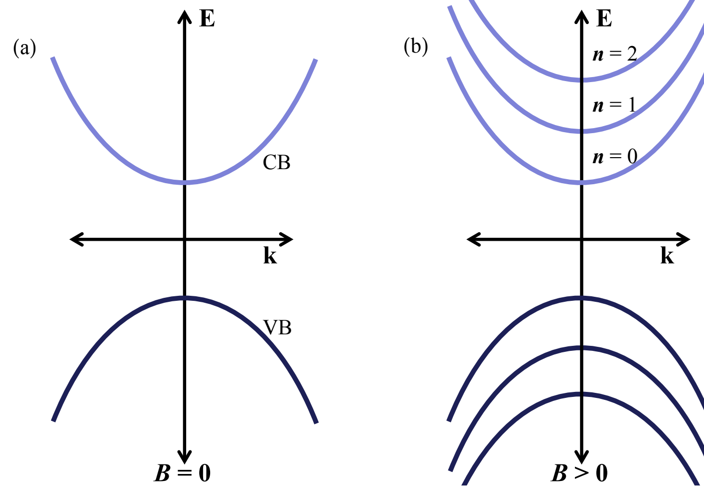

Figure 2.7 Effect of applied magnetic field on the band structure. a) Band structure in the absence of an applied magnetic field where CB indicates the conduction band and VB the valence band. b) Landau level structure at the bandgap in the presence of an applied magnetic field showing quantized levels in both the conduction and valence bands.

To determine the transition energy between different Landau levels, it is useful to redefine the position of zero energy, where $E = 0$ is defined as the top of the valence band. Interband transitions require both an electron in the initial state and an available state (hole) in the final state. Equation 2.42 can therefore be separated into the electron and hole components:

$$E_e^n(k_z) = E_g + (n + \frac{1}{2})\frac{e\hbar\mathbf{B}}{m_e^*} + \frac{\hbar^2 k_z^2}{2m_e^*} \tag{2.43}$$

$$E_h^n(k_z) = -(n + \frac{1}{2})\frac{e\hbar\mathbf{B}}{m_h^*} + \frac{\hbar^2 k_z^2}{2m_h^*} \tag{2.44}$$

The selection rule for interband transitions between Landau levels is $\Delta n = 0$. Therefore, the interband transition energy is given by

$$\hbar\omega = E_e^n(k_z) - E_h^n(k_z) = E_g + (n + \frac{1}{2})\frac{e\hbar\mathbf{B}}{\mu} + \frac{\hbar^2 k_z^2}{2\mu} \tag{2.45}$$

where $\frac{1}{\mu} = \frac{1}{m_e^*} + \frac{1}{m_h^*}$ is the reduced mass of the electron-hole pair [14]. The selection rules

indicate the electron and hole have the same n value, as well as $k_z \approx 0$ due to the negligible momentum of the photon. This results in equally spaced absorption spectra peaks with energies given by

$$E_L^n = E_g + (n + \frac{1}{2})\frac{e\hbar\mathbf{B}}{\mu} \tag{2.46}$$

for positive integer values of n. The absorption edge shifts to higher energy in a magnetic field according to $\frac{e\hbar\mathbf{B}}{2\mu}$. The electron effective mass can be determined from the transmission response and the width of the Landau levels is caused by carrier scattering [14].

Semiconductor Dynamics

Optical excitation is the main method used in this work to perturb a material system from its steady state configuration. Optical excitation results in the absorption of a photon by a crystal lattice. Different methods of absorption exist, depending on the photon energy and available states.

Optical Excitation of a Crystal Lattice

When light of sufficient energy is incident on a material, it causes transitions of electrons from states below the Fermi level to states above [11]. Light incident on metallic systems produces intraband absorption, in which a carrier is excited to a higher energy within the same band. For intrinsic semiconductors and insulators, the band gap of the material determines the minimum energy at which photons are absorbed. This is called the fundamental absorption edge and carriers in the valence band are excited into the conduction band in a process termed interband absorption. Interband absorption results in the creation of an electron-hole pair, with the electron excited to the conduction band and the hole in the valence band [14].

Quasiparticles and Quanta in an Excited Crystal Lattice

Given the right conditions, excitation of a crystal may result in quantized energy states. A few examples relevant to this work are presented below and in Table 3.1; including quantized electron-hole pairs, lattice vibrations and oscillating electrons.

Name	Field	Characteristic Properties	Characteristic Modes
Phonons	Elastic Wave	Lattice Vibrations	Optic and Acoustic
Plasmons	Electron Wave	Free Electrons and Photons	Geometric
Excitons	Polarization Wave	Electron-Hole Pairs	Discrete Orbitals
Polaron	Electron-Elastic Wave	Electrons and Phonons	Dispersive

Table 2.1 Quanta of Crystal Lattice Excitations.

Excitons

The mutual Coulomb attraction of a photo-excited electron and hole can lead to the formation of a bound pair, known as an exciton. Excitons form a hydrogenic system of bound states converging with the conduction band and give rise to an increase in absorption near the band edge [1]. In general, there are two types of excitons: free excitons (Wannier-Mott) and tightly bound (Frenkel) excitons [14]. This work will focus on free excitons, which have a large binding radius and tend to be delocalized states able to move through the crystal. Excitons are stable only if the binding energy is sufficiently large to prevent disruption from thermal effects, such as lattice vibrations. The room temperature thermal energy is $k_B T \approx$25 meV and the binding energy of excitons are on the order of a few meV; therefore, excitons are generally observed at cryogenic temperatures [14].

The binding energy of an exciton E_X can be determined using the Bohr model with a relative dielectric constant and the reduced mass of the electron-hole pair. The energy of the nth

(for n=1,2,...) level relative to ionization limit is given by

$$E_X(n) = -\frac{\mu R_H}{m_0 \varepsilon_r^2 n^2} = -\frac{R_X}{n^2} \tag{2.47}$$

where R_H is the Rydberg constant 13.6 eV of the hydrogen atom and R_X is the Rydberg constant of the exciton. The radius of the exciton is

$$r_{Xn} = \frac{m \varepsilon_r n^2 a_H}{\mu} = n^2 a_X \tag{2.48}$$

where a_H is the Bohr radius of the hydrogen atom 5.29×10^{-11} m and a_X is the exciton radius. From the previous equations, it can be seen that the exciton ground state with $n = 1$ has the largest binding energy and smallest radius. Typical values for GaAs give $R_X = 4.2$ meV and $a_X = 13$ nm, where the electron effective mass is $0.067 m_0$ and $\varepsilon_r = 12.8$ (static dielectric constant values are used since the binding energies are in the far-infrared spectral region) [14].

Exciton energy from a direct transition ($\mathbf{k} = 0$) is the energy required to produce a free electron hole pair E_g minus the Coulomb binding energy:

$$E_{Xn} = E_g - \frac{R_X}{n^2} \tag{2.49}$$

implying the formation of exciton states is energetically favorable compared to free electron hole pairs as the total energy is lower (see Figure 2.8). Excitons are observed in the spectra of very pure samples as impurities produce free carriers which screen the Coulomb interaction and reduce the binding energy, as well as generating local electric fields which ionize the excitons.

In addition to thermal instabilities, if the density of excitons is increased sufficiently or

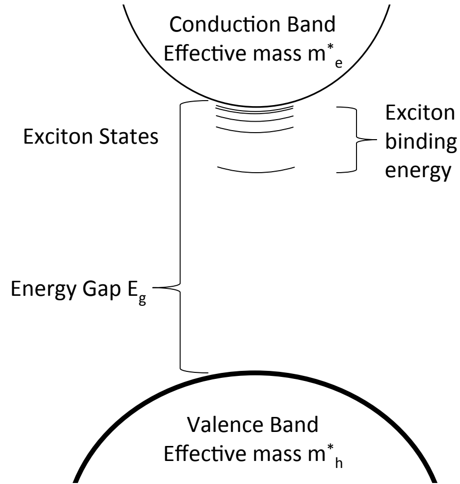

Figure 2.8 Direct band gap and exciton structure, where the lowest exciton level is the ground state and the energy difference between the exciton ground state and the conduction band edge is the exciton binding energy.

free carriers are injected, the Coulomb attraction binding the exciton is screened. In such a situation, the $\mathbf{k} \approx 0$ electron and hole states are filled, causing a decrease in the observed absorption (bleaching) with increasing laser intensity [14, 20]. The bound states becomes unstable and break up into free electron-hole pairs [20].

Excitons are perturbed by the application of electric and magnetic fields. The strength of the perturbation from magnetic fields is proportional to the exciton cyclotron resonance energy $\hbar\omega_c$

$$\hbar\omega_c = \hbar\frac{e\mathbf{B}}{\mu} \tag{2.50}$$

similar to free electrons except for the reduced electron-hole effective mass μ [14].

Phonons

The periodicity of the crystalline lattice in GaAs allows the formation of phonons, or quantized vibrations of lattice ions, with resonant frequencies in the infrared [14, 16]. Both acoustic and optical modes are possible as GaAs has eight atoms per unit cell [1]. The

electric field of the incident light can drive resonant oscillations of charged lattice ions to produce transverse optic phonons (TO). Longitudinal optic (LO) modes displace ions perpendicular to the applied field and thus do not interact with incident light [14].

Acoustic phonon modes require a non-zero wave vector to be created and thus are not directly generated from the incident light. Instead, optical phonons decay into acoustic phonons which are capable of traveling and scattering within the crystal. Acoustic modes are classified as longitudinal or transverse with different characteristic velocities [1]. Phonons play a large role in the relaxation of semiconductors as they act as an energy and momentum exchange mechanism between excited carriers and the crystal lattice.

Polarons

A polaron is the coupling of an electron and phonon; a local displacement of the crystal lattice immediately surrounding an electron. The distortion of the lattice follows the electron as it travels through the crystal. The polaron mass is larger than the unexcited lattice mass because the electron and lattice distortion move together. The deviation in mass can be measured through the cyclotron resonance frequency.

Surface Plasmons

A quantized oscillation of the free electron gas with respect to the positive lattice ions is called a plasmon. The displacement of the oscillations is in the direction of the electric field [14]. Using the Drude model, the relative dielectric function of a metal nanoparticle may be written as

$$\varepsilon_s = \varepsilon_B - \frac{\omega_p^2}{\omega^2 + i\omega\gamma} \tag{2.51}$$

where ε_B is the real background dielectric constant, ω is the optical frequency, ω_p is the plasma frequency, $\gamma = (1/\tau)$ is the carrier scattering frequency and τ is the scattering time.

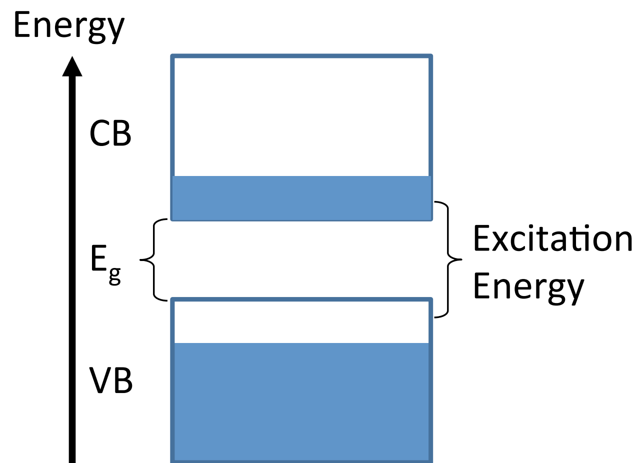

Figure 2.9 Bandfilling effects at room temperature. The conduction band (CB) is separated in energy from the valence band (VB) by the energy gap (E_g). The excitation energy of the light is greater than the bandgap energy, exciting electrons into the conduction band until no more states are available and the exciting light is transmitted.

Resonant Absorption Non-linearities

When large numbers of electrons are photo-excited in a semiconductor with an energy greater than the bandgap, electrons fill the states at the bottom of the conduction band and holes fill the top of the valence band as can be seen in the schematic shown in Figure 2.9. The exclusion principle holds for interband optical transitions, requiring the final state be unoccupied for an electron to absorb a photon. As the excitation source intensity is increased, the absorption gradually saturates as the available bands fill with photo-carriers in an effect called the band-filling nonlinearity [14]. If a carrier of the same type already exists in the final state, the transition is blocked and the effect is referred to as Pauli blocking or phase space filling. For high excitation densities, Pauli blocking prevents electrons from being excited as there are no available final states. This causes a blockage of further absorption of the excitation light in an effect called saturable absorption. An increase in

transmission resulting from the blockage of further absorption is termed bleaching of the absorption resonance.

Carrier Relaxation

The absorption of light in a semiconductor can create an electron hole pair with excess energy above the fundamental bandgap value. The initial step towards thermal equilibrium involves electrons and holes scattering out of the optically coupled valence and conduction band states [20]. Quasi-thermal energy distributions are established by carrier-carrier and carrier-phonon scattering. Recombination of the excited electrons and holes occurs by radiative (photon emission) and non-radiative (trapping and energy transfer/Auger) methods. Carrier relaxation can be classified into four regimes with overlapping timescales: coherent, non-thermal, hot carrier, and isothermal regimes [1].

In the coherent regime, the photo-excited carriers in a semiconductor maintain phase coherence with the exciting laser pulse. The coherent regime is described by quantum mechanics and exist on sub-ps time scales in semiconductors [1]. Coherence is destroyed through scattering processes, leading to a non-thermal regime where the excited carrier distribution function cannot be described by temperature. Carrier-carrier scattering redistributes the energy of the system and produces a thermal distribution generally at a higher temperature than the lattice, called the hot carrier regime. The density of excited carriers has a direct influence on the thermalization time, typically on the order of hundreds of fs to a few ps [1]. The carrier thermalization leads to the creation of large populations of phonons. The hot carrier regime is characterized by the cooling of carriers to the lattice temperature and provides information on carrier and phonon scattering processes. In the isothermal regime, the carriers have reached thermal equilibrium with each other and the lattice, but the system is not yet in full thermodynamic equilibrium as recombination has yet to take place. The recombination may occur through radiative (in which a photon is emitted) or non-radiative

Coherent Regime $\leq$200fs
momentum scattering carrier-carrier scattering intervalley scattering $\mathbf{\Gamma}$ to **L**,**X** hole-optical phonon scattering
Nonthermal Regime $\leq$2ps
electron-hole scattering electron-optical phonon scattering intervalley scattering **L**,**X** to $\mathbf{\Gamma}$ intersubband scattering ΔE$> \hbar\omega_{LO}$
Hot – **Carrier Regime** 1-100ps
hot carrier-phonon interactions decay of optical phonons carrier-acoustic phonon scattering intersubband scattering ΔE$< \hbar\omega_{LO}$
Isothermal Regime $\geq$100ps
carrier recombination

Table 2.2 Photo-excited semiconductor relaxation regimes for excitation at t=0. The regimes overlap in time. Typical semiconductor timescales, scattering and relaxation processes are listed for each regime. After [1].

relaxation processes. See Figure 2.10 for some basic examples.

The timescales for each regime are strongly dependent on the system band structure, excitation energy and temperature, mode of excitation, carrier density, and other parameters. Electron-electron scattering is the most efficient thermalizing process for electrons in the Γ valley and the scattering rates are carrier density dependent [1]. Therefore, the relaxation of non-thermal carrier distributions provides direct information concerning carrier-scattering processes. The carrier cooling dynamics are determined by the slower carrier-phonon interactions.

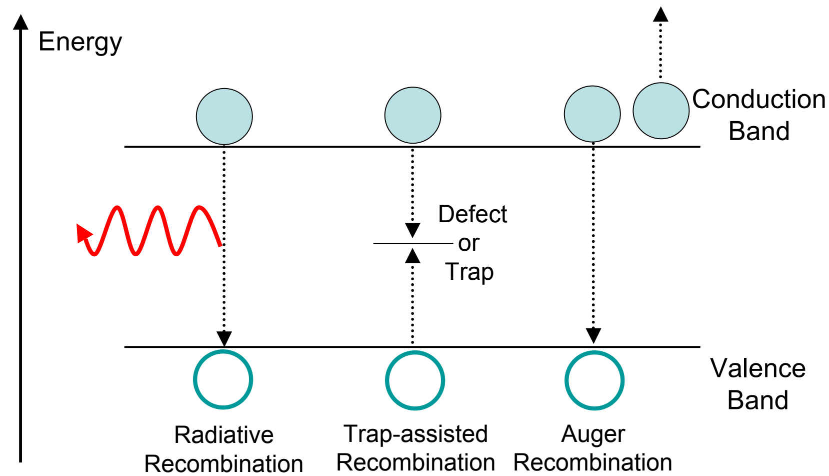

Figure 2.10 Basic relaxation processes in semiconductors. Electrons (blue solid circles) are shown in the conduction band of a semiconductor. They recombine with holes (open blue circles) through a number of processes, the most basic are: radiative recombination in which a photon is emitted as the pair recombine, capture by traps or defects in a mid-gap state, and Auger scattering where a pair recombine and their energy is transferred to a third carrier (shown as an electron).

Measuring Dynamic Properties with Pump and Probe Spectroscopy

The structure and optical properties of a material are characterized by observing the changes in optical properties using the pump and probe technique. In this method, a pump laser pulse excites the material while a weaker probe detects pump-induced changes in the response at a variable time delay. The time resolution is limited by the temporal width of the laser pulses. This technique allows the observation of the energy transfer between the light, electrons and lattice. The identifiable carrier excitation and relaxation regimes are: carrier excitation, momentum redistribution, thermalization and cooling by carrier scattering, carrier lattice thermalization, carrier density reduction by recombination and diffusion, and thermal structural effects [15, 21, 22].

Ultrafast pump-probe spectroscopy will be presented in two forms: degenerate and non-degenerate. Degenerate pump-probe spectroscopy involves the excitation of a sample and

measurement of pump-induced changes at the same photon energy. Non-degenerate pump-probe spectroscopy uses two synchronized light sources at different wavelengths to determine changes induced by the pump at energies away from the excitation energy.

Summary

The structure and electronic configuration of a material determine the allowed energy levels and occupation of those levels. The energy eigen-states and their occupation determines the response of the material to applied fields. Measurable optical properties depend on the fundamental material properties of the dielectric function and susceptibility. One can use changes in the optical properties to deduce information about the structure and electronic configuration of a material through Maxwell's equations. [15]

CHAPTER 3

MAGNETO-SPECTROSCOPY OF GALLIUM ARSENIDE

If you want to find the secrets of the universe,
think in terms of energy, frequency, and vibration.
Nikola Tesla

Introduction

Photo-excitation in condensed matter systems results in the creation of complex many-body states arising from the interaction of quasiparticles and quanta of the excited system [23]. One of the most fundamental quasiparticles is the bound electron-hole pair, or exciton. The influence of excitonic and carrier behavior in applied magnetic fields is of fundamental interest as knowledge of such behaviors could motivate the creation of devices. Energy loss through excitonic absorption and subsequent recombination is one of the major drains on the performance of direct-gap semiconducting solar cells. Direct probing of the interactions between excitons and the photo-excited plasma can be difficult as the internal energy transitions for excitonic states is in the far-infrared spectral range.

The exciton system is mathematically similar to the hydrogen atom with the hole playing the role of the proton and a binding energy on the order of a few meV. The reduction in binding energy compared to the Rydberg energy of the hydrogen atom (13.6 eV) is the result of the significantly smaller effective masses of the exciton pair compared to the free electron and hole as well as the influence of the background semiconductor dielectric con-

stant, which screens the Coulomb interaction [24]. The transitions between bound excitonic states can be probed, with the 1s $\rightarrow$ 2p internal resonance transition the most pronounced.

FIR and THz spectroscopy are able to directly probe non-radiative states not observable with other methods, such as time-resolved photo-luminescence, providing information on energy redistribution while carriers relax to the conduction band edge [25]. THz measurements can identify pair populations in all momentum states, however relatively few have been reported as the measurements are technically complicated [24]. Few experimental systems are capable of probing the meV regions directly as it requires a unique combination of a pulsed laser system synchronized with a broadband THz source, cryogenic cooling of the material of interest as well as the ability to apply magnetic fields. The U4IR beamline at the National Synchrotron Light Source is one of only half a dozen such systems existing worldwide.

Previous work indirectly inferred properties of direct gap bulk semiconductor systems or utilized confinement effects in quantum well structures to push bound state energies to room temperature [23, 26, 27]. In contrast, by directly probing the population of carriers in low energy states of bulk GaAs, the dynamic relaxation processes are evident. The application of a static magnetic field creates discrete states in the GaAs conduction band and populations of excited photo-carriers are observed in these states. Within the spectral window available (20-120 cm^{-1}), the electron cyclotron resonance (ECR) frequency is directly observed, as well as the exciton binding frequency. As the applied magnetic field increases, the exciton binding frequency is observed to split into two distinct modes corresponding to the transition energies between the exciton ground state and the first excited state where the spin degeneracy has been lifted for $\Delta l = \pm 1$.

In addition, the occupation of these states is not instantaneous upon photo-excitation. Carri-

ers are observed to be excited into the ECR mode, corresponding to occupation of the Landau levels in the conduction band, and the excitonic 1s $\rightarrow$ $2p_{+1}$ transition. The excitonic transition 1s $\rightarrow$ $2p_{-1}$ is delayed relative to the other transitions, indicating photo-carriers are not directly excited into the $2p_{-1}$ state, but instead pass through the state during the relaxation process. The dynamical studies further show the degree of non-parabolicity of the conduction band.

Exciton excitation and relaxation dynamics

At low excitation densities, intrinsic semiconductor absorption is dominated by optical transitions of correlated electron-hole pairs with clear excitonic resonances at low temperatures [27]. For excitation well above the bandgap, the photo-carriers undergo very rapid Coulomb and optical phonon scattering, leading to a direct population of excitonic states through the optical phonon decay within 0.6-0.9 ns of photo-excitation [24]. As the carrier density increases, the Coulomb interaction is screened while the conduction and valence band states near the band edge become occupied, producing band filling, absorption bleaching, and renormalization of the bandgap energy to lower values [27]. The excitons interact with acoustic phonons and other excitons to form a hot-exciton gas, which thermalizes above the lattice temperature [1]. The hot-exciton gas cools by emission of acoustic phonons in a process similar to photo-excited electron relaxation, and requires surfaces, defects, or phonons to radiatively recombine [1]. Excited exciton states are not believed to play a large role in the absorption or relaxation dynamics as their oscillator strengths are small; instead functioning as intermediate states as excited carriers relax to the zone center Γ [1].

Many studies have characterized the behavior of excitons in GaAs quantum wells as the quantum confinement increases the thermal stability of the excitons to room temperature [23, 26, 27]. The excitonic absorption in a GaAs quantum well is shown in Figure 3.1 for

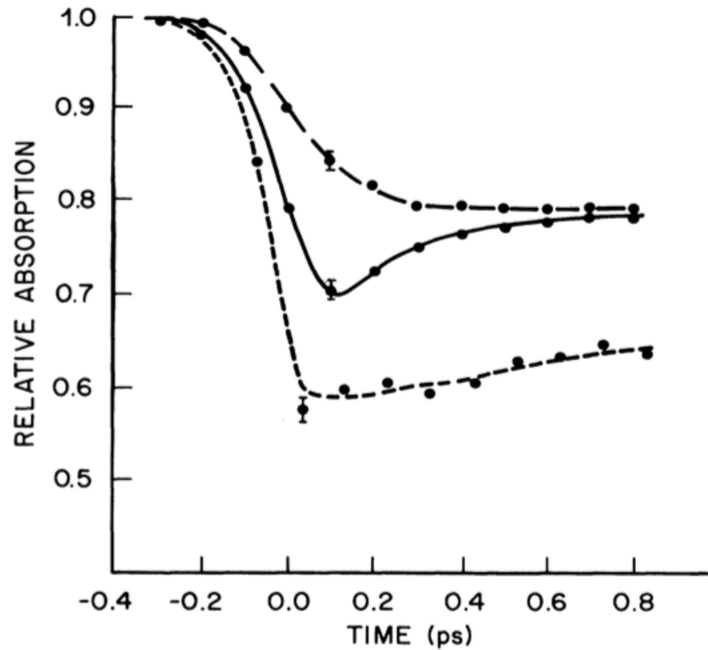

Figure 3.1 Dynamics of the heavy hole exciton peak absorption as a function of time delay for non-resonant 300 K excitation (dashed line); resonant excitation at 300 K (solid line) and resonant 15 K excitation (dot-dashed line) showing the dramatic change in absorption. Reprinted figure with permission from [27]. Copyright 1985 by the American Physical Society.

different excitation conditions: non-resonant excitations induces Coulomb screening, while resonant excitation produces bleaching of the excitonic absorption. The excitonic bleaching recovers to a value determined by Coulomb screening as the excitons are ionized by LO phonons in about 300 fs at 300 K. For 15 K, the LO phonon density is negligible and the resonant pumping produces a similar bleached absorption signature, followed by a recovery time on the order of 10 ps, indicating the fast recovery at room temperature is the result of phonon ionization of the excitons. The bleaching effect is attributed to phase-space filling of the single particle states during resonant excitation. Ionization by LO phonons produces carriers with about 25 meV of excess energy, creating higher temperature distributions and thereby reducing the band filling and screening effects. [27]

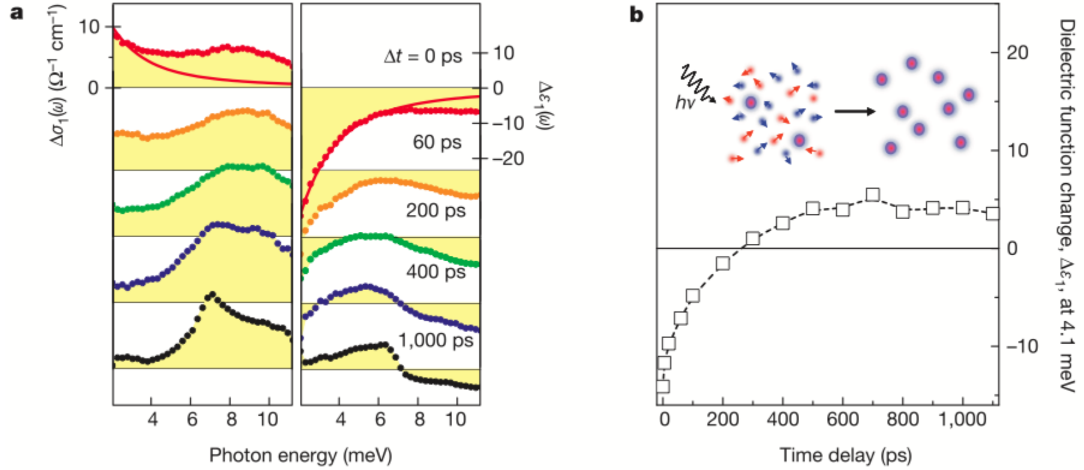

Figure 3.2 Non-resonant exciton formation. a) Exciton formation with 21 meV excess energy at a lattice temperature of 6 K. The change in conductivity is shown in the left panel and change in dielectric function is shown on the right for several time delays. The red lines at t=0 indicate the Drude fit. b) Time evolution of the induced dielectric function response at 4.1 meV showing a decay of conductive properties. Inset: schematic evolution of the electron-hole gas dominated by unbound quasiparticles with excitonic correlations into a population of pure excitons. Reprinted by permission from Macmillan Publishers Ltd: Nature [23], copyright (2003).

The formation, population relaxation and ionization of excitons in GaAs quantum wells have been characterized by optical pump-THz probe for resonant and non-resonant excitation. Resonantly excited exciton populations are observed to decay within several hundred ps of photoexcitation and the exciton peak broadens significantly with temperature, evolving from a Lorentzian oscillator to Drude-like spectrum. However, non-resonantly excited excitons follow a completely different evolution: features build up after excitation over hundreds of ps until a sharp exciton line shape is evident (see Figure 3.2a) at 1,000 ps around 7 meV. Two distinct timescales for exciton formation are discussed: a quasi-instantaneous appearance of excitonic enhancement and a slower full transformation from a photo-excited plasma to a charge-neutral excitonic phase as in Figure 3.2b. The slow increase from negative to positive dielectric values is attributed to a decreasing contribution from the conducting electron-hole gas. The formation of excitons at time delays hundreds

of ps after photo-excitation is characterized by the co-existence of bound and unbound pairs which eventually forms an insulating state. [23]

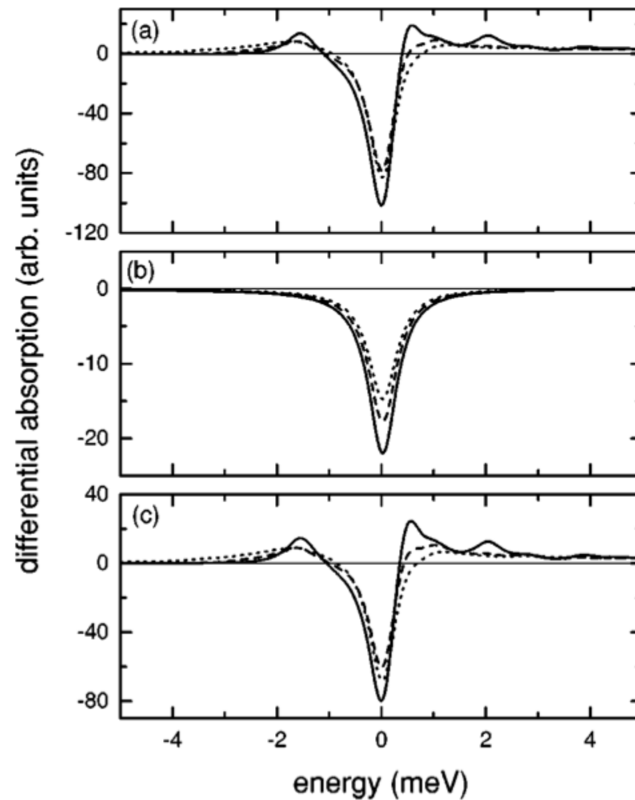

Figure 3.3 Theoretical differential absorption spectra for T=2 K (solid), 25 K (dashed) and 100 K (dotted) induced by thermally occupied excitons. a) Total signal, b) Pauli blocking, and c) Coulomb contributions. Reprinted figure with permission from [28]. Copyright 1999 by the American Physical Society.

Numerical calculations suggest the total differential absorption is similar to the Coulomb interaction-induced response with additional weak bleaching at the exciton peak induced by Pauli blocking. Bleaching of the excitonic state from Pauli blocking decreases with increasing temperature, as can be seen in Figure 3.3a. The Coulomb-induced bleaching decreases from 2 to 25 K and increases from 25 to 75 K, indicating coupling of energetically

higher excitons to the 1s state as seen in Figure 3.3c. The Pauli blocking contribution in Figure 3.3 is small, suggesting the total signal at these temperatures is essentially the result of the Coulomb interaction. Furthermore, the calculations indicate a strong non-linear coupling of low energy free carriers to the 1s exciton state induces the bleaching effects at all temperatures. [28]

The work presented here continues the analysis of exciton formation and relaxation by considering the effects in a bulk system quantized by an applied magnetic filed. The exciton binding energy in bulk GaAs require the sample temperature to stay below 49 K. The normally degenerate exciton spin states are investigated separately through the application of a magnetic field. Bleaching of the transitions between the excitonic 1s ground state and the spin split 2p excited state are observed; however, the dynamics of the bleached transitions and its implications have never been reported.

Experimental Setup

A commercial bulk semi-insulating (100) GaAs wafer 400 μm thick is held at different cryogenic temperatures in a superconducting magnet. Magnetic fields up to 10 T are applied perpendicularly to the sample surface and parallel to the incident beams in the Faraday geometry. A ps NIR pump laser and FIR probe are incident normal to the sample surface. The GaAs is excited at photon energies above the bandgap in the low fluence regime. The probe transmission through the sample is measured using a spectrometer and bolometric detector. The experimental setup has been detailed previously [29, 30, 31]. A schematic of the experimental setup is shown in Figure 3.4.

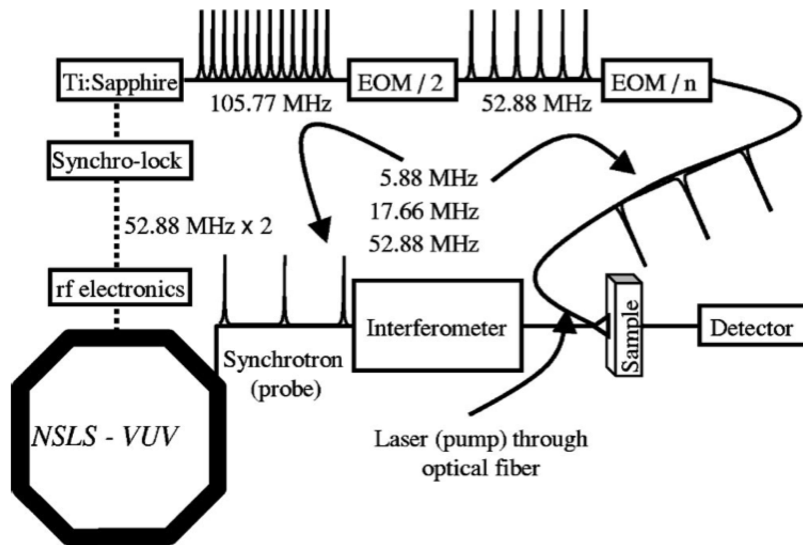

Figure 3.4 Experimental setup at the NSLS for optical pump-THz probe using the synchrotron storage ring as a broadband probe and synchronizing a laser pump. Reprinted with permission from [29]. Copyright 2002, AIP Publishing LLC.

Static absorption spectroscopy of GaAs

Static absorption spectroscopy is performed to determine the transmission of the sample, check for free carrier absorption, determine laser heating of the sample, and characterize the field-dependent variations of the interband transitions. The static transmission (T_0) in the frequency range of 18-110 cm^{-1} is measured to be 51.9%. Table 3.1 provides an energy comparison between common spectroscopic units.

Energy (eV)	Wavelength (nm)	Wavenumber (cm^{-1})	Temperature (K)
1.24	1000	10,000	2,898
0.124	10,000	1,000	290
0.00124	100,000	100	29

Table 3.1 Energy in different units for comparison.

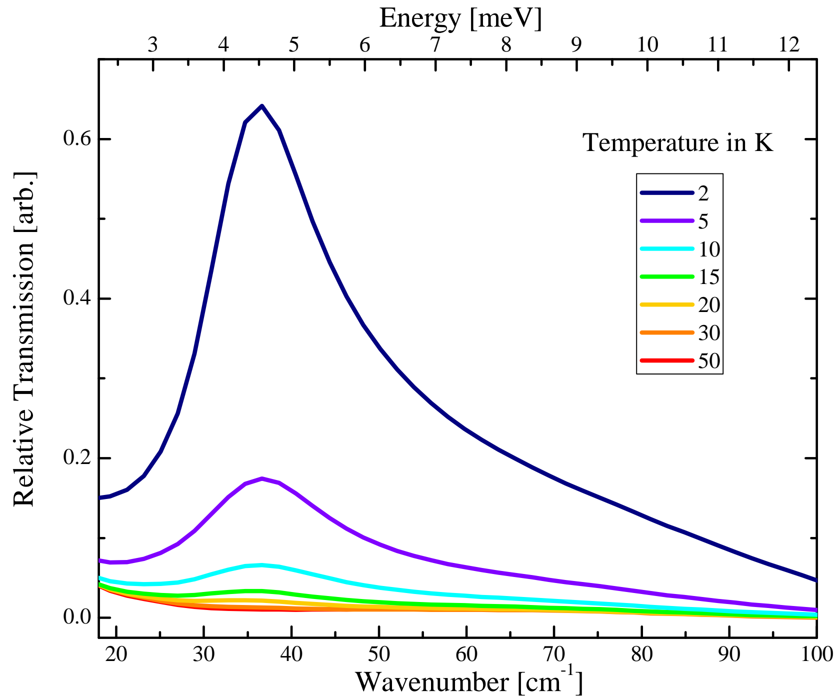

Figure 3.5 Temperature dependence of the background exciton population. The excitons are observed to dissociate around 30 K.

Figure 3.5 shows the temperature dependence of the background exciton population in the absence of an applied magnetic field. The binding energy of the exciton corresponds to a temperature of approximately 49 K. The temperatures listed are those measured in the sample holder and therefore do not take into account laser heating. From the figure, it is clear that sample heating due to the incident laser causes a local temperature rise of about 15-20 K, dissociating the excitons around a sample holder temperature of 30 K.

The application of a static magnetic field to a bulk semiconductor enhances absorption and causes oscillations known as the Franz-Keldysh effect [14, 32]. The band edge shifts to higher energies as the field is increased as can be seen in Figure 3.6 along with oscillations above the band edge. The shift in the absorption band will be evident in the population of

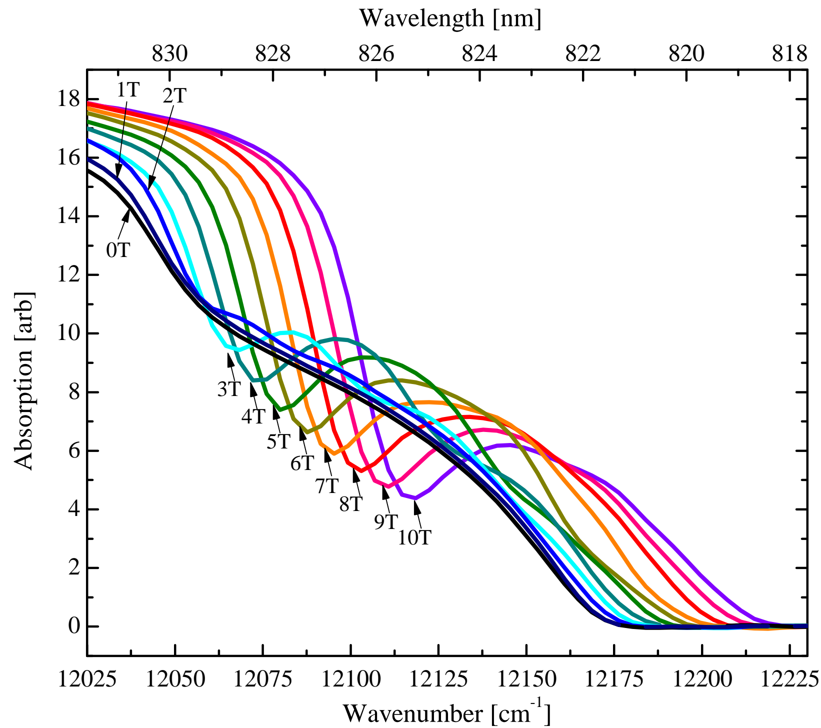

Figure 3.6 Field dependence of the GaAs absorption edge at 20 K showing the shift in absorption with applied magnetic field.

the Landau levels with increasing magnetic field.

Photo-Induced Spectroscopy

The static FIR transmission of the GaAs wafer is measured by comparing populations of photo-induced carriers when the laser is illuminating the sample to the population when the laser is blocked. In this manner, the increased absorption from the photo-excited carriers can be measured. The excitation wavelength of the pump laser is 805 nm. The spectroscopic response as a function of applied magnetic field is shown in Figures 3.7 and 3.8 for sample temperatures of 50 and 5 K, respectively.

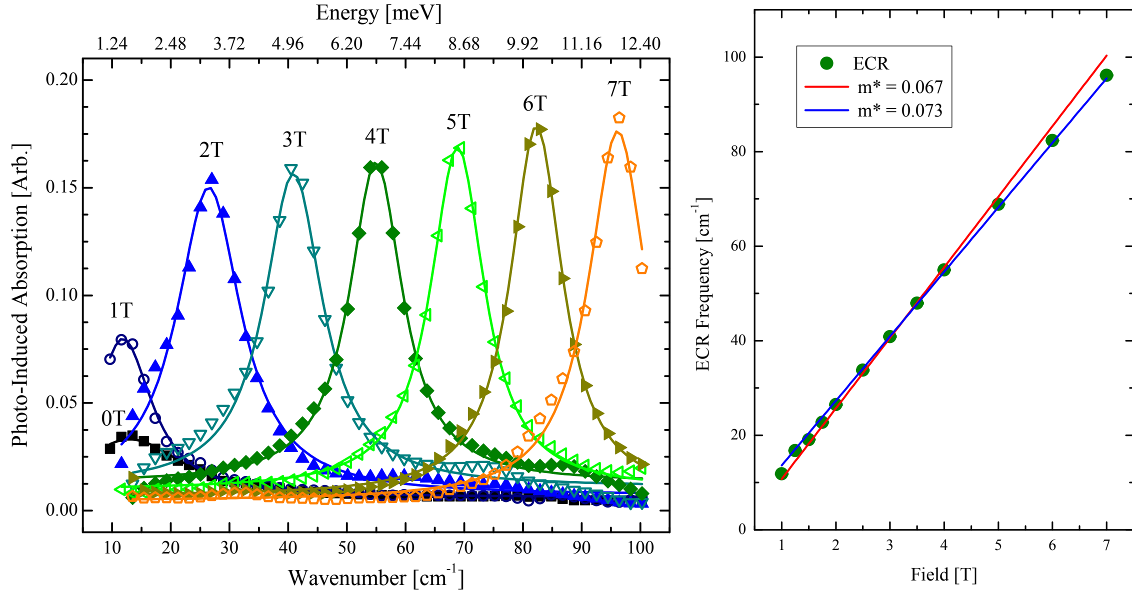

Figure 3.7 Left: Photo-induced Absorption Spectra of GaAs at 50 K as a function of field. At 0 T, the Drude absorption tail can be seen. As the magnetic field increases, the cyclotron resonance peak is observed to form and move to higher frequencies with field. Right: The center frequency of the ECR peaks derived from a Lorentzian fit.

Figure 3.7 shows the static photo-induced spectra as a function of applied magnetic field for a temperature of 50 K. The data (symbols) are fit with single Lorentzian peaks (lines). At 0 T (black squares), the Drude tail of the conductivity can be seen, indicating a population of excited carriers. For non-zero applied fields, the ECR frequency is observed to follow the Landau level field dependence of $\frac{eB}{m^*}$. The center frequency of each peak is shown on the right of Figure 3.7 and the fits shown indicate the observed effective mass m^*=0.073 as well as the accepted static effective mass in GaAs of 0.067. The deviation from the static effective mass is an indication that the excited carriers are not at the zero momentum position of the Landau level and instead are at higher momentum positions in the band.

Figure 3.8 shows the static photo-induced absorption spectra obtained at 5 K for different applied magnetic fields. In contrast to the 50 K data, three peaks are observed for fields greater than 1 T. A single peak exists at 0 T which was not present at 50 K. This peak is the

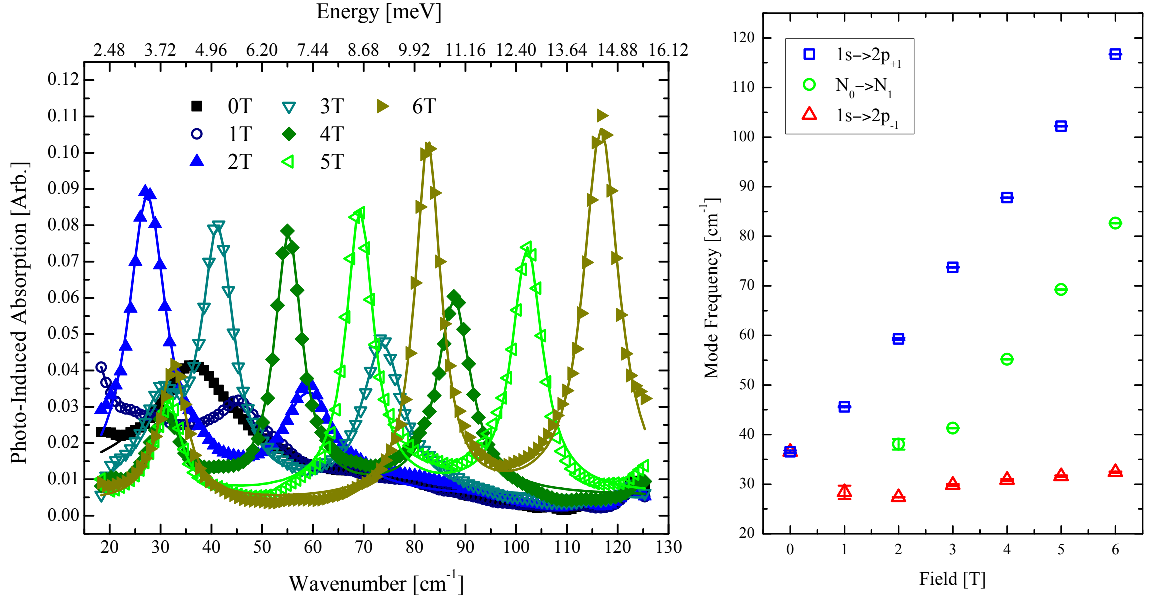

Figure 3.8 Left: Photo-induced Absorption Spectra of GaAs at 5 K. The cyclotron resonance is clearly observed for all non-zero applied magnetic fields, as well as two exciton transition peaks at different frequencies. Right: The center frequencies of the three peaks derived from Lorentzian fits as a function of applied magnetic field.

exciton binding energy observed in Figure 3.5. At 1 T, the ECR peak is evident as well as the exciton peak. By 2 T, the exciton peak has split into two modes, one of which increases in energy with applied field while the other stays approximately constant. A model comparing the mode frequencies with known transitions in the magnetic field-confined bulk GaAs system is presented in Figure 3.9.

At low temperatures, the equilibrium population of excitons resides primarily in the 1s state. The standard dipole selection rule $\Delta l=\pm 1$ makes the 1s$\rightarrow$2p$_{\pm 1}$ transitions the strongest. The same dipole selection rule applies to transitions between the Landau levels which are only confined to motion around the magnetic field lines and experience parabolic dispersion in the $\vec{z}$ direction as a result of the experimental geometry. The three experimentally measured modes correspond well with the theoretical transition frequencies predicted for Landau levels and the 1s$\rightarrow$2p$_{\pm 1}$ transitions [33] as can be seen in Figure 3.9a.

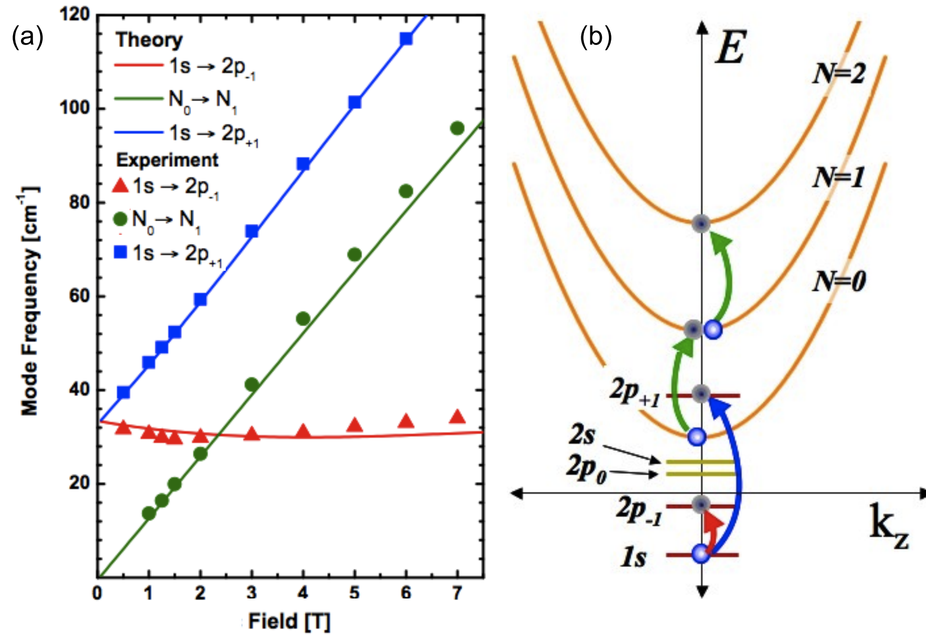

Figure 3.9 Static absorption spectra and transition model at 10 K. a) Mode frequencies as a function of applied field. Symbols: Experimental data. Lines: Theoretical transitions within Landau levels and excited bound states, from [33]. b) Schematic depiction of the energy transition in GaAs in a 5 T applied magnetic field. The applied field quantizes the conduction band into Landau levels and removes the spin degeneracy of the bound exciton levels. The dominant transitions occur between Landau levels (indicated by green symbols and arrows in (a) and (b), respectively), the 1s $\rightarrow$ 2p$_{-1}$ transition (indicated by red symbols and arrows in (a) and (b), respectively) and the 1s $\rightarrow$ 2p$_{+1}$ transition (indicated by blue symbols and arrows in (a) and (b), respectively).

Figure 3.10 compares static photo-induced measurements taken for different probe polarizations after photo-excitation at 795 nm and 5 K in order to verify the transition assignments. Single spectra measured at 5 T are shown on the left and composite spectra for fields 0-10 T are shown on the right. No circular polarizer was used in the measurements in the top panels. The middle panels show the response for left circular polarization of the probe and the bottom panels show the response for right circular polarization of the probe. The absorption feature near 37 cm^{-1} for **B**=0 is assigned to the 1s $\rightarrow$ 2p transition of the

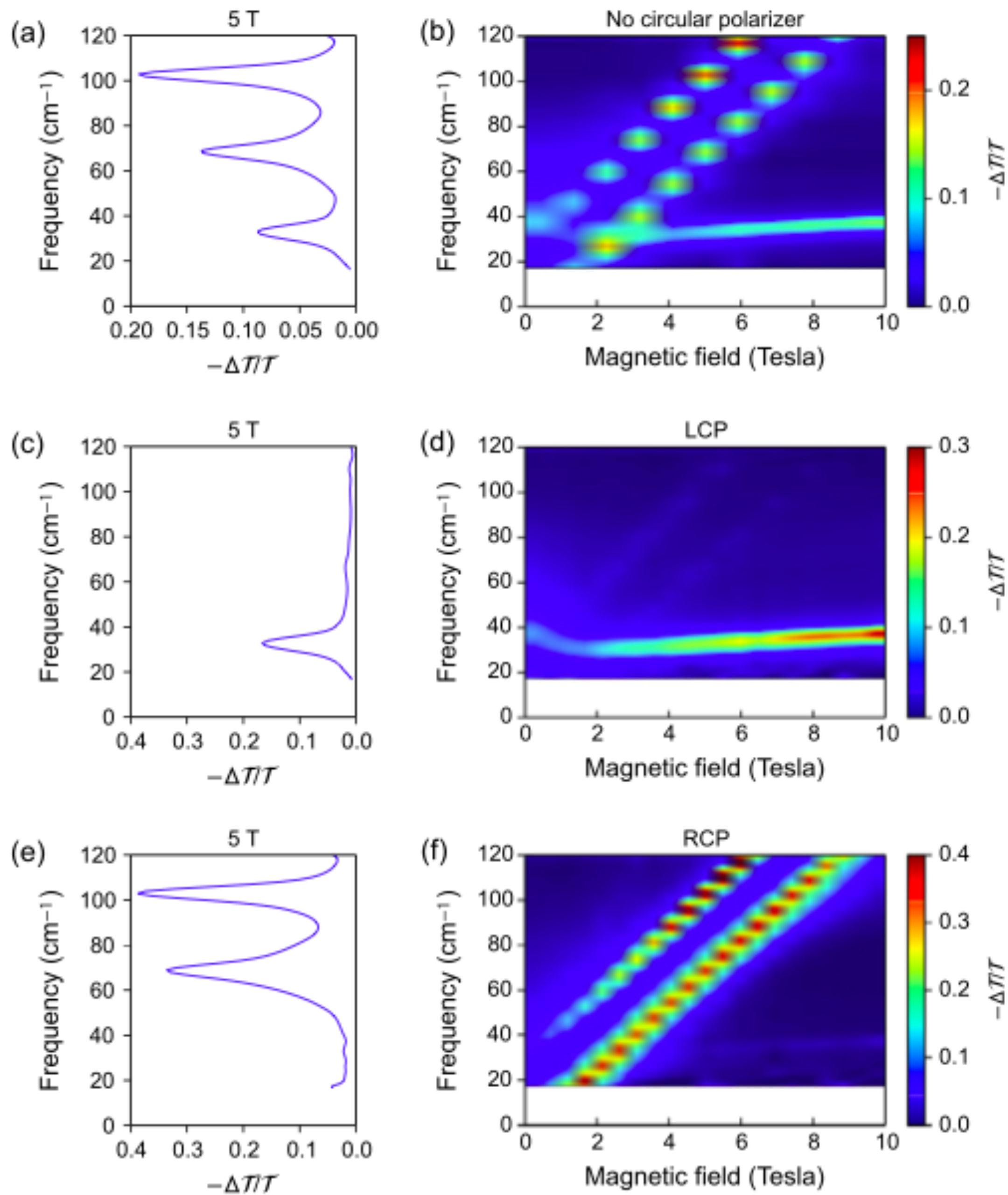

Figure 3.10 The static photo-induced transmission is shown at 5 K for an excitation wavelength of 795 nm and approximately 200 mW for different THz probe polarizations. a) and b) show the spectra for no polarizer (in 1 T increments), c) and d) show the spectra for a left circularly polarized THz probe (0.5 T increments) while e) and f) give the spectra for a right circularly polarized THz probe (0.5 T increments). Plots a), c), and e) show a single 5 T field measurement while b), d), and f) show composite spectra for applied magnetic fields from 0-10 T. Reprinted from [34], Copyright (2014), with permission from Elsevier.

exciton. As the magnetic field increases, this transition splits into two features with different field dependence and can be understood by considering the orbital momentum of the 2p exciton state. At 0 T, the 2p state quantum numbers are degenerate, but this degeneracy is lifted in the presence of the magnetic field. The selection rules governing light absorption require an angular momentum quantum number change of 1; therefore, the allowed transitions from the 1s state with 0 angular momentum are either to the $2p_{-1}$ or $2p_{+1}$ states. The circularly polarized probe distinguishes the transition states by their angular momentum change. Thus, the $1s \rightarrow 2p_{-1}$ transition is defined by an angular momentum change of -1, while the $1s \rightarrow 2p_{+1}$ and the ECR Landau level transitions are characterized by an angular momentum change of +1. [34]

Figure 3.11 shows the photo-induced spectra of GaAs at 5 T and 5 K for a range of excitation energies above and below the bandgap. From the figure, the three modes are observed to broaden and increase in intensity as the excitation energy decreases. Figure 3.12 shows the result of fitting the static photo-induced spectral modes shown in Figure 3.11 as Lorentzian oscillators. The oscillator strength and mode widths decrease with excitation energy above the bandgap of GaAs which is approximately 1.52 eV at 20 K. This likely indicates a saturation of the available states is taking place [14]. Further evidence of saturation is observed in the time-resolved spectra. Furthermore, the excitonic states decrease in strength with increased excitation energy, suggesting increased carrier momentum is disrupting the weakly bound states.

Time-Resolved Pump and Probe Spectroscopy

Transmission spectra for different time delays after photo-excitation are collected and normalized by the transmission spectra measured just before coincidence, in this case approximately 18 ns after the previous excitation pulse. The result is the photo-induced change in transmission over a spectral window from approximately 25-115 cm^{-1}. Since the stor-

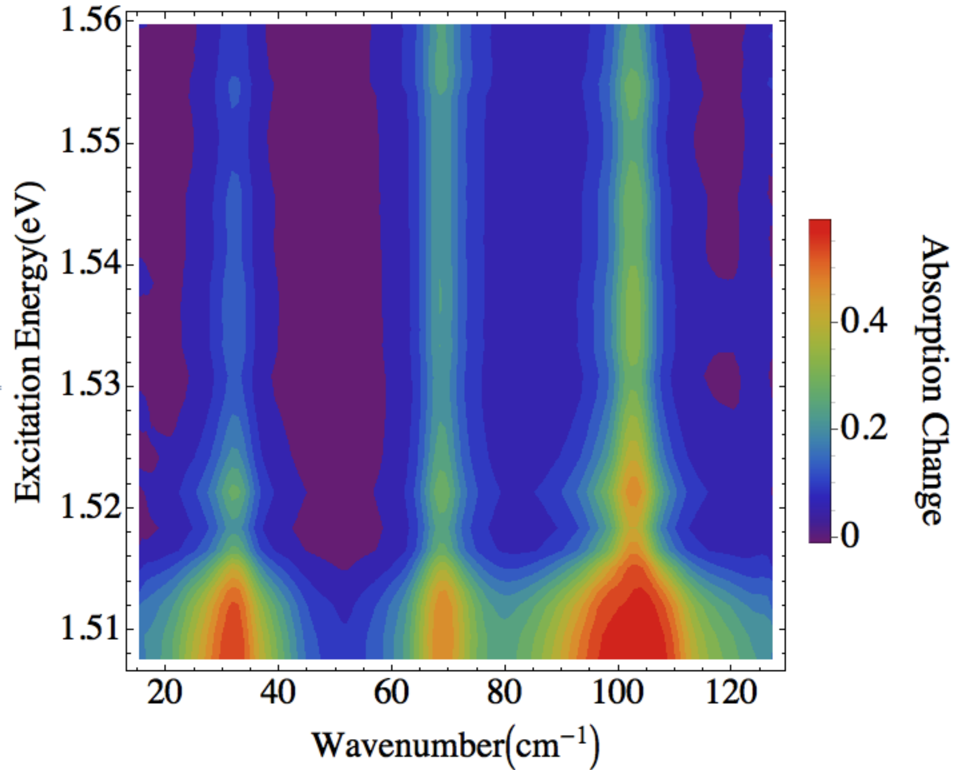

Figure 3.11 Photo-Induced Absorption Spectra of GaAs at 5 T and 5 K. The bandgap of GaAs is nominally around 1.52 eV at this temperature and significantly greater absorption and scattering are observed below the bandgap. The 1s $\rightarrow$ $2p_{-1}$ transition is located around 30 cm^{-1}, the ECR frequency is at 68 cm^{-1} and the 1s $\rightarrow$ $2p_{+1}$ transition is around 105 cm^{-1}.

age ring bunches cannot be time delayed as in a typical pump-probe experiment, the pump laser instead is triggered at pre-determined time delays with the peak in the convolution of the two pulses being defined as the zero delay. Measurements are taken for a variety of photo-excitation energies above the bandgap and for fields where the three modes are distinct within the spectral window; namely 4-6 T.

Differential Transmission of GaAs

The time-resolved differential transmission spectra at 5 T, 795 nm and 5 K are shown in Figures 3.13 and 3.14. Figure 3.13 shows the formation of the response while the Fig-

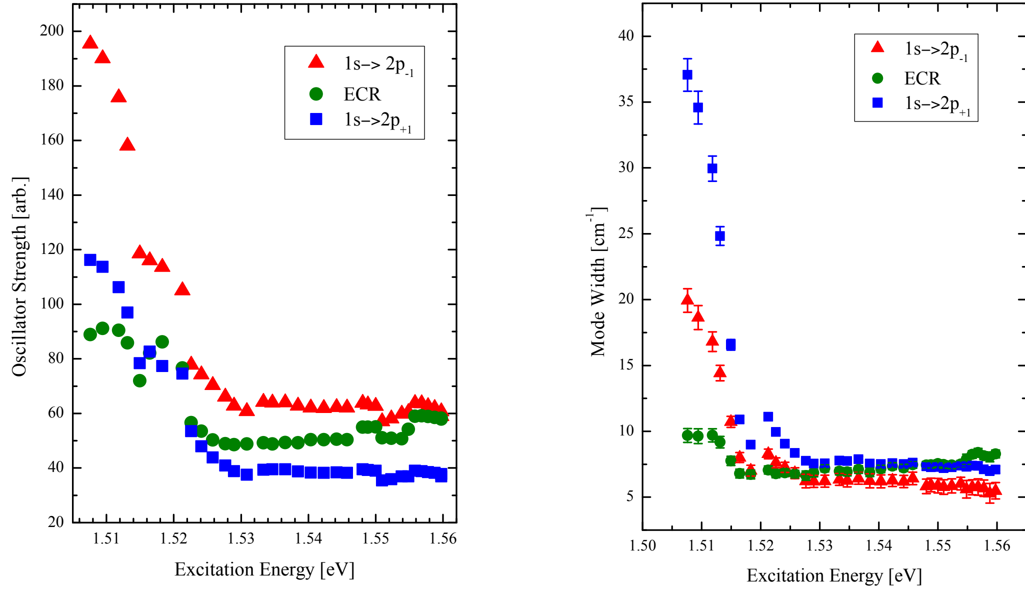

Figure 3.12 The oscillator strength and width derived from the Lorentzian oscillator fits of the photo-induced spectral modes in Figure 3.11 are shown as a function of photo-excitation energy for 5 T and 5 K. The strength and width of the modes decreases as excitation energy increases, likely the result of saturable absorption. The excitonic states experience a decrease in peak height with increased excitation energy, suggesting increased carrier momentum is disrupting the weakly bound states.

ure 3.14 shows its decay at various time delays.

The transient spectra show three modes present in the static spectra of the previous section; however, the exciton transitions clearly display bleaching of the absorption peak while the ECR mode grows in strength with photo-excitation. The bleaching suggests phase-space filling of the states involved in the transition is occurring [27]. The ECR width is observed to narrow during the first ns after excitation while the exciton modes broaden. Narrowing of the ECR mode has previously been attributed to electronic relaxation from higher Landau levels to lower ones, reducing the number of transitions contributing to the mode strength and thus narrowing the width over time [35].

The strength of the ECR transition relaxes over several ns, indicating the timescale for the

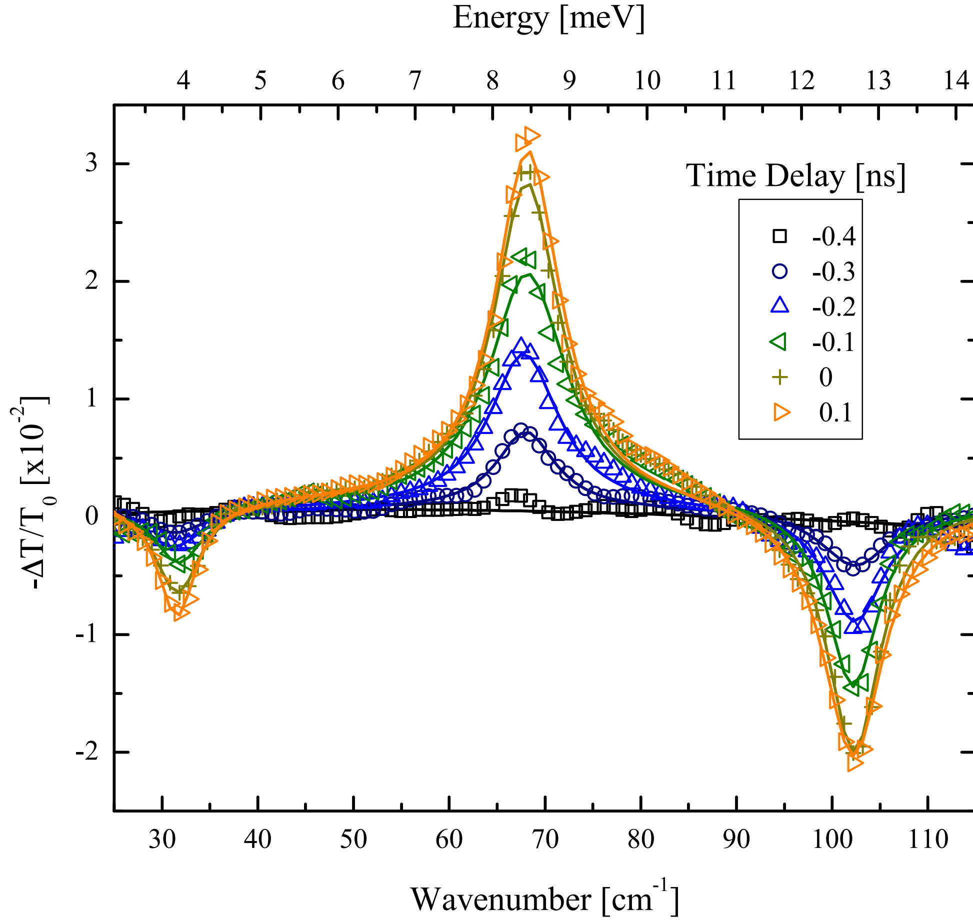

Figure 3.13 The formation of the differential transmission response at 5 T, 5 K and 795 nm. Zero time delay is defined as the ECR signal maximum. A transient bleaching is observed for the exciton transitions while the ECR mode grows in strength.

free electrons to form bound states or recombine and leave the ECR mode. Previous studies of carrier relaxation dynamics through Landau levels in Be doped GaAs indicated impurity scattering controls the relaxation rate [36].

Figures 3.15 and 3.16 show the effective mass derived from the ECR resonance as a function of time for different excitation wavelengths and applied fields. The excited carriers populate a range of Landau levels with higher effective masses and relax toward the lowest Landau level as the carriers thermalize [37]. Comparing Figures 3.15 and 3.16, it is clear

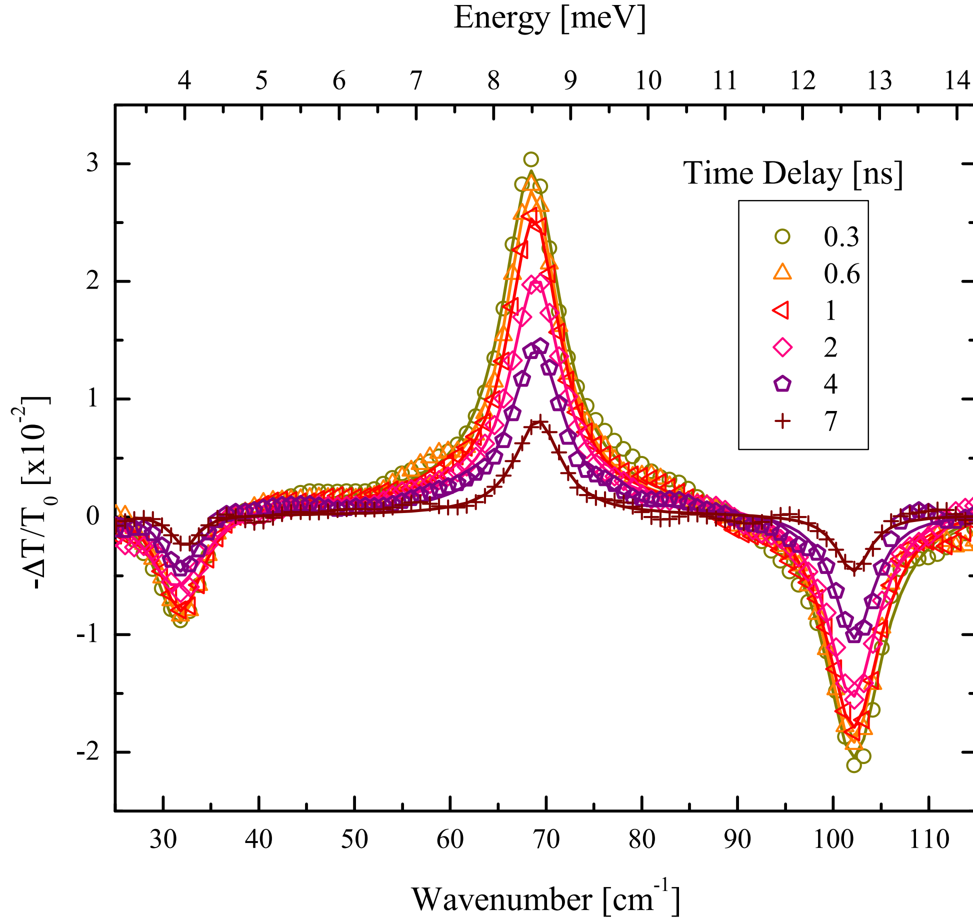

Figure 3.14 The decay of the differential transmission at 5 T, 5 K and 795 nm.

that the application of higher magnetic fields results in the population of higher Landau levels for the same excitation wavelength, consistent with the shifting of the absorption edge seen in Figure 3.6. The Landau level width is known to narrow with increasing field. This suggests for the same photo-carrier population densities and energies, electrons in higher magnetic fields occupy higher momentum states in the conduction band.

Figure 3.17 shows the oscillator strengths of the ECR and exciton transition modes as a function of time. The left side of the figure shows them as-measured, while the right side has been scaled and the bleached transitions plotted as positive to aid in comparison. Carriers in both exciton transition modes initially populate the 1s state, therefore the bleaching

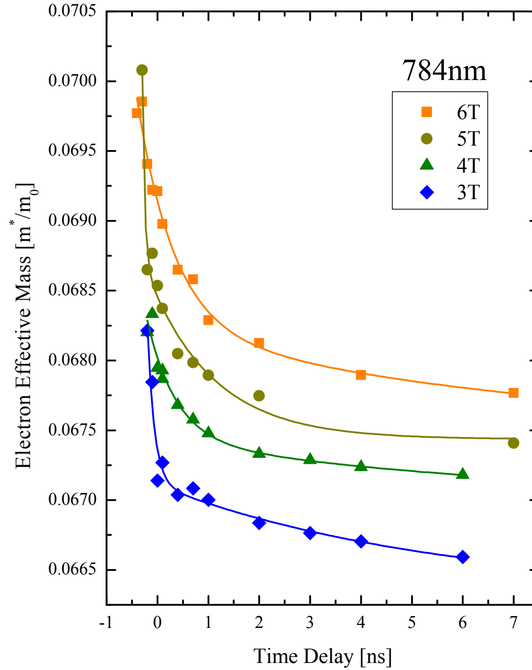

Figure 3.15 Effective mass comparison for different applied magnetic fields at 784 nm and 5 K. The effective mass values increase with increasing field, suggesting carriers are able to occupy higher energy Landau levels for the same excitation energy and the applied field increases.

observed on the left of Figure 3.17 is a result of differences in final state occupation rather than a reduction in initial state occupation. The bleached modes are observed to recover more quickly to the pre-excitation values than the ECR mode.

It can be seen on the right side of Figure 3.17 that the $1s \rightarrow 2p_{-1}$ transition maximum is delayed 1 ns relative to the peak of the ECR absorption and the $1s \rightarrow 2p_{+1}$ transition. Further, the $1s \rightarrow 2p_{-1}$ mode is still increasing in strength while the other two have started to relax. The timescale of the $1s \rightarrow 2p_{-1}$ absorption bleach suggests carriers in this bound transition are affected by the relaxation of warm free carriers through the Landau levels.

The effective mass and oscillator strength variations in time provide evidence of two relaxation pathways. Non-zero momentum transitions between Landau levels through elastic

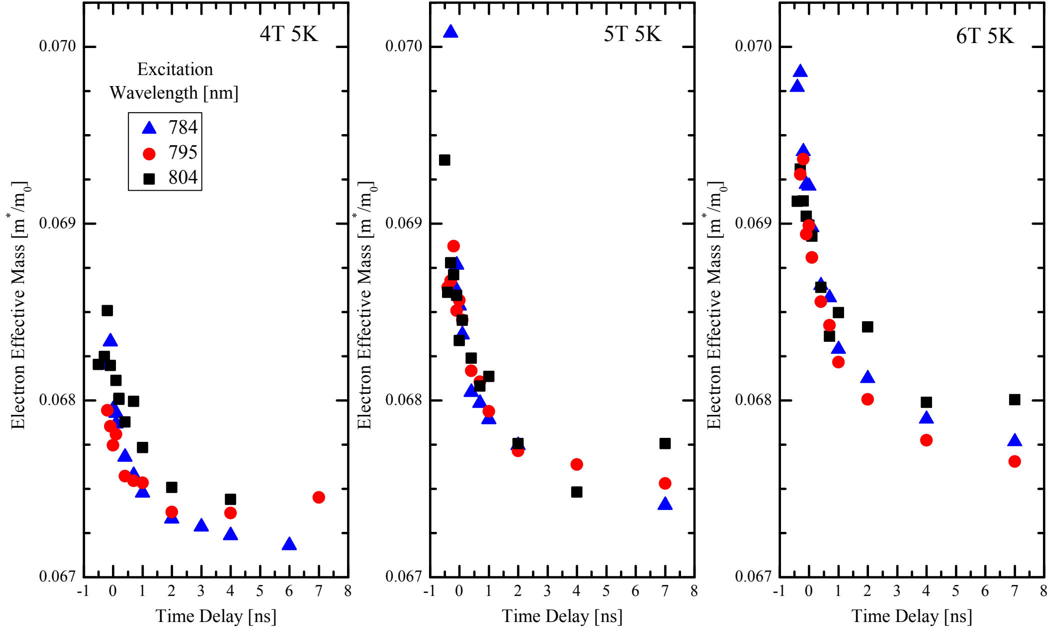

Figure 3.16 Effective mass comparison for different excitation wavelengths for applied fields of 4, 5 and 6 T at 5 K.

impurity scattering has been suggested for doped systems [36], where larger momentum changes are needed for the transition as the applied field increases. The excited carriers subsequently relax to the bottom of the Landau level through interband scattering. This explanation is consistent with the observations presented here of free carriers excited into higher momentum states as the applied field increases. The other relaxation pathway is a zero angular momentum transition to lower energy levels by resonant scattering of the free carriers with electrons bound in the 1s level. The bound electrons are then promoted to the $2p_{-1}$ level, resulting in temporary bleaching of the $1s \rightarrow 2p_{-1}$ transition from final state blocking. The subsequent relaxation steps involve lattice thermalization with the lowest bound electron levels, and is observed as the delayed bleaching of the $1s \rightarrow 2p_{-1}$ transition.

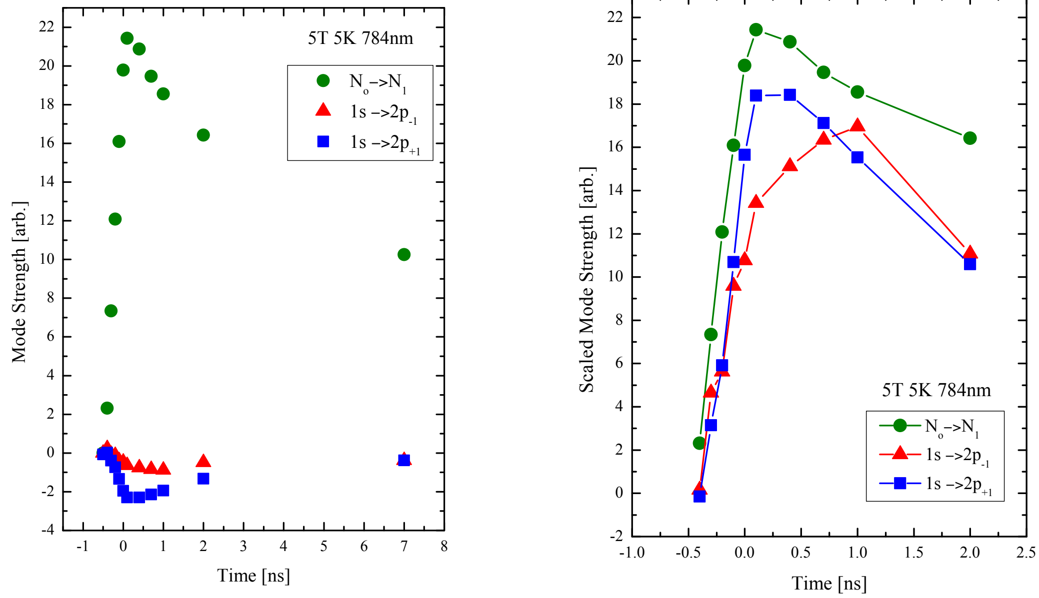

Figure 3.17 Oscillator Strengths of the ECR and exciton transitions at 5 T, 5 K, and 784 nm. The left figure shows the oscillator strengths as-measured. The right figures shows the exciton transition oscillator strengths scaled to the approximate strength of the ECR transition to aid in comparison of the time evolution of the response. The ECR and $1s \rightarrow 2p_{+1}$ transition are populated on the same timescale, while the $1s \rightarrow 2p_{-1}$ transition follows about 1 ns later.

Summary

Two distinct relaxation mechanisms through Landau levels in intrinsic bulk GaAs are observed following photo-excitation at low temperatures. The first is electronic relaxation through Landau levels and is measured through variations in the effective mass. This relaxation is observed to slow with increasing magnetic field, consistent with elastic scattering between Landau levels. The second relaxation mechanism observed is the transient bleach of the exciton transition $1s \rightarrow 2p_{+1}$ which coincides with the electronic relaxation through Landau levels. Based on the observations reported here, the bleaching of the transition is likely caused by final state blocking of the $2p_{-1}$ exciton level, which has never before been reported. This work suggests two mechanisms for electronic relaxation are occurring simultaneously.

CHAPTER 4

RELAXATION PATHWAYS IN ERAS:GAAS SYSTEMS

Nothing is too wonderful to be true if it be consistent with the laws of nature.

Michael Faraday

Introduction

Gallium arsenide is a semiconductor widely used in microwave and millimeter integrated circuits, infrared LEDs, lasers, and solar cells. Introducing ErAs nanoparticles provides a way to controllably tune the optical and electronic properties of GaAs. However, the fundamental carrier relaxation dynamics need to be fully understood in order to realize the myriad technical applications for such systems. The following systematic study characterizes the dynamics of high volume fractions (0.5-10%) of randomly distributed ErAs nanoparticles embedded in a GaAs matrix in the first few picoseconds following photo-excitation. The relaxation pathways are observed to be highly dependent on photo-carrier energy and density, as well as ErAs nanoparticle density. The results indicate the interface between ErAs and the host matrix forms an embedded Schottky barrier which acts as a trap as well as a source, injecting carriers into the GaAs conduction band. A simple model of the dynamics in a low fluence regime is presented. The array of high nanoparticle densities studied and the characterization of the relaxation pathways at multiple carrier excitation energies represents the most complete fundamental investigation of these systems to date.

Gallium arsenide is the material of choice for high speed photoconductive devices such as p-n junctions, solar cells, ultrafast optical switches, photomixers, and thermoelectric

structures [38]. Hybridized metal nanostructure/GaAs systems controlled by ultrafast optical pulses can achieve much faster switching than is attainable by phase change, voltage driven carrier injection, liquid crystals or modulation of superconductivity [39]. Interest in the embedded nanoparticle ErAs:GaAs composite system stems from the ability to control the optical and electronic properties of GaAs by incorporating semi-metallic ErAs nanoparticles without altering the position of the GaAs bandgap [40] and retaining high quality, atomically sharp ErAs/GaAs interfaces [41, 42]. The composite system displays tunable photo-carrier relaxation with ultrashort relaxation times spanning two orders of magnitude [8, 40], while achieving greater film quality [38, 43, 44, 45] and transport characteristics than LT grown GaAs [4, 7, 38, 46, 47, 48, 49, 50]. These features have made the ErAs:GaAs system highly promising for integration into GaAs-based opto-electronic devices [4, 8, 51, 52, 53, 54, 55]. However, the fundamental relaxation phenomena of these systems must be fully characterized before such applications can be realized.

To date, characterization of the relaxation dynamics in ErAs:GaAs composites has focused on optimizing ultrashort relaxation times in superlattice structures with low ErAs volume fractions as such systems show promise for THz device applications. These studies utilize the bonding differences between the ErAs rocksalt and GaAs zinc blende crystal structures, which introduce localized trap states into the bandgap of GaAs [48, 56]. The trap states act as non-radiative recombination sites for photo-excited GaAs carriers [5, 6, 8, 40], and carrier trapping times are altered by varying superlattice spacing [6, 40].

The following work elucidates the relaxation pathways in $ErAs_x$:$GaAs_{1-x}$ nanoparticle systems by focusing on the ultrafast response of single ErAs:GaAs layers. The sample geometry and high ErAs nanoparticle volume fractions give rise to the unique and unexpected optical responses observed. These systematic studies show competing relaxation effects exist in $ErAs_x$:$GaAs_{1-x}$ composites. Photo-carrier trapping by the localized interface states

and scattering of carriers from the interface states into the GaAs conduction band compete for dominance in the optical response. The strength of each component depends on the carrier momentum, availability of trap states and density of the excited carriers. The response is therefore highly sensitive to the photon energy, trap density, and carrier density. A phenomenological model of a three level system is presented which reproduces the observed carrier dynamics to a high degree of accuracy. Carrier dynamics are studied for three photon energies to identify relaxation pathways for each state in the model system.

State of Research

The growth process for these systems has been well characterized for ErAs volume fractions up to 4.5% with high levels of stability and reproducibility [9, 40, 44, 45, 51, 57, 58]. The ErAs:GaAs interface has been characterized electronically, showing evidence of Schottky diode behavior as well as significant levels of dark current [48, 55, 59, 60]. Optical characterization has been limited to superlattice structures with repeat layers of embedded ErAs nanoparticles, as these structures show promise for THz frequency devices [5, 6, 8, 40].

Growth Process

Erbium arsenide has low solubility in GaAs, leading to precipitates in the GaAs matrix [44]. The growth of ErAs nanoparticles in GaAs is driven by surface chemistry [40, 57] where the density and size of the particles may be controlled by the growth parameters: higher growth temperatures produce larger particles and greater ErAs deposition produces a higher density or reduced distance between the particles (Figure 4.1) [51, 58]. Depositing less ErAs than is required to form a complete film produces isolated nanoparticles [9]. In the low coverage regime, particle size stays roughly constant while the number of particles increases with Er deposition; however, for coverages larger than 0.5 monolayers (ML) the particles may extend laterally in the (001) plane or coalesce [9, 45].

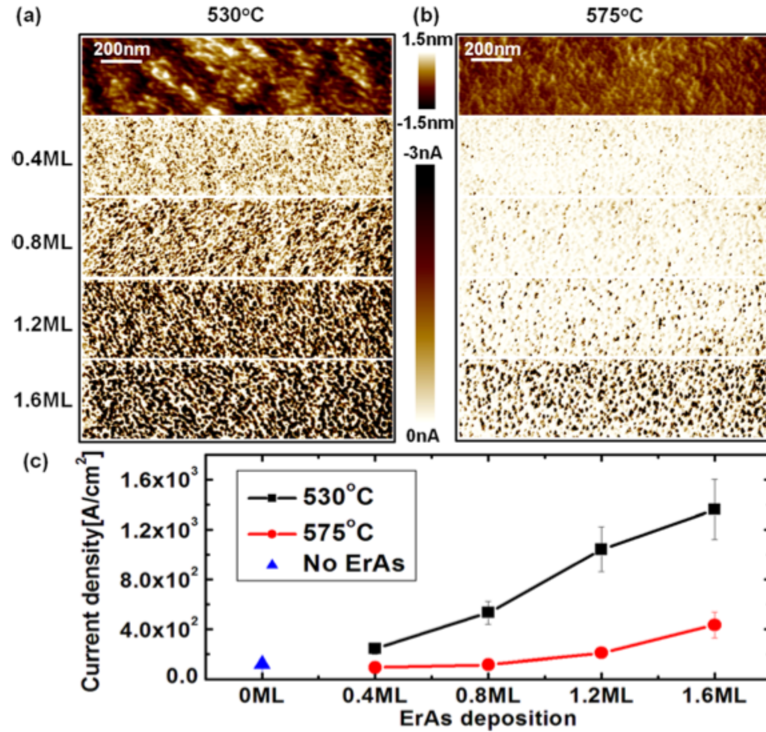

Figure 4.1 AFM and current density of varying ErAs deposition at two growth temperatures. The top panels of a) and b) show the surface topography of the 1.6 ML samples for both growth temperatures. The remaining panels show the cross-sectional TEM of 0.4, 0.8, 1.2 and 1.6 ML ErAs deposition. c) The average current density derived from multiple measurements on each sample and the GaAs reference. Reprinted with permission from [51]. Copyright 2012, AIP Publishing LLC.

The Bulk ErAs:GaAs Interface Structure

Energy band structure calculations of ErAs:GaAs indicate the composite system is not simply a superposition of the bulk GaAs and ErAs bands; the ErAs remains semi-metallic due to the presence of interface states sensitive to structural arrangement [61]. Depending on the crystallographic orientation and the structure at the ErAs:GaAs interface, the bonding character can vary significantly. The (011) interface provides nonpolar termination for both crystal structures where there are insufficient electrons to form full bonds as the tetrahedral bonding configuration of GaAs would require [48]. Therefore, the GaAs side of the interface contains dangling bonds, giving rise to a finite density of electronic states

within the bandgap corresponding to extended states on the ErAs side of the interface [48]. At the (001) interface, the polar GaAs and non polar ErAs produce two possible models of the structure exist: a Gallium-terminated ”chain” structure or an Arsenide-terminated ”shadow” structure (Figure 4.2) [48, 62]. In the chain structure, 3/4 filled Ga bonds exist across the interface and the Fermi level of the ErAs becomes pinned below the conduction band minimum at the level producing charge neutrality [48]. In the shadow model, the As bonds are partially filled and the Fermi level is pinned near the valence band maximum [48]. Fermi level pinning across the interface produces Schottky diode character where the height of the barrier can be tuned from 100-620 mV by varying composition, doping, and interface orientation [48, 55, 59, 60].

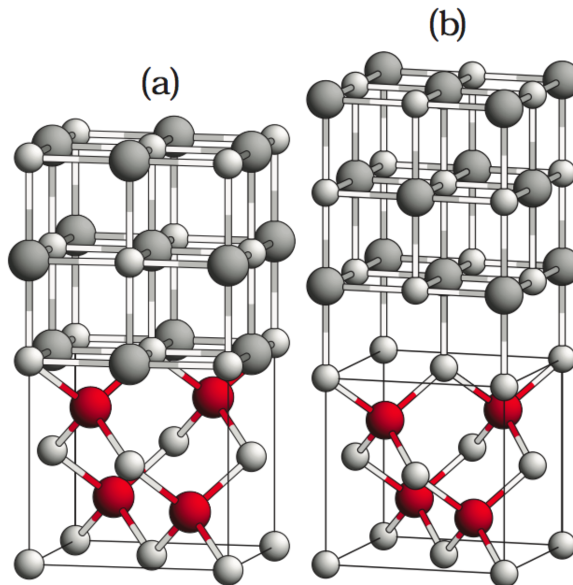

Figure 4.2 Structural model of the ErAs:GaAs (001) Interface: a) chain model (Ga dangling bond) and b) is the shadow model (As dangling bond). The white spheres are As ions, red are Er and the grey are Ga. The models represent the local structure at the interface. Reprinted with permission from [62]. Copyright 1998, AIP Publishing LLC.

The (001) direction of ErAs can be grown epitaxially on (001) GaAs with a slight distortion of the ErAs rocksalt structure [57]. ErAs lattice constant is 1.6% larger than that of GaAs, producing compressive strain [40, 63]. In-plane registry of ErAs films grown over GaAs indicates nearly perfect stacking of different crystal structures where the interface forms with Er substituting for Ga sites [43]. TEM and x-ray diffraction (XRD) analysis by multiple groups [43, 56] indicate the Arsenide-terminated shadow structure is correct, while TEM by another group [41] indicates the Gallium-terminated chain model is correct for ErAs thin films epitaxially grown on GaAs. The scanning TEM images in Figure 4.3 show the interface is atomically abrupt, with no dislocations or planar faults and the As sublattice is continuous across the interface [41]. Image contrast makes it difficult to determine the correct model from the [110] direction alone as the spacing between the Er-Ga-As triplet is near the resolution of the microscope; however in the [$1\bar{1}0$] direction the Ga-As dumbbells alternate with Er at the interfaces as expected for the chain model [41]. In addition, the [$1\bar{1}0$] interface shows Ga termination on the GaAs side (indicated by arrow) [41].

Electrical Characterization of the Embedded Nanoparticle ErAs:GaAs Interface

Semi-metallic ErAs nanoparticles act as buried Schottky barriers with overlapping depletion regions [47], potentially depleting both donors and acceptors. The Schottky barrier height is observed to increase as the number of carriers on the nanoparticles increases [59]. Differential conductivity measurements shown in Figure 4.4 indicate the presence of an interface state 0.2 eV above the GaAs fermi level which is absent in bulk and thin films of ErAs. Charges in this state are observed to decay into the GaAs matrix [56].

Previous Optical Studies of Superlattice Structures and Related Systems

For single ErAs thin films epitaxially grown on GaAs, a spectrally narrow (0.6 meV) optical absorption centered at 1540 nm exists due to intra 4f-shell transitions of the Er^{3+}

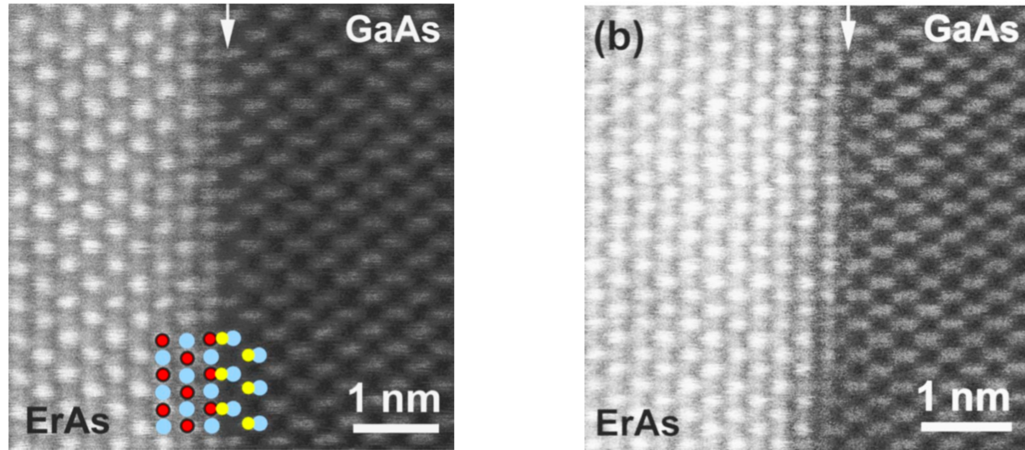

Figure 4.3 TEM images of the ErAs/GaAs interfaces. Left: High-angle annular dark-field TEM images of the ErAs/GaAs interface along [110]. The overlay represents the atomic column positions consistent with the chain model and the observed image contrast. The large blue disks represent As atoms and the small red and yellow disks represent Er and Ga, respectively. Right: High-angle annular dark-field TEM image of the ErAs/GaAs interface along [$1\bar{1}0$]; perpendicular to [110]. The arrows mark the positions of the last Ga atoms in the semiconductor. Reprinted with permission from [41]. Copyright 2005, AIP Publishing LLC.

electrons [64]. In contrast, when the ErAs is embedded in GaAs-based semiconductors, Er^{3+} luminescence is noticeably absent [47]. Instead, the incorporation of ErAs introduces localized states into the compound semiconductor bandgap, creating non-radiative decay channels which significantly reduce the carrier relaxation time.

The ultrafast optical response of several ErAs:compound semiconductor systems is summarized. Evidence is given to support excited carriers being captured by the localized states within the first few ps of excitation. The response of the systems to photo-excitation varies little with photon energy and the carrier capture times may be tuned by varying the spacing between ErAs nanoparticle-incorporated layers.

The first study discussed measured the optical conductivity of a GaAs reference wafer and ErAs:GaAs nanoparticle composites in a superlattice geometry using the optical pump-THz

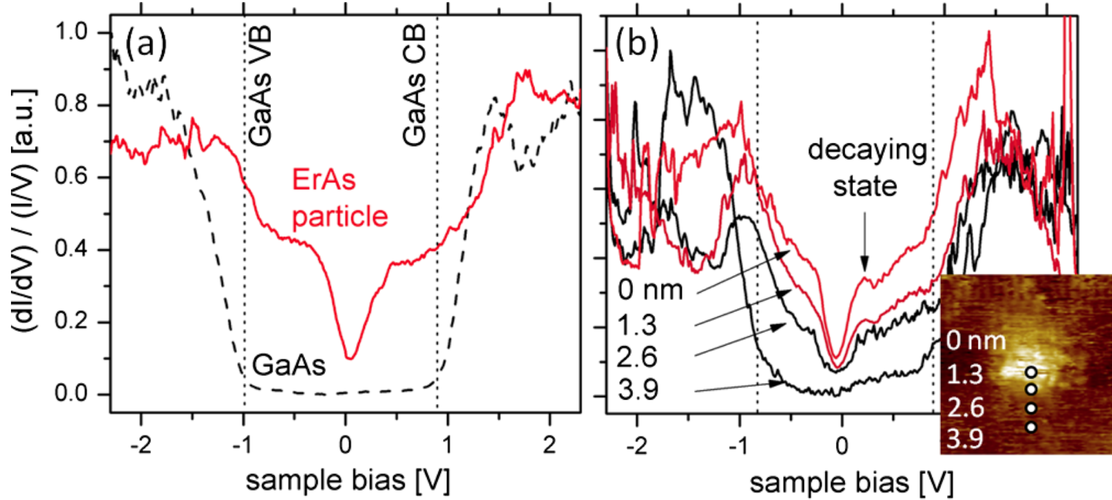

Figure 4.4 Differential conductance of embedded ErAs nanoparticles. (a) Averaged Differential Conductance for ErAs nanoparticles and the GaAs matrix. (b) Individual differential conductance spectra directly above a nanoparticle and moving in incremental steps into the GaAs matrix. The arrow in part (b) indicates the location of the interface state which is not present in the separate GaAs or ErAs nanoparticle spectra (a). Reprinted figure with permission from [56]. Copyright 2011 by the American Physical Society.

probe technique. Figure 4.5 shows the change in electric field and the optical conductivity for the GaAs reference following 1.55 eV excitation at room temperature. The results indicate a long-lived carrier population is excited by the above the GaAs bandgap and is slowly evolving to the pre-pump state after 500 ps. In contrast, Figure 4.6 shows the change in electric field and optical conductivity of ErAs:GaAs superlattices for two different superlattice spacings: L=25 nm on the left and L=50 nm on the right. The ErAs:GaAs conductivity measurements indicate rapid trapping of carriers excited in GaAs and trapped by the ErAs nanoparticles on a sub-ps time scale. The trapping is characterized by a single exponential decay and the carrier lifetime increases for the larger ErAs layer spacing. The mobilities of the ErAs systems are comparable to the GaAs mobilities, indicating pump induced changes in the optical conductivity are the result of carrier density changes. The time dependent carrier density is given as $N(t)=N_0e^{-t/\tau}$ and the carrier densities in the ErAs systems return to pre-pump values within the first few ps. Additionally, the carrier capture times increase

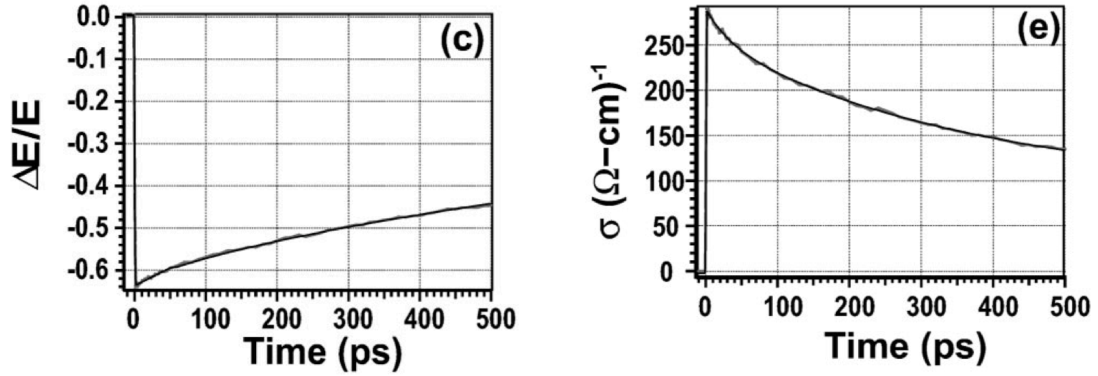

Figure 4.5 Optical-pump THz-probe of GaAs reference. Left: Normalized change in the electric field strength for the GaAs reference with a pump fluence of 19 μJ/cm^2. Right: Induced conductivity as a function of time delay for 1.55 eV excitation. Reprinted with permission from [6]. Copyright 2005, AIP Publishing LLC.

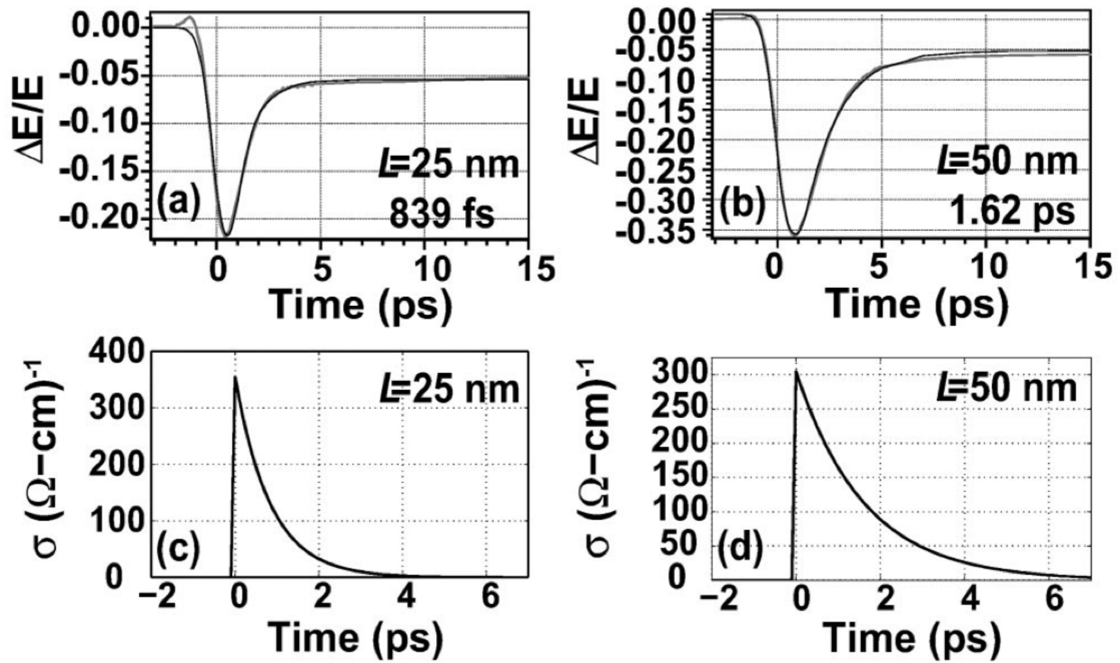

Figure 4.6 ErAs:GaAs superlattice optical pump-THz probe response for 1.55 eV excitation. a) Change in electric field strength for L=25 nm sample. b) Change in electric field strength for L=50 nm sample. c) Conductivity vs time for L=25 nm sample. d) Conductivity vs time for L=50 nm sample. Reprinted with permission from [6]. Copyright 2005, AIP Publishing LLC.

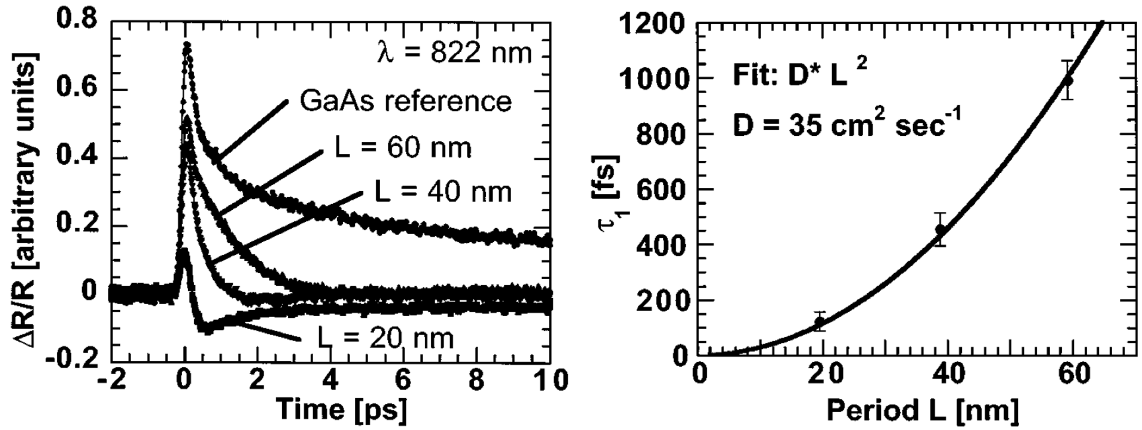

Figure 4.7 ErAs:GaAs superlattice transient reflectivity. Left: ErAs:GaAs superlattice differential reflectivity change for different superlattice periods *L*. Right: ErAs:GaAs superlattice time constant of initial transient decay as a function of superlattice period *L*. Reprinted with permission from [40]. Copyright 1999, AIP Publishing LLC.

with the pump fluence as the nanoparticles saturate, resulting in more excited carriers remaining in the GaAs conduction band at early times and contributing to the THz signal until being captured. [6]

The left side of Figure 4.7 shows the ultrafast optical pump-probe response of ErAs:GaAs superlattices grown with varying distances between superlattice periods but otherwise identical conditions. The degenerate pump-probe reflectivity response at 1.509 eV shows a significant alteration of the response from the GaAs reference with superlattice layer spacing. The GaAs reference maintains a large reflectivity signal within the time window which is attributed to initial carrier thermalization, followed by cooling of hot carriers to the conduction band edge and subsequent recombination. The ErAs systems show an initial positive transient, followed by a reduction to values close to the baseline within a few ps. The superlattice spacing alters both the magnitude of the response as well as the decay time of the initial transient, with the shortest spacing displaying a negative transient. The ErAs containing samples show GaAs-like excitation initially, but the photo-carriers are then captured by the ErAs nanoparticles which results in the transient decay. The data are fit with

exponential functions to extract the time constants. The decay time constant is shown on the right of Figure 4.7 and the error bars are the variation of the measured time constants with wavelength. Two possible explanations for the increased carrier capture time with superlattice period are given: 1) the number of capture sites per unit length increases with superlattice period which assumes the occupation of the capture site is the limiting factor in capture time and 2) as the period increases, the carriers need more time to reach the capture sites with travel time being the limiting factor. The quadratic fit shown on the right of Figure 4.7 is consistent with the diffusion explanation, however it is acknowledged as too simplistic. [40]

Further work on the ErAs:GaAs system indicates the intrinsic carrier capture time can be tuned from 190 fs to 17 ps by changing only the GaAs superlattice spacer layer thickness from 10 nm to 400 nm. The authors explain the capture of exited carriers in a two step process: diffusion toward the ErAs nanoparticle plane and subsequent carrier capture. However, a simple diffusion model does not accurately fit the observed carrier capture times and the cause of the deviation remains elusive. [8]

In ErSb:GaAs superlattices, the carrier lifetime is found to depend on the distance between the superlattice layers, the ErSb deposition amount and ErSb nanoparticle size. Probed at 1550 nm, the ErSb:GaAs superlattices display a change in slope with relaxation time as seen in Figure 4.8 for different superlattice periods. The time constants τ_1 and τ_2 derived from this data are attributed to a fast initial carrier decay and secondary recombination, respectively. Both lifetimes are observed to increase with layer thickness in Figure 4.9d. Samples containing more than 0.5 ML of ErSb contained no evidence of the secondary recombination τ_2, likely the result of efficient capture [65].

AFM images of two of the samples grown at different rates (0.04 ML/s (i) and 0.09 ML/s

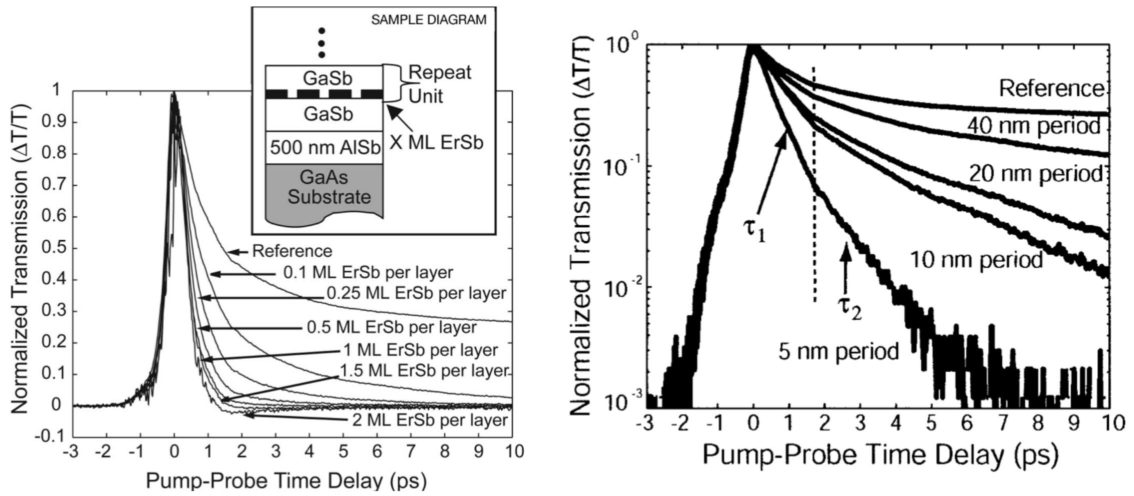

Figure 4.8 Left: ErSb:GaSb superlattice normalized differential transmission for different ErSb depositions in a 30 period, 20 nm spacing superlattice. The inset shows the sample structure. Right: ErSb:GaSb superlattice normalized differential transmission for different layer spacings in a 620 nm thick ErSb/GaSb superlattice with 0.1 ML of ErSb per layer. The number of periods is adjusted to maintain a constant thickness and thus increases the density of ErSb particles. The left side of the dashed line is fit to obtain τ_1 and the right side is fit to obtain τ_2. Reprinted with permission from [65]. Copyright 2004, AIP Publishing LLC.

(ii)) are shown in Figure 4.9 where the same lattice period and total ErSb deposition of 0.75 ML are maintained. The faster growth rate results in higher densities of smaller particles while the slower growth rate produces larger, sparsely distributed particles. The lifetime of the samples with different growth rates is shown in Figure 4.9b and shows that the smaller, dense distributions of nanoparticles have shorter lifetimes. Figure 4.9c contains the lifetime as a function of ErSb deposition per layer. The carrier lifetime decreases to an apparent minimum value on the order of the measurement resolution. [65]

Based on the above studies, the results from single layer ErAs:GaAs systems are anticipated to show shorter carrier lifetimes for higher ErAs deposition as the inter-particle spacing will decrease. No significant excitation wavelength dependence or dynamic processes other than carrier trapping and thermalization are expected. Using a single ErAs layer geometry should eliminate the inter-ErAs layer diffusion process from the dynamics.

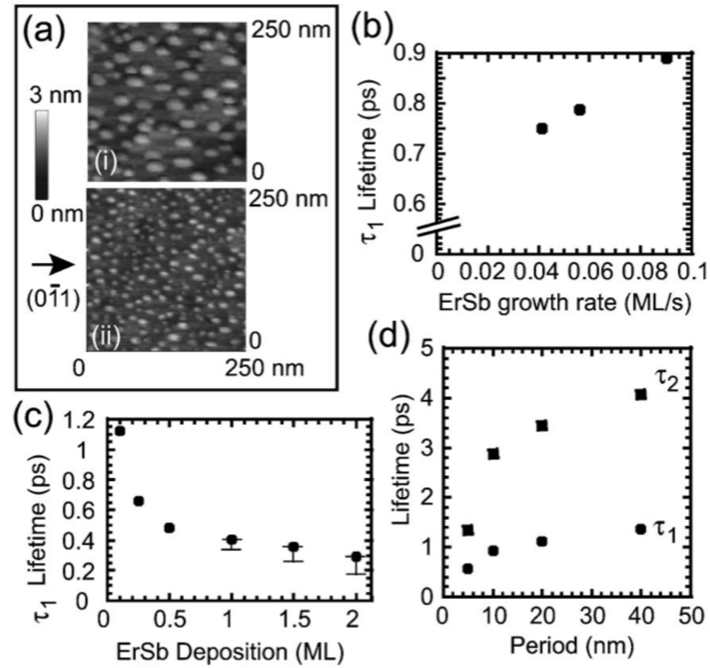

Figure 4.9 a) Atomic force microscopy image of 0.75 ML deposition of uncovered ErSb islands on GaSb grown at (i) 0.04 ML/s and (ii) 0.09 ML/s. b) The calculated lifetime τ_1 plotted as a function of growth rate for 0.5 ML ErSb per layer in a 30 period, 20 nm spacing superlattice. c) The calculated lifetime τ_1 plotted as a function of ErSb deposition per layer for a 30 period, 20 nm spacing superlattice. d) The calculated lifetimes τ_1 and τ_2 plotted as a function of period spacing in a 620 nm thick superlattice with 0.1 ML of ErSb per layer. Reprinted with permission from [65]. Copyright 2004, AIP Publishing LLC.

Single Layer ErAs:GaAs Dynamics

The dynamics of single layer ErAs:GaAs are significantly different from those reported in superlattices and related Er compound semiconductor systems. Longer carrier lifetimes are observed with increasing ErAs deposition. Significant wavelength dependence is observed and suggests a previously unreported dynamics process is taking place.

Sample Structure and Growth

The $ErAs_x$:$GaAs_{1-x}$ is fabricated by collaborators in the Palmstrøm group at the University of California, Santa Barbara. The composite samples are grown in a Vacuum Generator

V80H molecular beam epitaxy (MBE) chamber on a commercial GaAs wafer. The wafers were bonded to molybdenum sample holders using indium. The growth conditions have been detailed elsewhere [56]. The ErAs nanoparticles self-assemble [7, 9, 40, 47, 52] with particle size and density independently tunable during the growth process [6, 40, 58]. The growth temperature is held constant at 540°C during deposition, producing nanoparticle diameters of about 2 nm [51, 53, 56] for low volume fractions. Each composite sample consists of a semi-insulating substrate GaAs (001); 250 nm GaAs buffer; 300 nm of randomly distributed $ErAs_x$:$GaAs_{1-x}$ embedded nanoparticle layer grown by simultaneous co-deposition of Er, Ga and As; followed by a 10 nm GaAs capping layer to prevent oxidation (Figure 4.11a: inset). The composite layers have ErAs volume fractions of x = 0 to 10%. The $ErAs_x$:$GaAs_{1-x}$ compositions are calibrated by reflection high energy electron diffraction (RHEED) oscillations on ErAs and GaAs calibration samples. Before the optical measurements, the samples are unmounted and the back sides are mechanically polished to remove the indium used during bonding. The 0% volume fraction is used as an additional reference to ensure the observed response is not due to the growth conditions, including the possible presence of residual indium from the bonding layer on the back surface.

Experimental Details

The absorption data are acquired by spectroscopic ellipsometry and have been vertically offset for clarity. For the time-resolved measurements, the output of a mode-locked 76 MHz Ti:Sapphire laser with approximately 150 fs pulses is divided into cross-polarized pump and probe beams. The probe beam is time delayed relative to the amplitude-modulated pump beam, and a lock-in detection scheme is used (see Figure 4.11b). The pump is incident normal to the sample surface and the probe is incident at 20° to the surface normal. The probe fluence is held constant at 0.5 μJ/cm^2 throughout all measurements. The PPR signal is given as the relative change in reflectivity induced by the pump pulse over the background reflectivity measured by the probe ($\frac{\Delta R}{R_0}$) with a signal strength on the order of

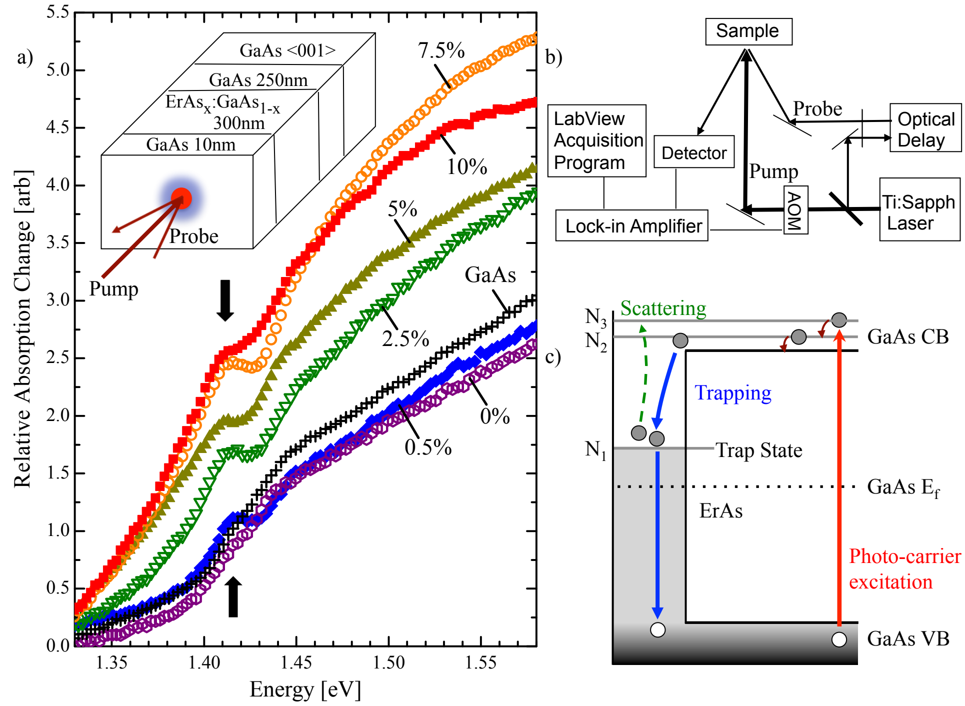

Figure 4.10 Absorption and Sample Structure of the ErAs$_x$:GaAs$_{1-x}$ composite system. a) Relative static absorption obtained by ellipsometry for ErAs$_x$:GaAs$_{1-x}$ with $x = 0 - 10\%$ and intrinsic GaAs. The black arrows indicate the location of the absorbing features in the band tails. The room temperature GaAs bandgap is located around 1.42 eV. Inset: Schematic (not to scale) of the composite sample structures for $x = 0 - 10\%$. b) Diagram of the degenerate pump probe experimental setup. c) 1D cut through the ErAs nanoparticle and GaAs matrix illustrating proposed dynamics in the composite system where the conduction band (CB) and valence band (VB) of GaAs are shown and the ErAs/GaAs interface gives rise to a Schottky trap within the bandgap and above the GaAs Fermi level (E_f). The shaded areas indicate electron occupation and the arrows illustrate the dynamic carrier processes.

10^{-3}. Data are fit using multiple exponential functions to extract time constants, with the error bars as indicators of fit uncertainty.

The PPR response of a semiconductor measures the relative change in the complex index of refraction induced by optically excited carriers and evolves as carrier densities and energies change. The signal shape depends on the relaxation pathways present for carrier cooling and population decay, while the sign of the response depends on the probe energy relative

to the bandgap [21, 22]. The measurements are all conducted in a low fluence (linear) regime [15] and therefore not likely to induce Auger, nonlinear, or multi photon absorption effects. The pump and probe measurements sample the change in carrier population excited by the pump but detected within the spectral frequency range of the probe. For the case of degenerate pump and probe, the method is a direct measurement of the population evolution at the excitation energy. The measurement resolution is limited by the pulse width of the laser and the accuracy of the optical delay line. The maximum time resolution of the experimental system described is approximately 0.25 ps.

Results and Discussion

The relative static absorption of the samples is shown in Figure 4.11a for the GaAs fundamental absorption edge and band tails at 300K. The x = 0% $ErAs_x$:$GaAs_{1-x}$ displays a softening of the band edge with respect to the commercial GaAs reference. An additional absorption feature within the band tails is seen in the ErAs-containing samples (indicated by the black arrows in Figure 4.11a). This increased absorption feature is attributed to the ErAs nanoparticles as it is noticeably absent in either the 0% or GaAs absorption spectra. The slope of the band tails is also observed to increase with ErAs incorporation. The presence of these absorption features and their effects on the dynamics of the system are presented and discussed below.

Figure 4.11c is a cartoon of the proposed system dynamics in the vicinity of an ErAs nanoparticle based on the experimental results. The interface between the ErAs and GaAs matrix forms a localized trap state [48, 56] through which photo-excited carriers can non-radiatively recombine or scatter back into the GaAs conduction band given sufficient momentum [38]. The composite systems are modeled as three discrete energy levels (see cartoon Figure 4.11c) and the relaxation of the excited carrier population is given by coupled rate equations. Only the evolution of photo-carriers after the zero time delay is considered,

with nonlinear and many-body effects neglected. The possibility of defects is also ignored as the systems are high quality and display no evidence of defects [41, 42]. The absorption is taken into account with different initial populations for the states, depending on photoexcitation energy and ErAs volume fraction. The energy levels are the interface trap state N_1; a cool carrier/low energy state near the GaAs conduction band edge N_2; and a hot carrier/high energy GaAs conduction band state N_3. Carriers in these states may either relax through normal decay channels in the GaAs conduction band states (positive contribution to overall PPR signal), or they may be captured by the trap state (negative contribution to signal). Carriers populating the trap state may non-radiatively recombine or scatter into the GaAs conduction band state N_2 (positive contribution to the overall PPR signal). τ_1 is the scattering time for carriers to move from the trap state N_1 to the GaAs conduction band edge N_2, τ_2 is the GaAs band edge thermalization time, τ_3 is the GaAs hot carrier population decay time and τ_4 is the effective carrier trapping time. Values of τ_i are taken from the experimental data and the strength terms A$_i$ are used as fitting parameters. For $\tau_{2,3} = 0$, the model produces the response of the GaAs reference sample.

$$\frac{dN_3}{dt} = -(A_3 \exp[\frac{-t}{\tau_3}] + A_4 \exp[\frac{-t}{\tau_4}])N_3[t] \tag{4.1}$$

$$\frac{dN_2}{dt} = A_3 \exp[\frac{-t}{\tau_3}]N_3[t] - A_2 \exp[\frac{-t}{\tau_2}]N_2[t] + A_1 \exp[\frac{-t}{\tau_1}]N_1[t] \tag{4.2}$$

$$\frac{dN_1}{dt} = A_4 \exp[\frac{-t}{\tau_4}]N_3[t] - A_1 \exp[\frac{-t}{\tau_1}]N_1[t] \tag{4.3}$$

The simulated response of the composite systems is compared to the experimental results as a means of verifying the relaxation dynamics.

Figure 4.11a shows the PPR of the GaAs reference and $ErAs_x$:$GaAs_{1-x}$ systems photoexcited below the bandgap at 1.38 eV. The GaAs transient is the result of excited defects or surface states which decay nearly instantaneously, and is therefore neglected in the analy-

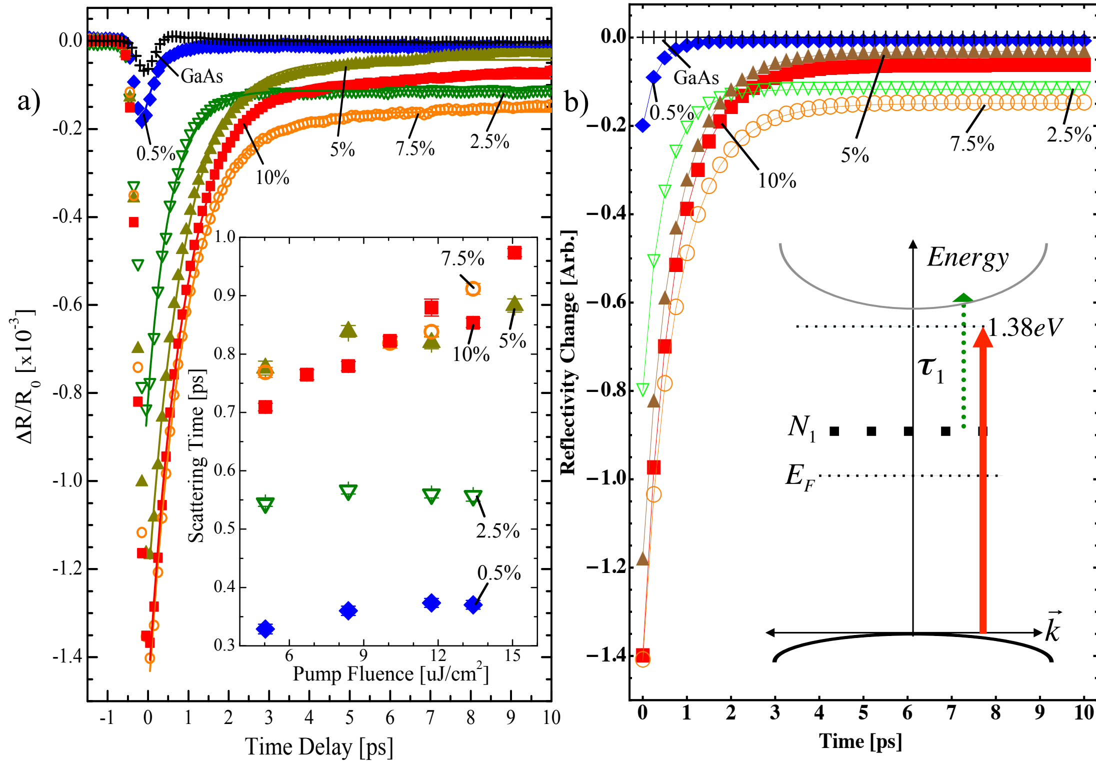

Figure 4.11 Spectral response at 1.38 eV. a) Differential reflectivity response for x=0.5-10% volume fractions of $ErAs_x$:$GaAs_{1-x}$ and the GaAs reference for a pump fluence of approximately 13 μJ/cm^2 at 1.38 eV. The solid lines are exponential fits used to extract the time constants. Inset: Carrier scattering times as a function of pump fluence from experimental spectra. b) Simulations of the system using experimentally derived time constants at 1.38 eV with scattering from the trap state to the GaAs conduction band. Symbols are included to aid comparison of simulated and experimental curves. Inset: Diagram of the model system where the N_1 is the trap state and τ_1 is the scattering time constant. The excitation energy is below the GaAs conduction band edge; therefore, the simulated response is achieved by direct population of the trap state with carriers scattering into the GaAs conduction band edge.

sis. The responses of the ErAs containing samples are significantly longer lived than the GaAs reference and increasingly negative with ErAs incorporation. The interface between semi-metallic ErAs and semiconducting systems are known to create interface potentials, or Schottky barriers [4, 55, 59, 60], with different barrier heights depending on the crystallographic directions of the interface [66]. The excitation energy is not sufficient to excite carriers across the GaAs bandgap; therefore, the initial response at zero time delay is the re-

sult of carriers excited from the GaAs valence band directly into the trap states or optically excited ErAs carriers. The excitation energy is above the resonance energy for the trap level; producing excess carrier momentum and enabling scattering into the GaAs conduction band edge within a few ps of excitation [38, 67]. The magnitude of the PPR response at 1.38 eV suggests a correlation between the density of trap states and the ErAs volume fractions exists. For the 0.5 and 2.5% volume fractions, the PPR response approaches a non-zero value after the first few ps which is different from the pre-excitation value.

The population of scattered carriers evolves with a single time constant shown as a function of pump fluence in the inset of Figure 4.11a. The scattering times for the 0.5 and 2.5% volume fractions have little fluence dependence while the 5-10% volume fractions show a linear increase in scattering time with pump fluence. The lack of fluence dependence, combined with the non-zero PPR response after the initial decay for the 0.5 and 2.5% volume fractions indicates the traps for these systems are saturating. The higher volume fractions have larger numbers of traps available (larger PPR magnitude) and can accommodate significantly larger carrier populations before scattering occurs. The scattering times for the higher volume fractions increase with fluence, suggesting the systems have not reached a saturation level.

The simulation results in Figure 4.11b show the relaxation of carriers initially populating only the N_1 interface trap state. Trapping behavior was neglected in the simulation as it was not directly observed in the evolution of the PPR response at 1.38 eV. Carriers in the trap states (excited from the GaAs valence band or the metallic ErAs carriers) scatter into the GaAs conduction band N_2. The recombination of carriers scattered into the conduction band occurs at significantly longer timescales and is beyond the scope of the present work. The simulation results indicate the 0.5 and 2.5% volume fractions are exhibiting saturation of available states as the response is non zero after the first few ps. This is consistent with

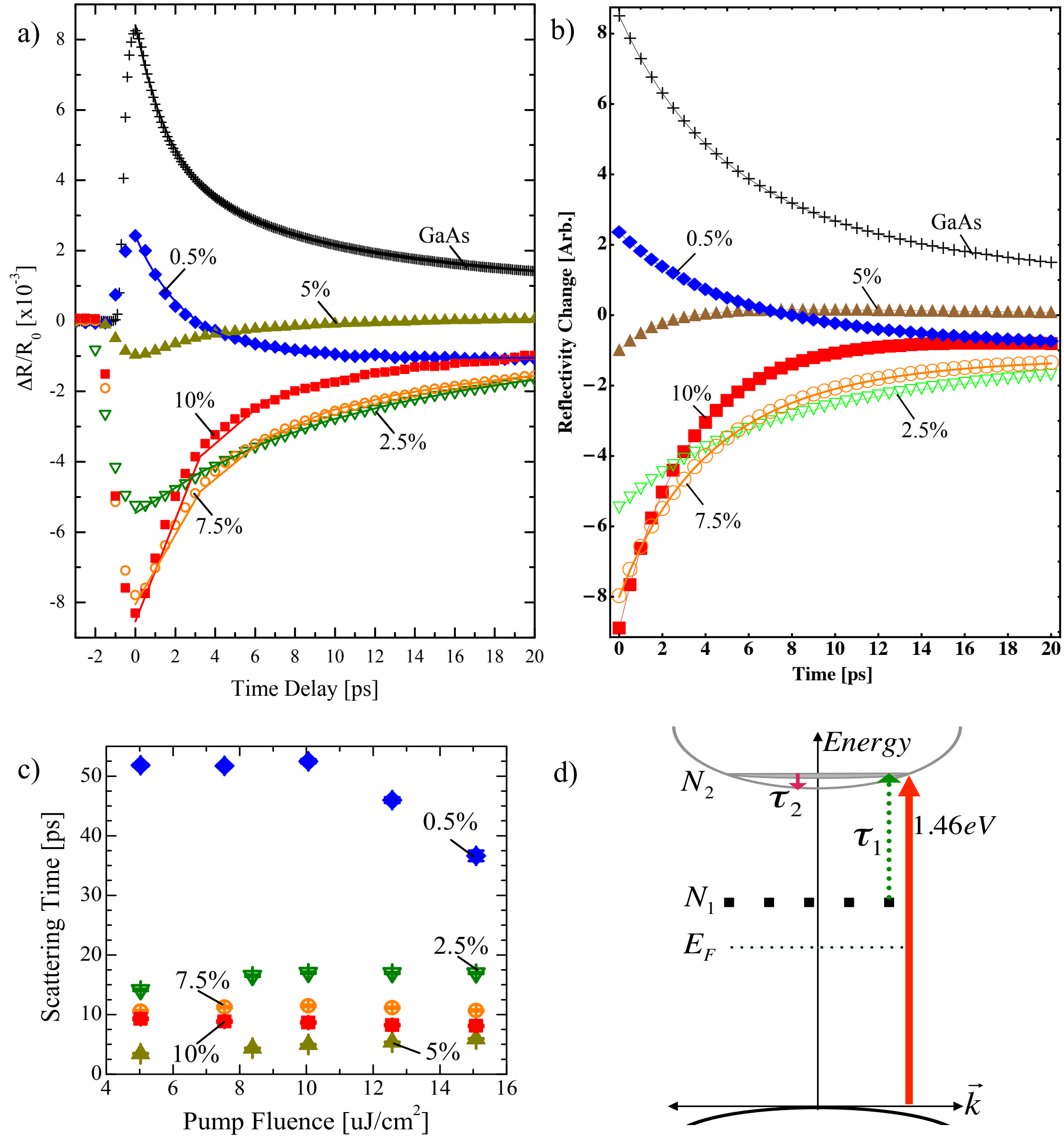

Figure 4.12 Spectral response at 1.46 eV. a) Differential reflectivity response for x=0.5-10% volume fractions of $ErAs_x$:$GaAs_{1-x}$ and the GaAs reference for a pump fluence of approximately 15 μJ/cm^2 at 1.46 eV. The solid lines are exponential fits used to extract the time constants. b) Simulations of the system using experimentally derived time constants at 1.46 eV. c) Carrier scattering times at 1.46 eV derived from experimental data as a function of pump fluence. d) Diagram of the model used in the simulation in (b) with the GaAs conduction band state N_2 at 1.46 eV, Schottky trap state N_1, GaAs band edge thermalization τ_2, carrier trapping τ_1 and scattering τ_4.

the constant scattering times shown in the inset of Figure 4.11a. The increase in scattering time with fluence for the 5-10% volume fractions suggests large populations of carriers are excited and the available states are sufficient.

The measurement and simulation of the ErAs:GaAs composites at 1.38 eV indicates scattering dominates the relaxation dynamics for excitation below the bandgap. While trapping behavior may exist, it is not observed directly on these timescales. Excited carriers initially populate the trap level, with increased carrier densities producing a more negative response. The excited carriers readily scatter from the trap level to the GaAs conduction band as a result of excess carrier momentum. For lower volume fractions, the available relaxation pathways saturate due to the extra carriers introduced from the ErAs. Higher volume fractions do not exhibit saturation of relaxation pathways even though carrier densities are higher, providing indirect evidence of an increase in trap density with ErAs volume fraction.

Figure 4.12a shows the response of each sample excited at 1.46 eV just above the GaAs conduction band edge. The GaAs reference PPR response is characterized by carrier and lattice thermalization [1]. The $ErAs_x$:$GaAs_{1-x}$ responses show markedly different behavior from the GaAs reference within the first 20 ps. The response is increasingly negative with ErAs incorporation at the zero time delay, and a subsequent slow positive rise can be seen.

The initial negative transient is ascribed to the trapping of carriers photo-excited in the GaAs by the interface states [5, 6, 8, 40]. Except for the 0.5%, the ErAs containing systems all display essentially instantaneous trapping within the resolution of the present experiment. The negative initial transients indicate the higher volume fractions have sufficient trap states available to capture the excited carriers. In contrast, the 0.5% system displays GaAs-like excitation followed by a slow negative transient, likely the result of saturated of

the trap states.

The slow positive rise for the 2.5-10% composites is attributed to scattering from the trap state to the GaAs conduction band. The relatively slow time evolution after photo-excitation implies the formation of low energy carrier distributions. The scattering times τ_1 associated with the positive PPR contribution at 1.46 eV are shown in Figure 4.12c. The scattering times observed at 1.46 eV are significantly longer than at 1.38 eV, suggesting the accumulation of a significant population of photo-carriers at the trap states is necessary for scattering to occur as carriers are not directly excited into the trap level. The lowest volume fraction shows a decrease in scattering time with fluence. As the PPR for the 0.5% system indicates the traps are already saturated, the faster scattering time with higher carrier densities reveals the scattering time depends on the photo-carrier density as well as the carrier momentum and trap density. The 2.5-10% systems show no clear fluence dependence at this excitation energy, suggesting significant carrier populations exist in the trap states even for low fluences.

Figure 4.12b contains the simulated response of the ErAs:GaAs composites at 1.46 eV. In order to produce the results shown in Figure 4.12b, carriers initially populate the trap states for the $ErAs_x$:$GaAs_{1-x}$ systems. The 0.5% and GaAs reference have initial carrier populations in the conduction band edge. This implies that while the 0.5% exhibits GaAs-like carrier excitation, the higher volume fractions trap photo-carriers nearly instantaneously upon excitation. Once a significant carrier population has accumulated in the trap state, scattering dominates the response.

Excitation at 1.55 eV shown in Figure 4.13a creates photo-carriers high in the GaAs conduction band giving rise to the sharp positive peak in the PPR response resulting from optical phonon emission followed by carrier thermalization [21, 1]. All of the composite

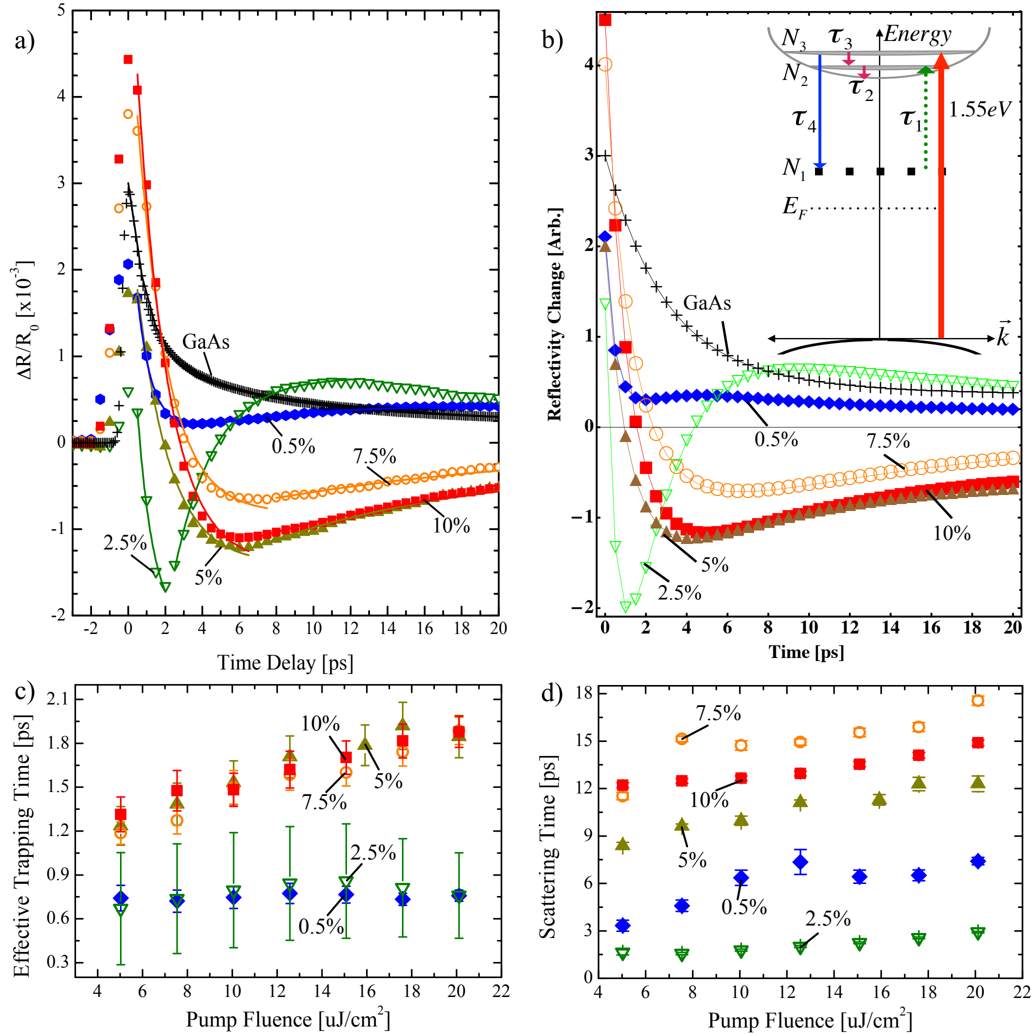

Figure 4.13 Spectral response at 1.55 eV. a) Differential reflectivity response for x=0.5-10% volume fractions of $ErAs_x$:$GaAs_{1-x}$ and the GaAs reference for a pump fluence of approximately 15 μJ/cm^2 at 1.55 eV. The solid lines are exponential fits used to extract the time constants. b) Simulations of the three level system using experimentally derived time constants at 1.55 eV with scattering from the Schottky trap state to the GaAs conduction band. Inset: Diagram of the model used in the simulation at 1.55 eV. Highly excited GaAs carriers N_3 are captured by the trap state τ_4, N_1 or relax by normal GaAs processes $\tau_{3,2}$ to the conduction band edge. Trapped carriers may be scattered τ_1 into the conduction band N_2. c) Effective carrier trapping time for the ErAs samples measured at 1.55 eV derived from experimental data as a function of pump fluence. d) Carrier scattering population times at 1.55 eV derived from experimental data as a function of pump fluence.

samples studied initially display GaAs-like carrier excitation in the conduction band, suggesting the excited carrier densities are saturating the trap states. For the $ErAs_x$:$GaAs_{1-x}$ materials at 1.55 eV (Figure 4.13a), two distinct effects are observed as a function of time delay: a fast negative carrier trapping signature and a slower scattering contribution at longer delay times.

The effective carrier trapping times are shown in Figure 4.13c. These time constants are labelled effective because trap emptying must occur before hot carriers can be trapped; therefore, the values are a combination of carrier capture and trap emptying times. Higher trap densities are expected to reduce the carrier lifetime based on earlier work [5]. However, the effective trapping times observed are longer for the higher volume fractions. The sub-ps timescales measured for the 0.5 and 2.5% $ErAs_x$:$GaAs_{1-x}$ are consistent with previously observed timescales [6, 8, 40] and show no clear carrier density dependence. For the 5-10% volume fractions, the trapping time increases with excited carrier density. Increasing trapping time with pump fluence was previously attributed to trap saturation where excited carriers remain in the GaAs until the state is available [6], consistent with the results presented here.

Carrier scattering times are shown in Figure 4.13d. The carrier scattering for the 0.5 and 2.5% systems is significantly faster at 1.55 eV than 1.46 eV, further suggesting carrier momentum impacts carrier injection from the trap state to the conduction band. The higher volume fractions show little change in scattering times above the bandgap, resulting from very high densities of excited carriers filling available states.

The simulation of the PPR at 1.55 eV is shown in Figure 4.13b in which all three states are initially populated. Trapping and state occupation dominates the response at this excitation energy, indicating an energy barrier to trapping exists.

Conclusions

The characteristic times shown in Figures 4.11, 4.12 and 4.13 are carrier energy, fluence and trap density dependent. The momentum and density of the excited carriers is critical for the trapping and scattering processes to occur as occupation of the interface state determines the response. The interface states behave as localized Schottky barriers [38, 67] and for the right conditions they trap or inject carriers to the GaAs matrix. These behaviors have not been reported by previous ultrafast studies of ErAs:GaAs or similar systems [3, 5, 6, 8, 40, 65, 68, 69].

The unique optical properties suggest ErAs:GaAs systems can be used for adaptive, highly tailored structures where the injection and depletion of carriers is optically controlled [39] and unwanted carrier dynamics can be swept out through biasing. Flexibility in the growth process could prevent stark interfaces and thereby improve charge transfer, lower resistivity, and tune barrier heights. Specific volume fraction devices could be used for photon detection at discrete energies or for carrier density detection. However, detailed knowledge of carrier dynamics is a critical preliminary step in order for ErAs:GaAs composite applications to be realized.

Competing relaxation pathways are observed in composite ErAs:GaAs systems. Ultrafast trapping of photo-carriers and carrier injection from localized Schottky states into GaAs is characterized. The systems exhibit a complex interplay of carrier trapping and scattering depending on the photo-carrier energy, carrier density, carrier momentum, and trap density as evidenced in the PPR response. Scattering from occupied Schottky states plays a large role in the response as it prevents full relaxation of the system on ultrashort timescales.

For sub-bandgap excitation, the localized Schottky state is initially populated, and excited carriers scatter to the host matrix. Saturation of the trap states is observed for lower volume

fractions. Near bandgap excitation is characterized by slower dynamics resulting from an accumulation of a significant population of warm excited carriers in the trap state before scattering can occur. At high excitation energies, GaAs-like excitation and saturation of the trap states dominates the initial PPR response, followed by rapid hot carrier trapping and scattering.

This study goes beyond previous work to fully characterize the fundamental dynamics of a wide array of nanoparticle densities. A model based on a simple three level system is sufficient to describe the ultrafast response with carrier trapping and scattering effects competing to explain the observations at different photo-excitation energies. Carrier occupation, trapping and scattering from the interface state produce the complex observed.
Furthermore, it is unclear at this point whether the higher nanoparticle volume fractions coalesce into larger particles. This issue could be addressed with TEM characterization or by using the sensitive optical techniques presented in the following chapter.

CHAPTER 5

SURFACE PLASMON POLARITONS IN ERAS:GAAS

An expert is a person who has made all the mistakes that can be made in a very narrow field.

Niels Bohr

Motivation

The flexibility in the ErAs:GaAs growth process offers the ability to tune absorption profiles of the composite by varying the ErAs deposition [9]. By embedding the nanoparticles, the resonance can be enhanced through the production of three dimensional interfaces [67]. Possible applications of IR resonances include data storage, optical filters and waveguides, solar energy conversion, catalysis, optical modulators, and switches [9, 70, 71, 72].

Quantum confinement effects significantly alter the electronic properties of ErAs as compared to the bulk material [48, 56, 61]. Conflicting reports have emerged on whether the band structure of embedded ErAs nanoparticles remains semi-metallic or if a confinement-induced bandgap opens. Several research groups have attempted to answer this question by performing static absorption and transmission measurements on nanoparticles of known sizes.

The work presented here supports the picture of semi-metallic ErAs nanoparticles. Static absorption spectra shows the existence of multiple absorption resonances due to the presence of the ErAs. Time-resolved reflectivity measurements are presented which show a strong oscillatory response indicative of surface plasmon polaritons, the first known mea-

surement of its kind in this system. The frequency of the response shifts to lower energy with excitation wavelength, moving toward expected GaAs phonon modes. Further, the highest volume fractions show polarization and power dependence in their response to ultrafast excitation, suggesting the nanoparticles are ellipsoids. The combined optical characterization suggests the response is the result of surface plasmon polaritons at the ErAs:GaAs interface coupling with the GaAs phonon modes.

State of Research

For the ErAs:GaAs composite system, a debate exists in the literature concerning the confinement effects on the ErAs nanoparticles and whether it causes a transition to occur for particles on the nanometer scale. Confinement can produce localized individual energy levels where the energy states are determined by the system's boundaries [70].

ErAs Absorption as Transitions Across a Confinement-Induced Bandgap

The infrared absorption peaks in ErAs:GaAs composite systems have been interpreted as transitions across a confinement-induced energy gap in the ErAs nanoparticles, where the ErAs undergoes a semimetal to semiconductor transition for nanoparticles less than 3 nm in diameter. Figure 5.1 shows the absorption data from a series of ErAs:GaAs samples with ErAs volume fractions ranging from 0.5-4.5%. The magnitude of the absorption peak increases linearly with ErAs incorporation, suggesting an increase in the number of absorbers present. The change in peak width is interpreted as a result of the nanoparticle size distribution, while the peak shifting with volume fraction is possibly related to hybridization of the wavefunctions between nanoparticles as their inter-particle spacing decreases [53].

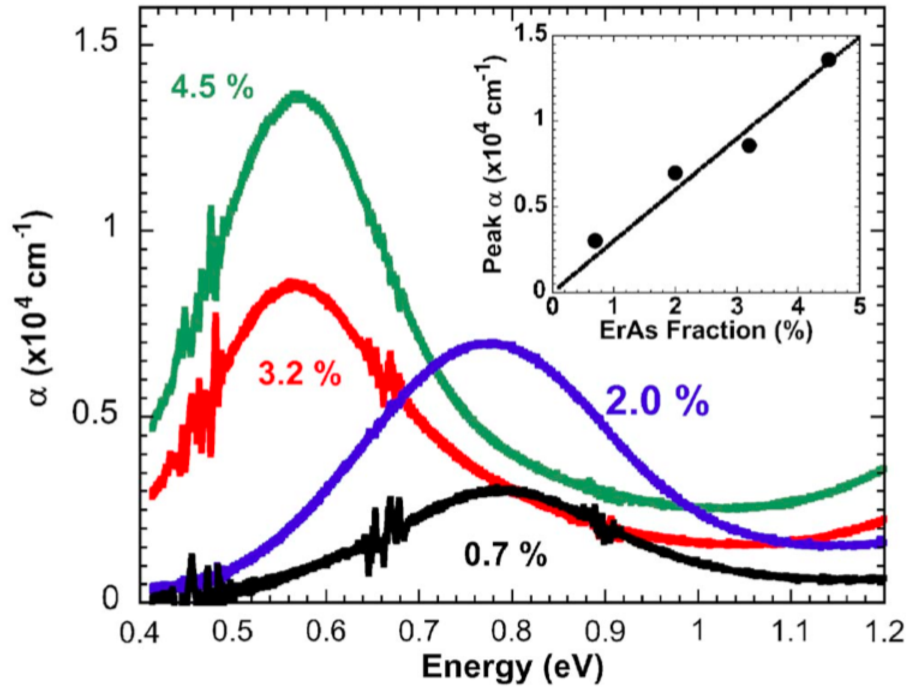

Figure 5.1 Absorption spectra for 0.5-4.5% ErAs. Left: Absorption data for ErAs:GaAs grown at 600°C vs. ErAs volume fraction. Inset: Peak absorption coefficient vs. volume fraction with a linear best-fit. Reprinted with permission from [53]. Copyright 2008, AIP Publishing LLC.

ErAs Absorption as a Surface Plasmon Resonance

Evidence for a surface-plasmon in the IR has been observed for varying ErAs layer thicknesses and fill fractions [7] as well as strong absorption and enhancement of the local electric field around the particles [9]. The resonant absorption of the particles can be shifted by the growth conditions: it is possible to tune the resonant absorption to lower energies by increasing the ErAs volume fraction [9, 53]. The absorption resonance peak can shift from 1.3 to 2.5 μm, resulting in the ErAs particles changing shape as can be seen in Figure 5.2. Increased deposition tends to push the resonance to longer wavelengths and also broadens the resonance, suggesting larger size particle distributions [9, 72].

Figure 5.3 shows the transmission of three superlattice structures at room temperature

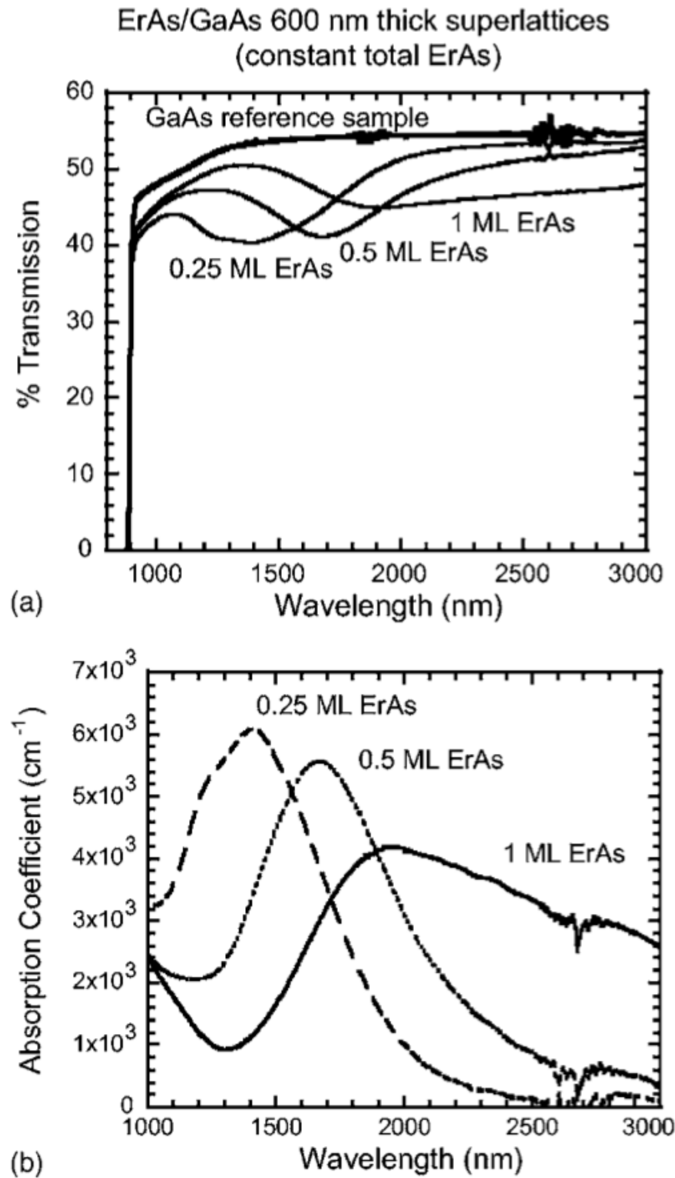

Figure 5.2 Transmission and absorption for ErAs/GaAs superlattices. (a) Transmission and (b) absorption for 0.25, 0.5, 1 ML ErAs depositions in ErAs/GaAs superlattices. The period was adjusted to 5, 10 and 20 nm for the 0.25, 0.5, and 1 ML samples, respectively, in order to maintain the total amount of ErAs in the layer constant. From Reprinted with permission from [9]. Copyright 2007, AIP Publishing LLC.

grown with varying ErAs layer thicknesses. Samples 1, 2, and 3 all contain 30 composite layers with ErAs fill fractions of 0.56, 0.85, and 1.13%, respectively. The composite layers are separated by 40 nm of GaAs and the samples were grown at 630°C [7]. The attenua-

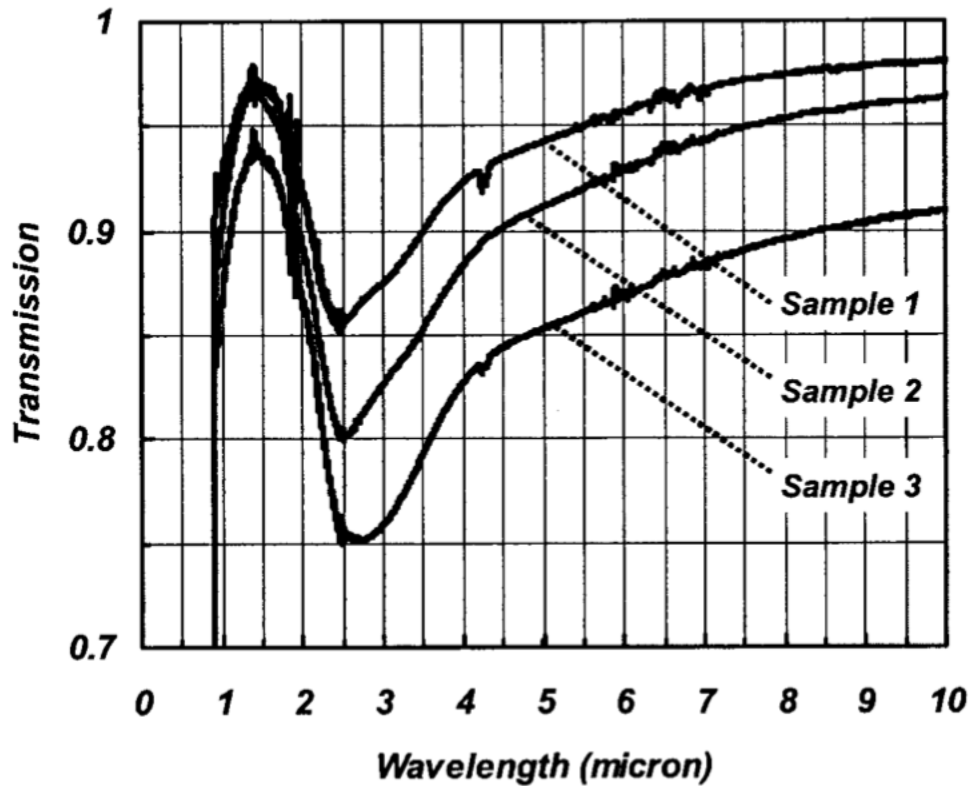

Figure 5.3 Normalized transmission for three ErAs:GaAs samples at room temperature. The GaAs band edge is seen at 0.85 μm as well as an attenuation peak centered at 2.48, 2.55, and 2.59 μm for samples 1, 2, and 3, respectively. The samples differ only in the thickness of the ErAs layers in the superlattice structure. Reprinted figure with permission from [7]. Copyright 2003 by the American Physical Society.

tion peak observed is large considering the ErAs layers constitute approximately 1% of the sample volume.

Experimental Description

In contrast to previous static and ultrafast optical studies, single layers of embedded ErAs nanoparticle systems with varying volume fractions are examined. Static absorption measurements are performed in the IR and show broad resonance bands not present in the GaAs reference sample. The frequency of the ultrafast oscillatory response is compared for different volume fractions. The change in frequency with ErAs volume fraction suggests the

nanoparticle size changes with deposition. Further, slight variations in the PPR response for different polarizations suggest the largest volume fractions may be slightly elliptical.

Samples Under Investigation

The $ErAs_x$:$GaAs_{1-x}$ is fabricated by collaborators in the Palmstrøm group at the University of California, Santa Barbara. The composite samples are grown in a Vacuum Generator V80H molecular beam epitaxy (MBE) chamber on a commercial GaAs wafer. The wafers are bonded to molybdenum sample holders using indium. The growth conditions have been detailed elsewhere [56]. The ErAs nanoparticles self-assemble [7, 9, 40, 47, 52] with particle size and density independently tunable during the growth process [6, 40, 58]. The growth temperature is held constant at 540°C during deposition, producing nanoparticle diameters of about 2 nm [51, 53, 56] for low volume fractions. Each composite sample consists of a semi-insulating substrate GaAs (001); 250 nm GaAs buffer; 300 nm of randomly distributed $ErAs_x$:$GaAs_{1-x}$ embedded nanoparticle layer grown by simultaneous co-deposition of Er, Ga and As; followed by a 10 nm GaAs capping layer to prevent oxidation (Figure 4.11a: inset). The composite layers have ErAs volume fractions of x = 0 to 10%. The $ErAs_x$:$GaAs_{1-x}$ compositions are calibrated by reflection high energy electron diffraction (RHEED) oscillations on ErAs and GaAs calibration samples. Before the optical measurements, the samples are unmounted and the back sides are mechanically polished to remove the indium used during bonding. The 0% volume fraction is used as an additional reference to ensure the observed response is not due to the growth conditions, including the possible presence of residual indium from the bonding layer on the back surface.

The absorption data are acquired by spectroscopic ellipsometry, spectrophotometery and FTIR. For the time-resolved measurements, the output of a mode-locked 76 MHz Ti:Sapphire laser with approximately 150 fs pulses is divided into polarized pump and probe beams.

The probe beam is time delayed relative to the amplitude-modulated pump beam, and a lock-in detection scheme is used (see Figure 4.11b). The pump is incident normal to the sample surface. The probe angle of incidence is 20° to the surface normal. The PPR signal is given as the relative change in reflectivity induced by the pump pulse over the background reflectivity measured by the probe ($\frac{\Delta R}{R_0}$) with a signal strength on the order of 10^{-3}.

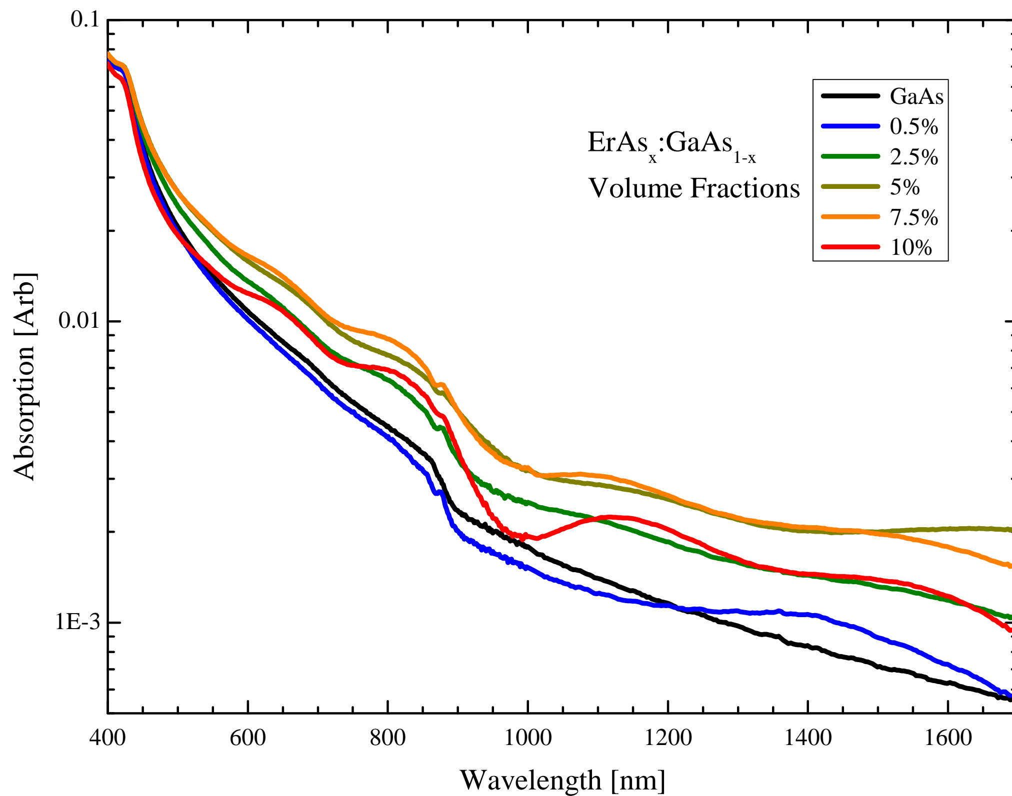

Figure 5.4 ErAs$_x$:GaAs$_{1-x}$ and GaAs reference absorption data. Several regions of increased absorption are present in the ErAs-containing samples. The GaAs absorption band edge is nominally around 872nm at 300 K.

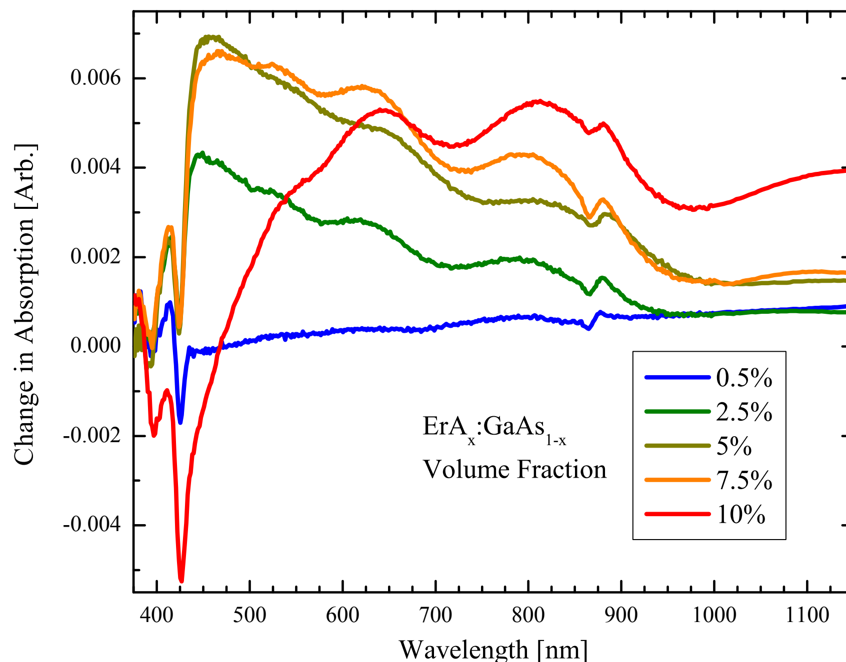

Figure 5.5 $ErAs_x$:$GaAs_{1-x}$ absorption data with the GaAs reference subtracted out. Plasmon absorption bands in the visible and UV part of the spectrum are observed for volume fractions greater than 0.5%.

Static Infrared Absorption

The incorporation of semi-metallic nanoparticles produces dramatic effects on the absorption in the visible and IR spectral regions. The static absorption spectra are shown in Figure 5.4. Multiple absorption peaks are evident in the absorption spectra both above and below the GaAs absorption edge at 880 nm, suggesting the nanoparticles are semi-metallic for the volume fractions studied.

Plasmon absorption bands are observed in Figure 5.5 from about 450-900 nm for ErAs volume fractions 2.5-7.5%. The plasmon absorption band is essentially non-existent for the 0.5% [70]. All of the ErAs containing samples show an abrupt absorption increase just below the GaAs band edge at 880 nm.

Figure 5.6 shows the IR absorption below the GaAs bandgap. A small absorption peak in the 0.5% sample around 1400 nm can be seen. The 2.5% volume fraction displays a wide peak near 2000 nm. The 5-10% composites have resonances around 2200 nm. The redshift in resonance energy with growth is consistent with larger nanoparticles for the higher volume fractions [9, 70]. Larger size distributions or increased relative proximity between adjacent nanoparticles could be the source of the broad resonance widths observed for the 2.5 and 10% samples [72]. The influence of the ErAs absorption on the transient optical response is examined below.

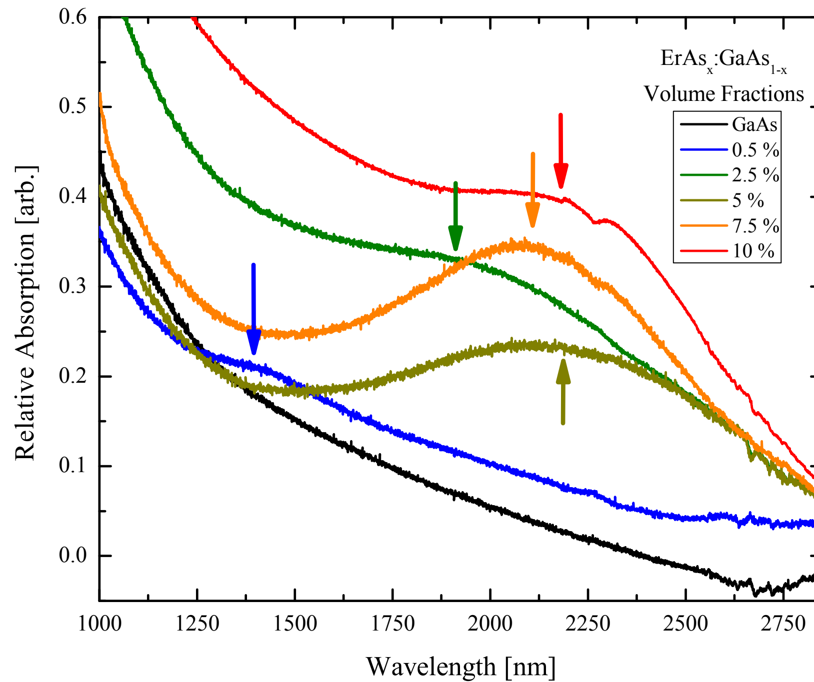

Figure 5.6 GaAs and $ErAs_x$:$GaAs_{1-x}$ absorption below the GaAs conduction band edge showing absorption peaks for all of the ErAs-containing samples (indicated by arrows) between 1250-2575 nm.

Time-Resolved Optical Measurements

The dynamics in the previous chapter focused on the transient optical response of the $ErAs_x$:$GaAs_{1-x}$ composite system within the first few ps following photo-excitation. In contrast, the dynamics investigated here detail the optical response at later time delays. Excitation is observed to produce a transient oscillatory response in the nanoparticle systems not present in the GaAs reference. The oscillatory response starts around 25 ps after excitation, indicating a formation time for the effect. Figure 5.7 shows the response of the 10% volume fraction sample for different pump fluences at 1.55 eV (800 nm). The amplitude of the oscillations is observed to increase with excitation fluence.

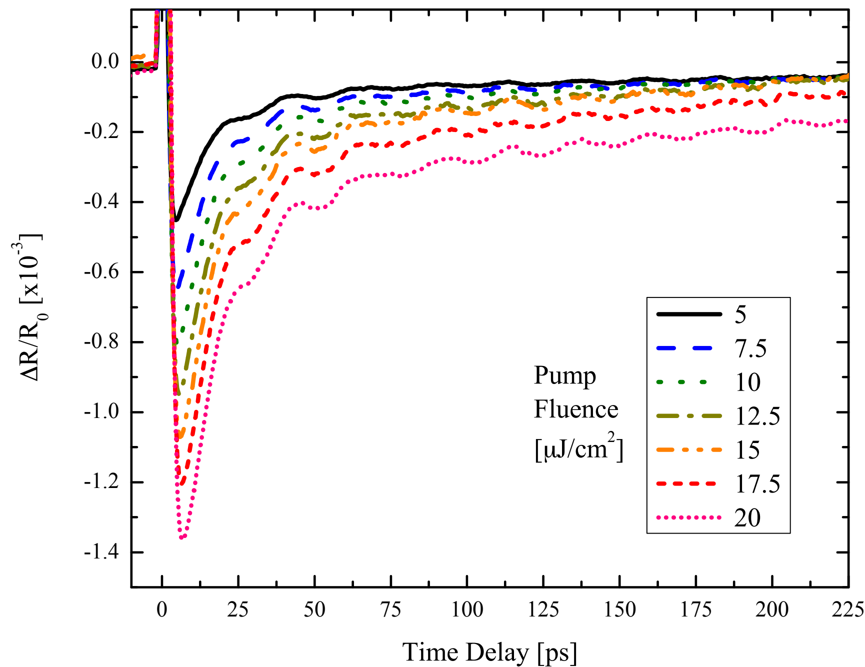

Figure 5.7 Oscillatory response of 10% $ErAs_x$:$GaAs_{1-x}$ at 1.55 eV for different pump fluences. The amplitude of the oscillations increases with pump fluence. A delayed onset of the oscillations of about 25 ps following photo-excitation is noted.

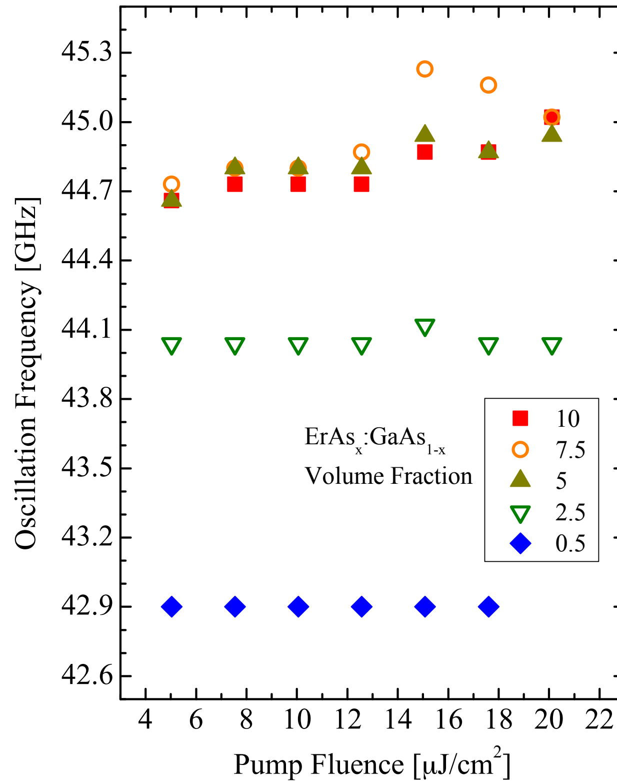

Figure 5.8 Oscillation frequencies of $ErAs_x$:$GaAs_{1-x}$ as a function of pump fluence and ErAs volume fraction obtained by Fourier transforms of the PPR signal. The change in frequency with volume fraction is qualitatively similar to the shift in the absorption peak observed in Figure 5.6.

All of the ErAs-incorporated samples display oscillations in the transient response for photo-excitation above the bandgap. The frequencies derived from Fourier transforms of the oscillating responses are shown in Figure 5.8 for the various pump fluences. The oscillation frequencies of the 0.5 and 2.5% volume fractions are not observed to vary with pump fluence; however, a slight increase in frequency with fluence is observed for higher volume fractions. Changes in the frequency with ErAs volume fraction suggest the nanoparticle size is changing with Er deposition. This is consistent with the static absorption spectra shown in Figure 5.6 where the resonance peaks are altered with ErAs incorporation. The overlap in oscillation frequencies and absorption peaks of the 5-10% samples indicates the

nanoparticles in these composites are approximately the same size.

The frequencies obtained following 1.55 eV excitation are averaged and compared to the expected phonon frequencies in the (100) direction of GaAs using experimentally derived values of the index of refraction for each of the ErAs composite samples. Table 5.1 lists the values for the observed oscillations and the expected phonon frequencies in the composite system. The GHz scale frequencies observed are slightly higher in energy than the expected phonon frequencies.

Sample	Avg. Frequency [GHz]	Phonon Frequency [GHz]	Percent Difference
0.5	42.90	43.11	0.49
2.5	44.05	42.74	3.07
5	44.83	42.07	6.56
7.5	44.94	42.30	6.25
10	44.80	42.50	5.42

Table 5.1 The average observed oscillation frequencies compared to the phonon frequency at 1.55 eV. The average frequencies obtained for different pump fluences are shown in the second column. The phonon frequencies are calculated using the acoustic wave speed of GaAs in the (100) direction and values of the index of refraction for each sample obtained by ellipsometry. The difference between the expected phonon frequency and the observed oscillation frequency are shown in the final column.

The oscillations persist with little amplitude loss for hundreds of ps, as can be seen in Figure 5.9 for excitation of the 10% volume fraction at 1.38 eV. Fourier transforms of the oscillations are shown in Figure 5.10. The phase and frequency are unaltered for different pump fluences. The average oscillation frequency for the 10% $ErAs_x$:$GaAs_{1-x}$ volume fraction at 1.38 eV is 37.69 GHz. The calculated phonon frequency at 1.38 eV for this sample is 38.59 GHz. The percent difference is thus 2.33%, significantly smaller than the value obtained at 1.55 eV. This small deviation suggests the resonance of the ErAs nanoparticles

is coupled to the phonon modes in the GaAs matrix. Combined with the ps formation time and the increase in amplitude with excitation fluence, the observed oscillations appear to be coupled surface plasmon phonon-polaritons.

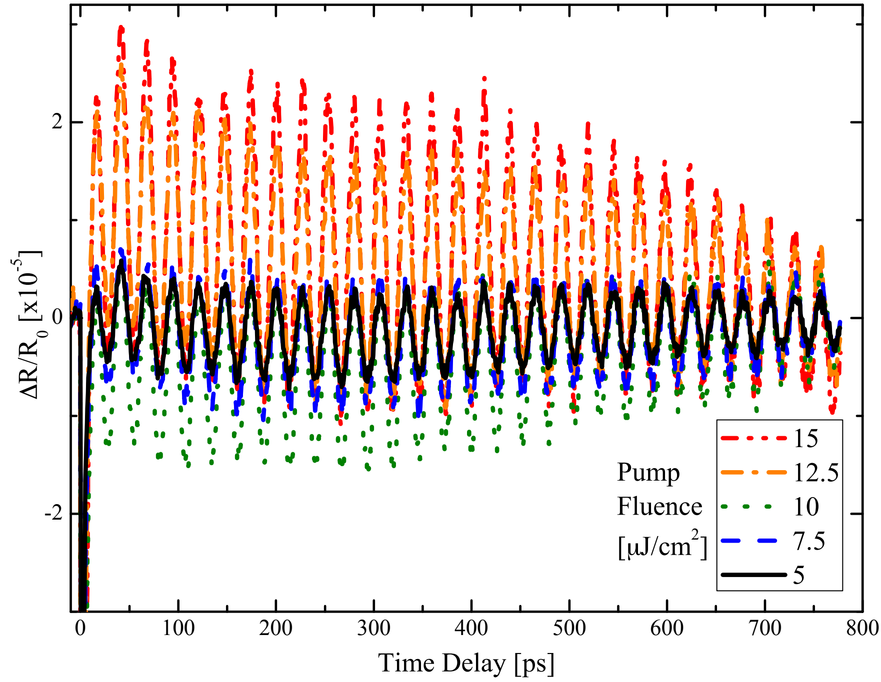

Figure 5.9 Oscillatory response of 10% $ErAs_x$:$GaAs_{1-x}$ at 1.38 eV for different pump fluences demonstrating the increasing magnitude with pump fluence and the persistence of the response over nearly 1 ns. Less attenuation is observed for lower fluences.

Figure 5.11 shows the PPR response of the 10% sample for both s and p incident polarizations. The left side shows the oscillation frequencies for s polarization as a function of pump fluence and the right shows the response for p polarization. The frequency difference between the two orientations suggests the nanoparticles are elliptical. The s polarized response shows a stronger fluence dependence, however the p polarization may indicate a threshold exists for higher energy coupling with greater fluence and carrier densities.

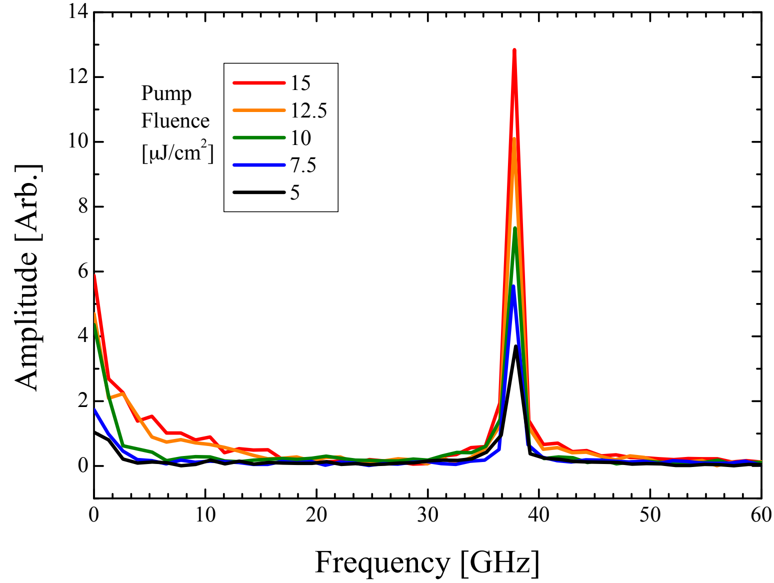

Figure 5.10 Frequency of the oscillatory response of 10% $ErAs_x$:$GaAs_{1-x}$ at 1.38 eV for different pump fluences showing the sharpness of the feature. The tails observed from 0-10 GHz are the result of the zero delay influencing the Fourier transform.

The static absorption shows several resonance features for each ErAs volume fraction. Little is known about the ErAs dielectric constant [9] and the possible broad size distribution in each volume fraction further complicates the analysis. Measuring the static absorption with polarized light should indicate if the broadened modes are the result of closely spaced nanoparticles [72]. Access to higher intensity IR ultrafast systems could produce interesting fluence dependence results, potentially revealing the nature of the coupling in the composite system and verifying the possible frequency-fluence threshold for the coupling of surface plasmon polaritons to GaAs phonons.

Summary

The work presented here discusses the nature of the absorption resonances in ErAs:GaAs composite systems. For the volume fractions studied, resonance peaks are observed in the

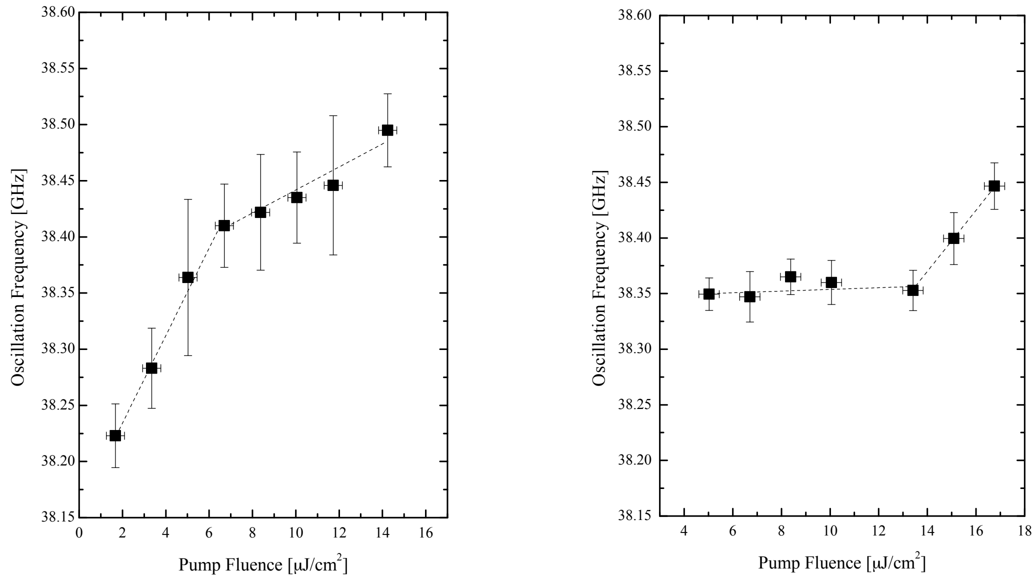

Figure 5.11 The polarization dependence of the oscillatory response on the pump fluence for the 10% composite at 1.393 eV. Left: the pump and probe are both s polarized. Right: the pump and probe are both p polarized. The fluence-dependent response is significantly stronger in the s direction but the p direction suggests a fluence threshold may exist.

static absorption spectra. These peaks suggest the nanoparticles are increasing in dimension with ErAs incorporation and a large distribution of sizes may be present. The transient optical response displays persistent oscillatory components both above and below the GaAs bandgap. The frequencies of the oscillations are observed to follow the same trend with volume fraction as the static absorption resonance peaks. Polarization dependence of the frequency response suggests the nanoparticles may be elliptical.

CHAPTER 6

CONCLUDING REMARKS

If someday they say of me that in my work I have contributed something
to the welfare and happiness of my fellow man,
I shall be satisfied.
George Westinghouse

Characterizing the optical response of a material system provides valuable information about the electronic structure, carrier transport, relaxation pathways, and defects in the system. Detailed knowledge of energy dissipation mechanisms and electronic relaxation pathways is critical for increasing efficiencies in existing technologies and necessary for new innovations to occur.

Two distinct relaxation mechanisms in bulk GaAs are reported following photo-excitation at low temperatures. The first is electronic relaxation through Landau levels and is measured through variations in the effective mass. This relaxation is observed to slow with increasing magnetic field, consistent with elastic scattering between Landau levels. The second relaxation mechanism observed is the transient bleach of the exciton transition 1s $\rightarrow 2p_{\pm1}$ which coincides with the electronic relaxation through Landau levels. Based on the observations reported here, the bleaching of the transition is likely caused by final state blocking of the 2p$_{-1}$ exciton level, which has never before been reported. This work suggests two mechanisms for electronic relaxation occur simultaneously: elastic scattering between quantized conduction band states and Auger-like relaxation through the 2p exci-

ton state. These findings may have a strong impact on semiconducting energy harvesting systems. Exciton absorption and recombination is the main energy loss mechanism in solar cells; therefore, understanding and being able to manipulate or minimize the effects could further enhance device performance, especially for low temperature applications.

Competing relaxation pathways are observed for short time delays in ErAs:GaAs systems, which exhibit a complex interplay of carrier trapping and scattering depending on the photo-carrier energy, carrier density, and trap density. The scattering process plays a large role in the response as it prevents full relaxation of the system on ultrashort timescales. For sub-bandgap excitation, the Schottky trap state is initially populated and excited carriers scatter to the host matrix. Saturation of the trap states is observed for lower volume fractions. Near bandgap excitation is characterized by slower dynamics due to the accumulation of warm excited carriers in the trap state before scattering occurs. At high excitation energies, GaAs-like excitation and saturation of the trap states dominates the initial PPR response, followed by rapid hot carrier trapping and scattering. A model based on a simple three level system accurately describes the ultrafast response with carrier occupation of the trap state explaining the observations at different photo-excitation energies. These studies goes beyond previous work to fully characterize the fundamental dynamics of a wide array of nanoparticle densities in GaAs and suggests the optical response of the system can tuned by changing the nanoparticle density in addition to the spacing between superlattice layers. The complexity of the relaxation pathway as described in this work warrants future investigation to clearly identify the carrier conductivities, potential barriers and charge transfer. In addition, more volume fractions should be characterized to determine if the results presented here are simply a result of the significantly higher ErAs nanoparticle densities compared to other works, or if the multilayer geometry prevents the observation of the dynamics reported here.

Composite ErAs:GaAs systems exhibit an oscillatory response highly suggestive of surface plasmon polariton oscillations at the interface between the semi-metallic ErAs and semiconducting GaAs, which couple to the GaAs phonon modes. The oscillatory response forms on the order of 25 ps and increases in amplitude with excitation fluence. The frequencies are observed to follow the same trend with volume fraction as the static absorption resonance peaks, indicating different size distributions exist for the 0.5, 2.5 and 5-10%. An apparent growth threshold exists in the ErAs:GaAs composite system for depositions greater than 5% volume fraction. The high volume fraction samples characterized in this work displayed similar relaxation timescales, absorption resonance peaks, and surface plasmon polariton frequencies. These results suggest that for ErAs depositions ranging from 5-10%, the nanoparticles are the same size. This is in contrast to the lower volume fractions, 0.5 and 2.5%, which show static absorption responses consistent with previous low volume fraction characterization [7, 9] in which particle size increases with ErAs deposition. To our knowledge, TEM characterization of nanoparticle size and distribution has only occurred for depositions below 5%. The results indicate a previously unreported growth phenomena is taking place in addition to the dynamics and warrants further TEM studies.

The work presented in this dissertation discusses three dynamic pathways in GaAs-based systems previously unreported in the literature. The results and references contained within indicate the study of GaAs is by no means complete and much remains to be learned from the archetype compound semiconductor.

CHAPTER 7

APPENDIX

Excitonic Calculations

An estimation of the number of unit cells within one GaAs exciton radius using the unit cell length $a = 0.56$ nm and the excitonic radius 2.48 from Chapter 2,

$$\frac{0.56nm^3}{\frac{4}{3}\pi(13nm)^3} \tag{7.1}$$

is approximately 5×10^4 unit cells [14].

The $n = 1$ excitonic state has the largest binding energy based on equation 2.47 with a value of 4.2 meV for GaAs [14]. Therefore, the highest temperature at which one would expect to be able to observed stable excitons is

$$T = \frac{E(1)}{k_B} = \frac{4.2eV}{1.38x10^{-23}J/K} \tag{7.2}$$

approximately 49 K. Consistent with the observations in Chapter 3 of no excitonic behavior at 50 K.

Carriers per Island Calculation

The ErAs carrier density is 3×10^{20} carriers/cm^3 [58]. The growth conditions for the ErAs samples indicate a nanoparticle diameter of 2.2-2.4 nm [56].

The nanoparticle volume V_{np} is therefore

$$\frac{4}{3}\pi r^3 = 9nm^3 \tag{7.3}$$

and the number of carriers per nanoparticle is approximately

$$\frac{3x10^{20}}{cm^3} * \frac{1cm^3}{10^{21}nm^3} * V_{np} = 2.7 \tag{7.4}$$

The ErAs lattice constant is 5.78 Å. The unit cell volume V_{cell} is therefore 0.193 nm^3. The number of unit cells per nanoparticle is estimated to be

$$\frac{V_{np}}{V_{cell}} = 47 \tag{7.5}$$

The ErAs unit cell has four Er atoms; therefore, there are approximately 188 Er atoms per nanoparticle. This indicates most of the Er electrons are bound as the number of free carriers per nanoparticle is 70× smaller than the number of Er ions in the nanoparticle.

Simulation Code for the ErAs:GaAs Potential Barrier Dynamics

The Mathematica code used for the simulations is based on coupled first order differential equations. The plot output default shows all the curves on the same figure, but allows one to manipulate the figure to show each curve individually as well. The code for the 900 nm (1.38 eV) simulation is shown here.

```
Manipulate[
 Module[{t, z, sol, p1, p2, p3, p4, p5, p6, k1, k2, k3, k4,
 k0, T1, T2, T3, T4, T5, T6, T7, T8, T9, T0, U1, U2, U3,
 U4, v0, v1, v2, v3, v4, D0, D1, D2, D3, D4},
  T1 = .427; T2 = 14.47; T3 = .37029; T4 = .5568;
```

```
T5 = .88312; T6 = .9117; T7 = .8535; D0 = .37029;
D1 = .5568; D2 = .88312; D3 = .9117; D4 = .8535;
z = If[T1 < 475, 10, 1];
U1 = 0*Exp[-t/T1];(*hot carrier cooling*)

U2 = .00*Exp[-t/T2];(*band edge relaxation*)

k0 = .0*Exp[-t/T3];(*trapping time 0.5*)

v0 = 1.75*Exp[-t/D0];(*scattering 0.5*)

k1 = 0*Exp[-t/T4];(*trapping time 2.5*)

v1 = 1.0*Exp[-t/D1];(*scattering 2.5*)

k2 = .0*Exp[-t/T5];(*trapping time 5*)

v2 = .755*Exp[-t/D2];(*scattering 5*)

k3 = .0*Exp[-t/T6];(*trapping time 7.5*)

v3 = .65*Exp[-t/D3];(*scattering 7.5*)

k4 = .0*Exp[-t/T7];(*trapping time 10*)

v4 = .76*Exp[-t/D4];(*scattering 10*)
```

```
sol = NDSolve[{
Ca'[t] == -U1*Ca[t], (*equations for GaAs*)
Cb'[t] == U1*Ca[t] - U2*Cb[t],
Cc'[t] == 0,

Cd'[t] == -U1*Cd[t] - k0*Cd[t], (*equations for 0.5% ErAs*)
Ce'[t] == U1*Cd[t] - U2*Ce[t] - k0*Ce[t] + v0*Cf[t],
Cf'[t] == k0*(Cd[t] + Ce[t]) - v0*Cf[t],

Cg'[t] == -U1*Cg[t] - k1*Cg[t], (*equations for 2.5% ErAs*)
Ch'[t] == U1*Cg[t] - U2*Ch[t] - k1*Ch[t] + v1*Ci[t],
Ci'[t] == k1*(Ch[t] + Cg[t]) - v1*Ci[t],

Cj'[t] == -U1*Cj[t] - k2*Cj[t], (*equations for 5% ErAs*)
Ck'[t] == U1*Cj[t] - U2*Ck[t] - k2*Ck[t] + v2*Cl[t],
Cl'[t] == k2*(Cj[t] + Ck[t]) - v2*Cl[t],

Cm'[t] == -U1*Cm[t] - k3*Cm[t], (*equations for 7.5% ErAs*)
Cn'[t] == U1*Cm[t] - U2*Cn[t] - k3*Cn[t] + v3*Co[t],
Co'[t] == k3*(Cm[t] + Cn[t]) - v3*Co[t],

Cp'[t] == -U1*Cp[t] - k4*Cp[t], (*equations for 10% ErAs*)
Cq'[t] == U1*Cp[t] - U2*Cq[t] - k4*Cq[t] + v4*Cr[t],
Cr'[t] == k4*(Cp[t] + Cq[t]) - v4*Cr[t],

    Ca[0] == .0,  (*initial conditions GaAs*)
    Cb[0] == .0,
```

```
        Cc[0] == 0.0,

        Cd[0] == .0,(*initial conditions 0.5% ErAs*)
        Ce[0] == .0,
        Cf[0] == 0.2,

        Cg[0] == 0.,(*initial conditions 2.5% ErAs*)
        Ch[0] == .0,
        Ci[0] == .80,

        Cj[0] == 0.,(*initial conditions 5% ErAs*)
        Ck[0] == .0,
        Cl[0] == 1.18,

        Cm[0] == 0.,(*initial conditions 7.5% ErAs*)
        Cn[0] == .0,
        Co[0] == 1.41,

        Cp[0] == 0,(*initial conditions 10% ErAs*)
        Cq[0] == .0,
        Cr[0] == 1.4},

{Ca, Cb, Cc, Cd, Ce, Cf, Cg, Ch, Ci, Cj, Ck, Cl, Cm,
Cn, Co, Cp, Cq, Cr},
     {t, 0, z}];
   p1 = ListLinePlot[
Table[{t, Ca[t] + Cb[t] - Cc[t] /. sol[[1]]},
```

```
{t, 0, z, z/40}],
    PlotMarkers -> Style["+", Large], PlotRange -> All,
    AspectRatio -> 7/5,
    PlotStyle -> {Thin, Black},
    Frame -> True,
    FrameStyle -> {Thick, Thick},
    FrameTicksStyle -> Directive[Large, 20],
    FrameLabel -> {"Time [ps] ",
    "Reflectivity Change [Arb.] "},
    LabelStyle -> {FontSize -> 20, Bold},
    ImageSize -> {750, 700},
    ImagePadding -> {{70, 5}, {50, 10}}];
  p2 = ListLinePlot[
  Table[{t, Cd[t] + Ce[t] - Cf[t] /. sol[[1]]},
  {t, 0, z, z/40}],
    PlotMarkers -> Style["\[FilledDiamond]", Large],
    PlotRange -> All,
    PlotStyle -> {Thin, Blue},
    AspectRatio -> 7/5,
    Frame -> True,
    FrameStyle -> {Thick, Thick},
    FrameTicksStyle -> Directive[Large, 20],
    FrameLabel -> {"Time [ps] ",
    "Reflectivity Change [Arb.] "},
    LabelStyle -> {FontSize -> 20},
    ImageSize -> {750, 700},
    ImagePadding -> {{70, 5}, {50, 10}}];
```

```
  p3 = ListLinePlot[
Table[{t, Cg[t] + Ch[t] - Ci[t] /. sol[[1]]},
{t, 0, z, z/40}],
    PlotMarkers -> Style["\[EmptyDownTriangle]", Large],
    PlotRange -> All,
    AspectRatio -> 8/5,
    PlotStyle -> {Thin, Green},
    Frame -> True,
    FrameStyle -> {Thick, Thick},
    FrameTicksStyle -> Directive[Large, 20],
    FrameLabel -> {"Time [ps] ",
    "Reflectivity Change [Arb.] "},
    LabelStyle -> {FontSize -> 20, Bold},
    ImageSize -> {750, 700},
    ImagePadding -> {{70, 5}, {50, 10}}];
  p4 = ListLinePlot[
Table[{t, Cj[t] + Ck[t] - Cl[t] /. sol[[1]]},
{t, 0, z, z/40}],
    PlotMarkers -> Style["\[FilledUpTriangle]", Large],
    PlotRange -> All,
    AspectRatio -> 7/5,
    PlotStyle -> {Thin, Brown},
    Frame -> True,
    FrameStyle -> {Thick, Thick},
    FrameTicksStyle -> Directive[Large, 20],
    FrameLabel -> {"Time [ps] ",
    "Reflectivity Change [Arb.]"},
```

```
    LabelStyle -> {FontSize -> 20, Bold},
    ImageSize -> {750, 700},
    ImagePadding -> {{70, 5}, {50, 10}}];
  p5 = ListLinePlot[
Table[{t, Cm[t] + Cn[t] - Co[t] /. sol[[1]]},
{t, 0, z, z/40}],
    PlotMarkers -> Style["\[EmptyCircle]", Large],
    PlotRange -> All,
    AspectRatio -> 7/5,
    PlotStyle -> {Thin, Orange},
    Frame -> True,
    FrameStyle -> {Thick, Thick},
    FrameTicksStyle -> Directive[Large, 20],
    FrameLabel -> {"Time [ps] ",
    "Reflectivity Change [Arb.]"},
    LabelStyle -> {FontSize -> 20, Bold},
    ImageSize -> {750, 700},
    ImagePadding -> {{70, 5}, {50, 10}}];
  p6 = ListLinePlot[
Table[{t, Cp[t] + Cq[t] - Cr[t] /. sol[[1]]},
 {t, 0, z, z/40}],
    PlotMarkers -> Style[ "\[FilledSquare]", Large],
    PlotRange -> {{-.3, 10.3}, {-1.5, .075}},
    AspectRatio -> 7/5,
    Frame -> True,
    FrameStyle -> {Thick, Thick},
    FrameTicks -> {{Automatic,
```

```
        Automatic}, {{0, 1, 2, 3, 4, 5, 6, 7, 8, 9, 10},
        Automatic}},
    FrameTicksStyle -> Directive[Large, 20],
    PlotStyle -> {Thin, Red},
    FrameLabel -> {"Time␣[ps]␣",
    "Reflectivity␣Change␣[Arb.]"},
    LabelStyle -> {FontSize -> 20, Bold},
    ImageSize -> {750, 700},
    ImagePadding -> {{70, 5}, {50, 10}}];
  Switch[plt,
   1, Show[p1],
   2, Show[p2],
   3, Show[p3],
   4, Show[p4],
   5, Show[p5],
   6, Show[p6],
   7, Show[p6, p2, p3, p4, p5, p1]]],
{{plt, 7, ""}, {
   1 -> Text@Style["GaAs", Italic],
   2 -> Text@Style["0.5%", Italic],
   3 -> Text@Style["2.5%", Italic],
   4 -> Text@Style["5%", Italic],
   5 -> Text@Style["7.5%", Italic],
   6 -> Text@Style["10%", Italic],
   7 -> "all"}, ControlType -> SetterBar},
ContentSize -> {840, 840}, Alignment -> Center]
```

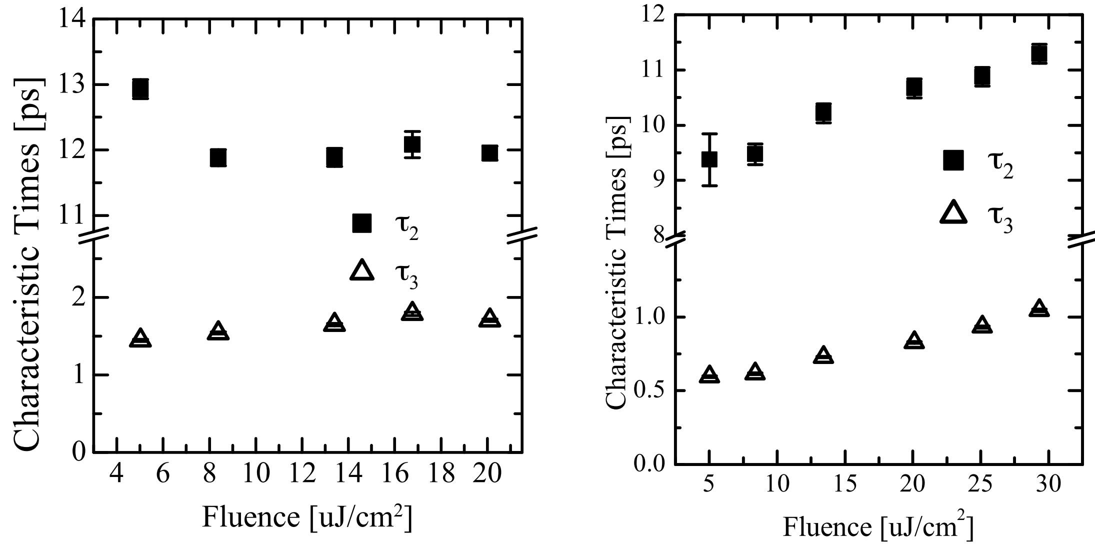

Figure 7.1 GaAs Characteristic Timescales for Excitation at 1.46 and 1.55 eV

Average values of the observed characteristic times are used at each photon energy simulated. The strength of each component and the initial population of the states are changed at each energy.

Figure 7.1 shows the fluence-dependent time constants of GaAs at 1.46 and 1.55 eV used in the simulation. Radiative recombination is not observed on the timescales reported in Chapters 3 and 4. For near bandgap excitation, the carriers have small amounts of excess energy and are referred to as cool. For excitations with excess energy greater than 36 meV, the carrier distribution is referred to as hot and is capable of emitting longitudinal optical phonons and scattering, decreasing the population decay time with increasing excitation energy. This decrease in characteristic time with photon energy is observed in the GaAs $\tau_{2,3}$ time constants Figure 7.1, where τ_2 is the band edge thermalization time and τ_3 is a carrier scattering time. The time constants at 1.55 eV are significantly shorter for a given

fluence than at 1.46 eV due to optical phonon emission and rapid energy redistribution that occurs at higher photo-excitation energies. The fluence dependence indicates the effects of carrier densities on the redistribution of energy. The two GaAs states used in the model represent the different kinetics occurring for cold and hot electron distributions and are not meant to imply only two energy states exist in the conduction band.

Phonon Frequencies

Phonon oscillation frequencies are calculated using the longitudinal acoustic wave speed in the [100] direction of GaAs 4.73 nm/ps [19], the experimentally derived index of refraction, and the excitation wavelength. Calculations for the GaAs reference and the ErAs:GaAs composite samples are shown in Table 7.1 for 800 nm excitation.

$$f = \frac{2 v_s n}{\lambda} \tag{7.6}$$

Sample	Experimental n value at 1.55 eV	Expected Phonon Frequency [GHz]
GaAs	3.62	42.82
0.5	3.65	43.11
2.5	3.61	42.74
5	3.56	42.07
7.5	3.58	42.30
10	3.59	42.50

Table 7.1 Experimental Values of the Index of Refraction and Expected Phonon Frequencies at 1.55 eV

BIBLIOGRAPHY

[1] J. Shah. *Ultrafast spectroscopy of semiconductors and semiconductor nanostructures*. Solid State Sciences. Springer-Verlag, Berlin, 1999.

[2] D. D. Nolte. Optical scattering and absorption by metal nanoclusters in gaas. *J. Appl. Phys.*, 76(6):3740–3745, 1994.

[3] J. F. O'Hara, J. M. O. Zide, A. C. Gossard, A. J. Taylor, and R. D. Averitt. Enhanced terahertz detection via eras:gaas nanoisland superlattices. *Appl. Phys. Lett.*, 88(25):251119, 2006.

[4] J. M. O. Zide, A. Kleiman-Shwarsctein, N. C. Strandwitz, J. D. Zimmerman, T. Steenblock-Smith, A. C. Gossard, A. Forman, A. Ivanovskaya, and G. D. Stucky. Increased efficiency in multijunction solar cells through the incorporation of semimetallic eras nanoparticles into the tunnel junction. *Appl. Phys. Lett.*, 88(16):–, 2006.

[5] A. K. Azad, R. P. Prasankumar, D. Talbayev, A. J. Taylor, R. D. Averitt, J. M. O. Zide, H. Lu, A. C. Gossard, and J. F. O'Hara. Carrier dynamics in ingaas with embedded eras nanoislands. *Appl. Phys. Lett.*, 93(12):–, 2008.

[6] R. P. Prasankumar, A. Scopatz, D. J. Hilton, A. J. Taylor, R. D. Averitt, J. M. Zide, and A. C. Gossard. Carrier dynamics in self-assembled eras nanoislands embedded in gaas measured by optical-pump terahertz-probe spectroscopy. *Appl. Phys. Lett.*, 86(20):201107, 2005.

[7] E. R. Brown, A. Bacher, D. Driscoll, M. Hanson, C. Kadow, and A. C. Gossard. Evidence for a strong surface-plasmon resonance on eras nanoparticles in gaas. *Phys. Rev. Lett.*, 90:077403, Feb 2003.

[8] M. Griebel, J. H. Smet, D. C. Driscoll, J. Kuhl, C. A. Diez, N. Freytag, C. Kadow, A. C. Gossard, and K. von Klitzing. Tunable subpicosecond optoelectronic transduction in superlattices of self-assembled eras nanoislands. *Nat. Mater.*, 2(2):122–126, 02 2003.

[9] M. P. Hanson, A. C. Gossard, and E. R. Brown. Infrared surface plasmon resonances due to er-v semimetallic nanoparticles in iii-v semiconductor matrices. *J. Appl. Phys.*, 102(4):043112, 2007.

[10] G. Butcher. Anatomy of an electromagnetic wave. *NASA Mission:Science*, 2014.

[11] F. Wooten. *Optical Properties of Solids*. Academic Press, New York, 1972.

[12] J. D. Jackson. *Classical Electrodynamics*. John Wiley & Sons, Inc, New Jersey, 3 edition, 1999.

[13] M. Born and E. Wolf. *Principles of Optics*. Cambridge University Press, Cambridge, 7 expanded edition, 1999.

[14] M. Fox. *Optical Properties of Solids*. Oxford Master Series in Condensed Matter Physics. Oxford University Press, Oxford, 3 edition, 2010.

[15] J. P. Callan, A. M.-T. Kim, C. A. D. Roeser, and E. Mazur. *Ultrafast Physical Processes in Semiconductors*, volume 67 of *Semiconductors and Semimetals*. Academic Press, New York, 2001.

[16] C. Kittel. *Introduction to Solid State Physics*. Wiley, New Jersey, eighth edition, 2005.

[17] J. S. Blakemore. *Semiconductor Statistics*. Dover Publications, Inc., New York, 1987.

[18] Gallium arsenide. *Wikipedia, the free encyclopedia*, 2014.

[19] Gallium arsenide. *Ioffe NSM Database*, 2014.

[20] D. von der Linde. Laser spectroscopy of ultrafast solid-state phenomena. *Ann. Rev. Mat. Sci.*, 18:75–100, 1988.

[21] S. S. Prabhu and A. S. Vengurlekar. Dynamics of the pump-probe reflectivity spectra in gaas and gan. *J. Appl. Phys.*, 95(12):7803–7812, 2004.

[22] B. R. Bennett, R. A. Soref, and J. A. del Alamo. Carrier-induced change in refractive-index of inp, gaas, and ingaasp. *J. Quant. Electron.*, 26(1):113–122, 1990.

[23] R. A. Kaindl, M. A. Carnahan, D. Hagele, R. Lovenich, and D. S. Chemla. Ultrafast terahertz probes of transient conducting and insulating phases in an electron-hole gas. *Nature*, 423:734–738, 2003.

[24] S. W. Koch, M. Kira, G. Khitrova, and H. M. Gibbs. Semiconductor excitons in new light. *Nat. Mater.*, 5:523 – 531, 2006.

[25] M. A. Zudov, A. P. Mitchell, A. H. Chin, and J. Kono. Terahertz magnetospectroscopy of transient plasmas in semiconductors. *J. Appl. Phys.*, 94(5):3271–3277, 2003.

[26] T. Arikawa, X. Wang, D. J. Hilton, J. L. Reno, W. Pan, and J. Kono. Quantum control of a landau-quantized two-dimensional electron gas in a gaas quantum well using coherent terahertz pulses. *Phys. Rev. B*, 84:241307(R), 2011.

[27] W. H. Knox, R. L. Fork, M. C. Downer, D. A. B. Miller, D. S. Chemla, C. V. Shank, A. C. Gossard, and W. Wiegmann. Femtosecond dynamics of resonantly excited excitons in room-temperature gaas quantum wells. *Phys. Rev. Lett.*, 54(12):1306–1309, Mar 1985.

[28] T. Meier and S. W. Koch. Excitons versus unbound electron-hole pairs and their influence on exciton bleaching: A model study. *Phys. Rev. B*, 59(20):13202–13208, May 1999.

[29] R. P. S. M. Lobo, J. D. LaVeigne, D. H. Reitze, D. B. Tanner, and G. L. Carr. Sub-nanosecond, time-resolved, broadband infrared spectroscopy using synchrotron radiation. *Rev. Sci. Instrum.*, 73(1):1–10, 2002.

[30] G. L. Carr, R. P. S. M. Lobo, J. LaVeigne, D. H. Reitze, and D. B. Tanner. Exploring the dynamics of superconductors by time-resolved far-infrared spectroscopy. *Phys. Rev. Lett.*, 85(14):3001–3004, Oct 2000.

[31] G. L. Carr. Dynamics of gaas photocarriers probed with pulsed infrared synchrotron radiation. *Nucl. Instrum. Meth. B*, 199:323 – 327, 2003.

[32] T.-Y. Zhang and W. Zhao. Magnetoexcitonic optical absorption in semiconductors under strong magnetic fields and intense terahertz radiation in the voigt configuration. *Europhys. Lett.*, 82(6):67001, 2008.

[33] G. R. Allan, A. Black, C. R. Pidgeon, E. Gornik, W. Seidenbusch, and P. Colter. Impurity and landau-level electron lifetimes in n-type gaas. *Phys. Rev. B*, 31(6):3560–3567, Mar 1985.

[34] X. Xi, R.J. Smith, T.N. Stanislavchuk, A.A. Sirenko, S.N. Gilbert, J.J. Tu, and G.L. Carr. A broadband silicon quarter-wave retarder for far-infrared spectroscopic circular dichroism. *Infrared Phys. Techn.*, 67(0):436 – 440, 2014.

[35] G. A. Khodaparast, D. C. Larrabee, J. Kono, D. S. King, S. J. Chung, and M. B. Santos. Relaxation of quasi-two-dimensional electrons in a quantizing magnetic field probed by time-resolved cyclotron resonance. *Phys. Rev. B*, 67(3):035307, Jan 2003.

[36] R. M. Hannak, W. W. Rühle, and K. Köhler. Relaxation dynamics of electrons between landau levels in gaas. *Phys. Rev. B*, 53(24):R16137–R16139, Jun 1996.

[37] A. P. Mitchell, A. H. Chin, and J. Kono. Picosecond time-resolved cyclotron resonance of non-equilibrium carriers in semiconductors. *Physica B*, 272(1-4):434 – 437, 1999.

[38] D. C. Driscoll, M. Hanson, C. Kadow, and A. C. Gossard. Electronic structure and conduction in a metal/semiconductor digital composite: Eras:ingaas. *Appl. Phys. Lett.*, 78:1703–1705, 2001.

[39] N. I. Zheludev and Y. S. Kivshar. From metamaterials to metadevices. *Nat. Mater.*, 11:917–924, 2012.

[40] C. Kadow, S. B. Fleischer, J. P. Ibbetson, J. E. Bowers, A. C. Gossard, J. W. Dong, and C. J. Palmstrøm. Self-assembled eras islands in gaas: Growth and subpicosecond carrier dynamics. *Appl. Phys. Lett.*, 75(22):3548–3550, 1999.

[41] D. O. Klenov, J. M. Zide, J. D. Zimmerman, A. C. Gossard, and S. Stemmer. Interface atomic structure of epitaxial eras layers on (001) in0.53ga0.47as and gaas. *Appl. Phys. Lett.*, 86(24):–, 2005.

[42] N.G. Stoffel, C.J. Palmstrøm, and B.J. Wilkens. Ion channeling measurement of the lattice registry of ultrathin eras layers in gaas/eras/gaas (001) heterostructures. *Nucl. Instrum. and Meth. B.*, 5657, Part 2(0):792 – 794, 1991.

[43] H.-K. Jeong, T. Komesu, C.-S. Yang, P.A Dowben, B.D Schultz, and C.J Palmstrøm. Photoemission forward scattering from eras(100)/gaas(100). *Mater. Lett.*, 58(24):2993 – 2996, 2004.

[44] T. E. Buehl, J. M. LeBeau, S. Stemmer, M. A. Scarpulla, C. J. Palmstrøm, and A. C. Gossard. Growth of embedded eras nanorods on (411)a and (411)b gaas by molecular beam epitaxy. *J. Cryst. Growth*, 312(14):2089 – 2092, 2010.

[45] J. K. Kawasaki, R. Timm, T. E. Buehl, E. Lundgren, A. Mikkelsen, A. C. Gossard, and C. J. Palmstrøm. Cross-sectional scanning tunneling microscopy and spectroscopy of semimetallic eras nanostructures embedded in gaas. volume 29, page 03C104. AVS, 2011.

[46] P. Pohl, F. H. Renner, M. Eckardt, A. Schwanhuer, A. Friedrich, . Yksekdag, S. Malzer, G. H. Dhler, P. Kiesel, D. Driscoll, M. Hanson, and A. C. Gossard. Enhanced recombination tunneling in gaas pn junctions containing low-temperature-grown-gaas and eras layers. *Appl. Phys. Lett.*, 83(19):4035–4037, 2003.

[47] S. Sethi and P. K. Bhattacharya. Characteristics and device applications of erbium doped iii-v semiconductors grown by molecular beam epitaxy. *J. Electron. Mater.*, 25:467–477, mar 1996.

[48] K. T. Delaney, N. A. Spaldin, and C. G. Van de Walle. Theoretical study of schottky-barrier formation at epitaxial rare-earth-metal/semiconductor interfaces. *Phys. Rev. B*, 81:165312, Apr 2010.

[49] R. Yano, Y. Hirayama, S. Miyashita, H. Sasabu, N. Uesugi, and S. Uehara. Pump & probe spectroscopy of low-temperature grown gaas for carrier lifetime estimation: arsenic pressure dependence of carrier lifetime during mbe crystal growth. *Phys. Lett. A*, 289(1 and 2):93 – 98, 2001.

[50] M. C. Beard, G. M. Turner, and C. A. Schmuttenmaer. Subpicosecond carrier dynamics in low-temperature grown gaas as measured by time-resolved terahertz spectroscopy. *J. Appl. Phys.*, 90(12):5915–5923, 2001.

[51] K. W. Park, V. D. Dasika, H. P. Nair, A. M. Crook, S. R. Bank, and E. T. Yu. Conductivity and structure of eras nanoparticles embedded in gaas pn junctions analyzed via conductive atomic force microscopy. *Appl. Phys. Lett.*, 100(23):233117, 2012.

[52] H. P. Nair, A. M. Crook, and S. R. Bank. Enhanced conductivity of tunnel junctions employing semimetallic nanoparticles through variation in growth temperature and deposition. *Appl. Phys. Lett.*, 96(22):222104, 2010.

[53] M. A. Scarpulla, J. M. O. Zide, J. M. LeBeau, C. G. Van de Walle, A. C. Gossard, and K. T. Delaney. Near-infrared absorption and semimetal-semiconductor transition in 2 nm eras nanoparticles embedded in gaas and alas. *Appl. Phys. Lett.*, 92(17):173116, 2008.

[54] W. Kim, J. Zide, A. Gossard, D. Klenov, S. Stemmer, A. Shakouri, and A. Majumdar. Thermal conductivity reduction and thermoelectric figure of merit increase by embedding nanoparticles in crystalline semiconductors. *Phys. Rev. Lett.*, 96:045901, Feb 2006.

[55] J. Russell, I. Appelbaum, V. Narayanamurti, M. P. Hanson, and A. C. Gossard. Transverse momentum nonconservation at the eras/gaas interface. *Phys. Rev. B*, 71, 2005.

[56] J. K. Kawasaki, R. Timm, K. T. Delaney, E. Lundgren, A. Mikkelsen, and C. J. Palmstrøm. Local density of states and interface effects in semimetallic eras nanoparticles embedded in gaas. *Phys. Rev. Lett.*, 107:036806, Jul 2011.

[57] C. Kadow, J. A. Johnson, K. Kolstad, J. P. Ibbetson, and A. C. Gossard. Growth and microstructure of self-assembled eras islands in gaas. *J. Vac. Technol. B*, 18:2197, 2000.

[58] D. R. Schmidt, A. G. Petukhov, M. Foygel, J. P. Ibbetson, and S. J. Allen. Fluctuation controlled hopping of bound magnetic polarons in eras:gaas nanocomposites. *Phys. Rev. Lett.*, 82:823–826, Jan 1999.

[59] A. Dorn, M. Peter, S. Kicin, T. Ihn, K. Ensslin, D. Driscoll, and A. C. Gossard. Charge tunable eras islands for backgate isolation in algaas heterostructures. *Appl. Phys. Lett.*, 82:2631, 2003.

[60] J. D. Zimmerman, E. R. Brown, and A. C. Gossard. Tunable all epitaxial semimetal-semiconductor schottky diode system: Eras on inalgaas. *J. Vac. Sci. Technol. B*, 23:1929, 2005.

[61] M. Said, C.M. Bertoni, A. Fasolino, and S. Ossicini. Electronic structure of rare earth arsenide/gallium arsenide superlattices. *Solid State Commun.*, 100(7):477 – 480, 1996.

[62] W. R. L. Lambrecht, A. G.Petukhov, and B. T. Hemmelman. Schottky barrier formation at eras/gaas interfaces: a case of fermi level pinning by surface states. *Solid State Commun.*, 108:361–365, 1998.

[63] H. Yamaguchi and Y. Horikoshi. Growth of gaas/eras/gaas structure by migration enhanced epitaxy. *Appl. Phys. Lett.*, 60:2341, 1992.

[64] J. D. Ralston, F. Fuchs, J. Schneider, and J. Schmälzlin. Study of eras/gaas strained-layer structures using optical absorption and ion channeling. *J. Appl. Phys.*, 68(5):2176–2180, 1990.

[65] M. P. Hanson, D. C. Driscoll, J. D. Zimmerman, A. C. Gossard, and E. R. Brown. Subpicosecond photocarrier lifetimes in gasb/ersb nanoparticle superlattices at 1.55 μm. *Appl. Phys. Lett.*, 85(15):3110–3112, 2004.

[66] C. J. Palmstrøm, T. L. Cheeks, H. L. Gilchrist, J. G. Zhu, C. B. Carter, B. J. Wilkens, and R. Martin. Effect of orientation on the schottky barrier height of thermodynamically stable epitaxial metal/gaas structures. *J.Vac. Sci. Technol. A*, 10(4):1946–1953, 1992.

[67] M. W. Knight, Y. Wang, A. S. Urban, A. Sobhani, B. Y. Zheng, P. Nordlander, and N. J. Halas. Embedding plasmonic nanostructure diodes enhances hot electron emission. *Nano Lett.*, 13(4):1687–1692, 2013.

[68] H. Lu, D. G. Ouellette, S. Preu, J. D Watts, B. Zaks, P.G. Burke, M. S. Sherwin, and A. C. Gossard. Self-assembled ersb nanostructures with optical applications in infrared and terahertz. *Nano Lett.*, 14:1107–1112, 2014.

[69] L. R. Vanderhoef, A.K. Azad, C. C. Bomberger, D. R. Chowdhury, D. B. Chase, A. J. Taylor, J. M. O. Zide, and M. F. Doty. Charge carrier relaxation processes in tbas nanoinclusions in gaas measured by optical-pump thz-probe transient absorption spectroscopy. *Phys. Rev. B*, 89:045418, 2014.

[70] S. Link and M. A. El-Sayed. Spectral properties and relaxation dynamics of surface plasmon electronic oscillations in gold and silver nanodots and nanorods. *J. Phys. Chem. B*, 103:8410–8426, 1999.

[71] H. A. Atwater, J. A. Dionne, and L. A. Sweatlock. *Surface Plasmon Nanophotonics*, volume 131 of *Springer Series in Optical Sciences*. Springer, The Netherlands, 2007.

[72] A. Hohenau, A. Leitner, and F. R. Aussenegg. *Surface Plasmon Nanophotonics*, volume 131 of *Springer Series in Optical Sciences*. Springer, The Netherlands, 2007.